PROJECT MONARCH:

THE APPLICATION OF LUDWIG PRANDTL'S BELL-CURVE SPAN LOADING TO A STRAIGHT, HIGH PERFORMANCE SAILPLANE WING

By

COLE KELLY

Bachelor of Science in Aerospace Engineering
Bachelor of Science in Mechanical Engineering
Oklahoma State University
Stillwater, OK
2019

Submitted to the Faculty of the
Graduate College of the
Oklahoma State University
in partial fulfillment of
the requirements for
the Degree of
MASTER OF SCIENCE
July, 2021

PROJECT MONARCH:

THE APPLICATION OF LUDWIG PRANDTL'S BELL-CURVE

SPAN LOADING

TO A

STRAIGHT, HIGH PERFORMANCE SAILPLANE WING

Thesis Approved:

Dr. Jamey D. Jacob

Thesis Advisor

Dr. Ryan Paul

Dr. Aaron Alexander

Dr. Andrew Arena

ACKNOWLEDGMENTS

I would like to thank my advisor, Dr. Jamey Jacob, who has been a great professor through my undergrad and graduate career, and has mentored me for years. My academic committee members, Dr. Aaron Alexander and Dr. Paul, who have supported my research endeavors with time and commitment since the conception of this project. My committee member Dr. Andrew Arena, who sparked my love for aircraft design with my capstone project and has been a great professor since.

Thank you to the Oklahoma State University Unmanned Systems Research Institute for assisting with the fabrication and sponsoring this project, as well as providing critical lab space for future aircraft fabrication.

The computing for the high-fidelity analysis for this project was performed at the High Performance Computing Center at Oklahoma State University supported in part through the National Science Foundation grant OAC-1531128.

Thank you to my family and close friends for supporting me through my undergraduate and graduate programs, for their deep understanding and support to my educational and professional endeavors. To Scott Weekley, my design partner and good friends, for assisting and supporting as we tackled our bell-curve related design projects; couldn't have had a better partner. To AJ Burba and Taylor Mitchell for consistent communication and support for building materials and software assistance.

Acknowledgments reflect the views of the author and are not endorsed by committee members or Oklahoma State University.

Name: COLE KELLY

Date of Degree: JULY, 2021

Title of Study: PROJECT MONARCH: THE APPLICATION OF LUDWIG PRANDTL'S BELL-CURVE SPAN LOADING TO A STRAIGHT, HIGH PERFORMANCE SAILPLANE WING

Major Field: MECHANICAL AND AEROSPACE ENGINEERING

Abstract: This thesis focused on the design considerations and application of Ludwig Prandtl's 1933 bell-curve span load to a high performance, straight aircraft wing. Sailplanes are designed to maximize lift-to-drag ratio and reduce induced drag through a combination of planform optimization and airfoil selection to maximize performance. This project took an existing sailplane and redesigned its wing, favoring a bell curve lift distribution instead of the original elliptical lift distribution. The new wing aimed to further reduce induced drag by 11 percent and create proverse yaw while maintaining the same root bending moment as the original wing, to result in a more aerodynamically efficient aircraft of the same weight and structure. Major aerodynamic design choices were determined using Prandtl's Lifting Line Theory, low-fidelity analysis using Avena Vortex Lattice and XFLR5, and high-fidelity Computational Fluid Dynamics results utilizing Oklahoma State University's High Performance Computing Center. Structural design was completed using Solidworks, and the manufacturing and testing of the new aircraft wing will be compared to the existing performance values of the original sailplane wing, to prove the increased performance seen during the design stage.

TABLE OF CONTENTS

LIST OF TABLES

LIST OF FIGURES

CHAPTER I

INTRODUCTION

For years, the elliptical lift distribution has been the industry standard when it comes to achieving optimum aerodynamic efficiency and decreasing the amount of induced drag produced by lift. In 1922, Ludwig Prandtl published his Lifting Line theory in English, which allowed for a simple way to calculate lift and induced drag for a wing of finite span [19]. The optimization of his theory resulted in an elliptically shaped lift distribution, which was deemed the most efficient of any span loading for a single wing [2]. This knowledge was taken and applied to many popular aircraft over the next 100 years.

Arguably the most famous aircraft to adopt this theory visually was the popular British World War II aircraft, Spitfire, which had an elliptically shaped wing to achieve peak efficiency (*See Fig. 1*). Obtaining an elliptical lift distribution, or maximum efficiency factor, can be obtained by designing an elliptical wing while holding airfoil cross section and wing twist constant, or changing the airfoil and wing twist to match the elliptical span load shape. When considering wings with little to no geometric twist, the planform shape has a direct influence on the shape of the span loading.

Figure 1: the Supermarine Spitfire, 9th Production Mk I (1938), which created an elliptical span loading through its unique planform shape

But in 1933, Prandtl published a lesser known paper with a superior lift distribution, claiming that any other lift distribution produced more induced drag, including the elliptically-shaped distribution from his previous work [13]. The difference in span loadings can be seen in *Fig. 2* Because the theory was never published in English, it didn't have the same effect as his work in 1922. In this publication, he described a bell-curve shaped lift distribution that decreased induced drag by an additional 11 % while removing the span constraint, and instead constraining root bending moment. It was found that the resulting optimal bell-curve shape described by Prandtl in this work leads to an increase in span of 22 % over it's elliptical equivalent when the span constraint is removed, but because more lift is being generated at the root rather than the tip, the theoretical structural weight is held constant due to both the elliptical and bell-curve span loads having the same root bending moment.

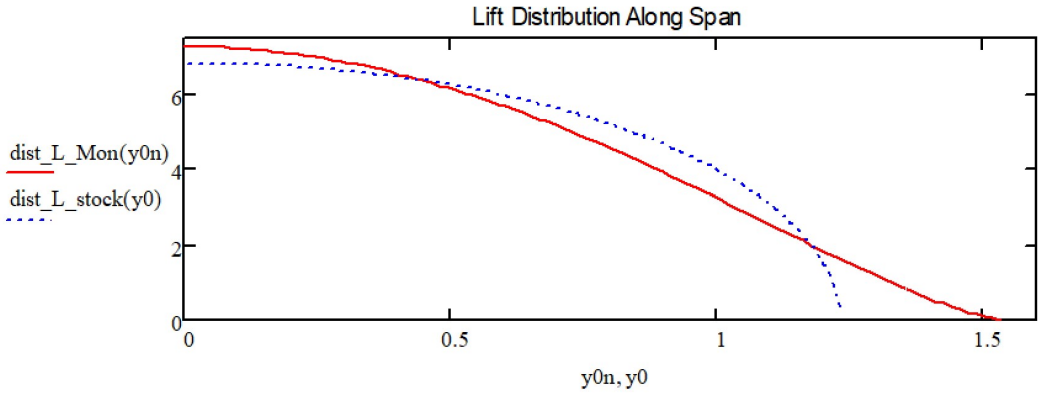

Figure 2: Lift Distribution of Monarch1 (first iteration) and Elliptical Distribution for same lift generation

Overall, the consensus is that for a given structural weight, the bell-curve lift distribution is the most efficient. Regardless, this theory is not as widely known or accepted as his previous work with elliptical lift distributions, even though it points to a new golden standard for designing aircraft wings. Given the nature of the current aircraft industry, limitations on wingspan and spar effectiveness are considered during the design phase and suggest the superiority of the elliptical lift distribution. Although a bell-curve lift distribution is ideal, designing a wing to achieve this can be challenging. Similar to that of the elliptical distribution, this can be done through changing chord distribution of the wing, adding geometric wing twist, varying the airfoil cross section along the span of the wing, or a combination of all three.

This comes with caveats in the form of other design considerations. For example, a bell-curve lift distribution implies that the lift generated at the wingtips trails to zero. Unless the chord tapers to a point, which can cause a multitude of problems with stall, a larger chord is necessary, and an aggressive twist is needed to achieve zero lift; the wingtip needs to be set at the local airfoil's respective effective zero lift angle of attack. Because of this downward twist, our resultant lifting force vector is now directed forward and creates a transition zone near

the 3-quarter span point where downwash becomes upwash, which forces tip vortices towards this point along the span. Analyzing induced drag created along the span demonstrates the wing's ability to create proverse yaw in a coordinated turn. Aggressive wing twist or airfoil variation, although will help the plane make more stable turns, will additionally change the profile drag, will require additional analysis for stability considerations, and require complex manufacturing to achieve. Another design consideration is the lack of span constraints in the calculation, and replacing it by constraining the bending moment being created at the root, which in turn suggests the amount of structural weight for an elliptical and bell-curve lift distribution of the same magnitude be constant. Because more lift is being generated at the root for a bell-curve span loading, a more aggressive twist is needed, or a larger chord length. Similar to the effects from creating the bell shape described first in this section, increasing the span or chord length and increasing the wing area as a result, also increases the amount of total drag being generated, even though induced drag is decreasing. But, if the optimal balance between airfoil selection, geometric wing twist, and chord taper is achieved, while using a simple and intentional manufacturing process, the overall aircraft design can benefit greatly from the decreased amount of induced and overall drag. This process will be detailed in this body of work.

Figure 3: Global Hawk Top View

Aircraft that will see the largest benefit from reduced induced drag are aircraft that operate at low air speeds, perform long endurance missions, or rely on maximum aerodynamic performance for other mission requirements. This includes HALE (high altitude long endurance) aircraft and UAVs, performance aircraft that maximize lift-to-drag such as sailplanes and gliders, and any aircraft that operate in low Reynolds number regimes. A great example of a HALE UAV that already demonstrates increased aerodynamic performance is the Global Hawk (*See Fig. 3*)

The focus of this thesis is on the benefits of increased aerodynamic performance for Un-

manned vehicles, particularly ones that are considered low Reynolds number aircraft. One common similarity between HALE UAVs and sailplanes is the optimization for performance: to reduce drag and increase range and endurance. One manifestation of this is an increased Aspect ratio for both classifications of aircraft. Aspect ratio is the ratio between the span squared and the planform area; increasing aspect ratio makes the wings longer and reduces chord length, resulting in "skinnier" wings, and generally leads to an increase in performance through a reduction in induced drag. To increase aerodynamic performance, it is assumed that well-designed aircraft from both classes push to increase aerodynamic efficiency, and in turn are designed to match an elliptical lift distribution due to constrained wingspans.

Because of this, the best way to prove the validity and feasibility of the bell-curve lift distribution, is to take an existing high performance aircraft with an elliptically-based lift distribution, modify the wing to have a bell-curve lift distribution, and use a combination of low-fidelity analysis, high-fidelity CFD analysis, and flight test data to compare the two wings for the same aircraft. Keeping in mind scale and cost, this body of work will look to modify an existing hobby sailplane's wing, which was chosen over a more expensive HALE UAV, to achieve the same goal. Using a cost-effective and simple air frame to modify and prove Prandtl's theory is the best and most responsible way to explore the potential benefits of Prandtl's inviscid drag reduction methods. The Volantex ASW28 RC sailplane was selected to be modified, and can be seen in *Fig. 4*). The current wing, which will be referred to throughout as the "Stock" wing, is 8.33 ft in length, 4 square feet in area, generates 3lbs of lift in cruise flight around 36 ft/s, and has a variable-taper design with a constant airfoil cross section and no wing twist to achieve a near-elliptical lift distribution.

Figure 4: Volantex ASW28 Top View

The goal of this research project is to redesign a high performance sailplane wing with a bell-curve lift distribution in order to validate the results found by Ludwig Prandtl in 1933, and explore the potential benefits of implementing it into modern aircraft designs. This will be achieved by demonstrating Prandtl's 11 % reduction in induced drag and propose a wing design that decreases overall drag on the same order of magnitude, manufacture the wing using a combination of composites and 3-D printing, and proving the performance

increase through real flight data of both wings on the same aircraft. All design theory, design processes, and results will be detailed in this body of work. This will be achieved in 3 phases:

1. Phase I: Using Lifting Line Theory and the governing equations and assumptions associated with Prandtl's work on the bell-Curve lift distribution, derive an algorithm that solves for wing twist necessary to create the span loading using major geometric characteristics of an aircraft's planform.

2. Phase II: Using Low fidelity analysis tools, explore several different planform configurations constrained by an existing aircraft's wing geometry and implementing the bell-curve span loading, and select the configuration with the highest aerodynamic performance. The following wing configurations will look at changing taper, airfoil cross section and/or distribution, and geometric wing twist to create a bell-curved span loading, while maintaining the same design CL value, a constant wing area, and a constant root bending moment so no additional structure is needed to compensate for the new wing design In this phase, validation of the theoretical reductions in induced drag will be priority, and reductions in overall drag by optimizing a new airfoil for the planform will be considered and compared.

3. Phase III: Using high fidelity Computational fluid dynamics analysis in STAR-CCM+, analyze the selected wing geometry to validate results found in low fidelity analysis. Validation will be successful if:

   (a) Lift Distribution for a given C_L value matches low fidelity analysis results

   (b) Total drag coefficient matches closely to that found in low fidelity analysis

   (c) The aircraft vorticity shed profiles matches previous research efforts on bell-curve loaded wings and the work of Ludwig Prandtl

4. Phase IV: Use advanced construction methods to manufacture the new wing design to match the weight of the original aircraft's wings, design the wing to seamlessly integrate into the existing aircraft's fuselage, and gather flight test data to validate overall drag reduction through an improved endurance figure at the designed cruise condition. This phase will likely belong to the future work section.

CHAPTER II

LITERATURE REVIEW AND PREVIOUS WORK

2.1 Literature Review

Detailed here is an introduction to the bell-curve lift distribution and information regarding previous research efforts into its applications and benefits. It's important to compare the bell-curve lift distribution (referred to as the BCLD) to it's predecessor, the elliptical lift distribution, and key areas it can be implemented to fully benefit from its performance improvements. These studies include several different aircraft that have adopted the BCLD, as well as the analysis techniques used to design and analyze the wings to prove performance enhancements. Subsequent studies are not limited to: showing the proverse yaw control characteristic of BCLDs, development of straight and swept flying wings to adopt the BCLD, and different analysis solvers and resulting performance.

2.1.1 Prandtl's Bell-Curve Theory

"Über Tragflügel kleinsten induzierten Widerstandes", translated to English as "Concerning Wings for Minimum Induced Drag", was Ludwig Prandtl's 1933 publication further exploring his previous work concerning the minimization of induced drag for a finite wing. His previous work stated, for a given amount of lift generated with a constrained wingspan, achieving the smallest amount of induced drag is achievable through an elliptical lift distribution [13]. Normally, when designing an aircraft, there are many reasons for having a constrained wingspan: manufacturing capabilities, spar sizing, requirements such as "passing through a particular bay door", wing loading and material restrictions, to name a few. But Prandtl knew a wing that induced drag was progressively reduced the larger the wingspan and aspect ratio became, theoretically. Spar sizing and weight becomes an issue when extending to "infinity" from the root location, and this loading would have to be considered when analyzing the wing; any addition of spar weight meant more required lift generation to compensate, and due to downwash effects established in his previous work, this meant inherently more drag.

Knowing this, instead of constraining the wing design by wingspan, Prandtl prescribed the amount of lift being generated and the moment of inertia of the wing as limiting factors. The moment of inertia created by the wing included the lift-generated load and the spar weight at each location along the wing's span, which was directly proportional to the bending moment at the given location. The goal is to minimize the product of density and total circulation generated by the wing, declared by Prandtl as W_i meaning L/V_∞, by holding the

generated amount of lift and bending moment constant. The constraints are shown below, where Γ is the circulation and y_0 is the location along the span.

$$L = \rho_\infty V_\infty \int \Gamma \, dy_0 \tag{2.1.1}$$

$$I = Lr^2 = \rho_\infty V_\infty \int \Gamma y_0^2 \, dy_0 \tag{2.1.2}$$

$$D_i = \rho_\infty \int \Gamma w \, dy_0 \tag{2.1.3}$$

Shown above are the equations for lift, wing inertia, and lift generation, with air density ρ, air speed V, radius of gyration r, downwash w, and circulation Γ. From this, Prandtl concluded that for a wing generating a certain amount of lift and root bending moment, but not limited by wingspan, the ideal lift distribution shape solved for resembled that of a "tapered wing", not an elliptical one. Instead of the elliptically shaped lift distribution in his previous work, the new lift distribution generated more lift at the root of the wing, which trailed to zero lift generation at the wingtips - the bell curve lift distribution.

From derivation of the above equations, defining the circulation at the root as Γ_0, and defining the ratio of circulation across the span as μ, Prandtl defined span, root circulation, and induced drag as:

$$b = 4r\sqrt{\frac{1-\frac{\mu}{4}}{1-\frac{\mu}{2}}} \tag{2.1.4}$$

$$\Gamma_0 = \frac{L}{\pi\rho V_\infty r}\sqrt{\frac{1-\frac{\mu}{2}}{(1-\frac{\mu}{4})^3}} \tag{2.1.5}$$

$$D_i = \frac{L^2}{8\pi\rho V_\infty^2 r^2}\frac{(1-\frac{\mu}{2})(1-\frac{\mu}{2}+\frac{\mu^2}{4})}{(1-\frac{\mu}{4})^3} \tag{2.1.6}$$

The minimum value of this function occurs when μ is equal to 1, and this results in the right most fraction in equation 2.1.4 being equal to 0.888, root circulation equal to 1.088 of the original, and span equal to 1.2247. Knowing this, and comparing two wings with the same lift and bending moment, a bell-curve lift distribution allows for the wingspan to increase by 22 %, and achieves 11 % less induced drag than its elliptical counterpart [4][13][10]. The comparison between the span loadings, as well as the performance benefits as a function of μ can be visualized in *Fig. 6*. This same performance increase, span increase, and bell-curve shape will be pursued in the design portion of this thesis.

A similar result to Prandtl's was later concluded by Robert T. Jones in 1950, which stated that a 15 % decrease in induced drag could be achieved with a 15 % increase in

	$f(\mu)_b$	$f(\mu)_{\Gamma_0}$	$f(\mu)_{D_i}$
μ	$\sqrt{\frac{1-\frac{\mu}{4}}{1-\frac{\mu}{2}}}$	$\sqrt{\frac{1-\frac{\mu}{2}}{\left(1-\frac{\mu}{4}\right)^3}}$	$\frac{\left(1-\frac{\mu}{2}\right)\left(1-\frac{\mu}{2}+\frac{\mu^2}{4}\right)}{\left(1-\frac{\mu}{4}\right)^3}$
0.00	1.000000	1.000000	1.000000
0.25	1.035098	1.030498	0.945778
0.50	1.080123	1.058080	0.909621
0.75	1.140175	1.079456	0.892126
1.00	1.224745	1.088662	0.888889

Figure 5: Variation in $\mu and results in gspan, circulation, and induced drag changes$

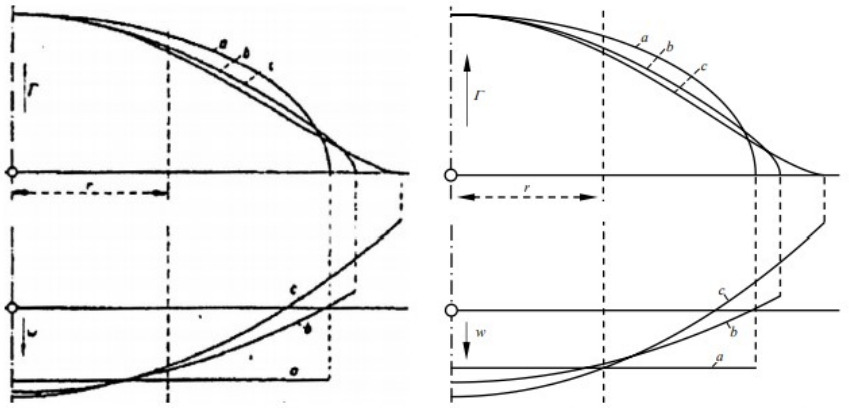

Abb. 1. Verlauf der Zirkulation und der Abwärtsgeschwindigkeit *a* Elliptische Verteilung, *c* beste Verteilung; *b* ein zwischen liegender Fall.

Fig. 1. Trend of the circulation and downwash. *a* elliptical distribution, *c* optimum distribution; *b* intermediate case.

Figure 6: Comparison between original figure from 1933 and translated and updated figure from 2020

wingspan over a similar elliptically loaded wing [12]. This was achieved by Jones by constraining the same variables: Root bending moment (wing inertia from lift and structural weight in Prandtl's work) and lift. Designing around these constraints, as well as several others, has been exemplified in work using Jones and Prandtl as a foundation since [11], but the fundamental constraints held by Jones, as previously discussed, are the most important when considering the application of the span-loading to other aircraft configurations. His equation for minimum induced drag, relating elliptical and non-elliptical wingspan ratios, S and S_e, is given below.

$$D_i = \frac{L^2}{\pi \frac{\rho}{2} V_\infty^2 (2S_e)^2} [8(\frac{S_e}{S})^4 - 16(\frac{S_e}{S})^3 + 9(\frac{S_e}{S})^2] \tag{2.1.7}$$

The minimum of this function without exceeding the root bending moment anywhere along the span is achieved when $S/S_e = 1.33$, and this can be seen in *Fig. 7*. Lower induced drag ratios are believed to be achieved past this point, but force distribution along the span when it exceeds 150% of the original, S_e, causes larger negative bending moments along the structure, and although root bending moment is constant, the structure cannot hold these induced moments.

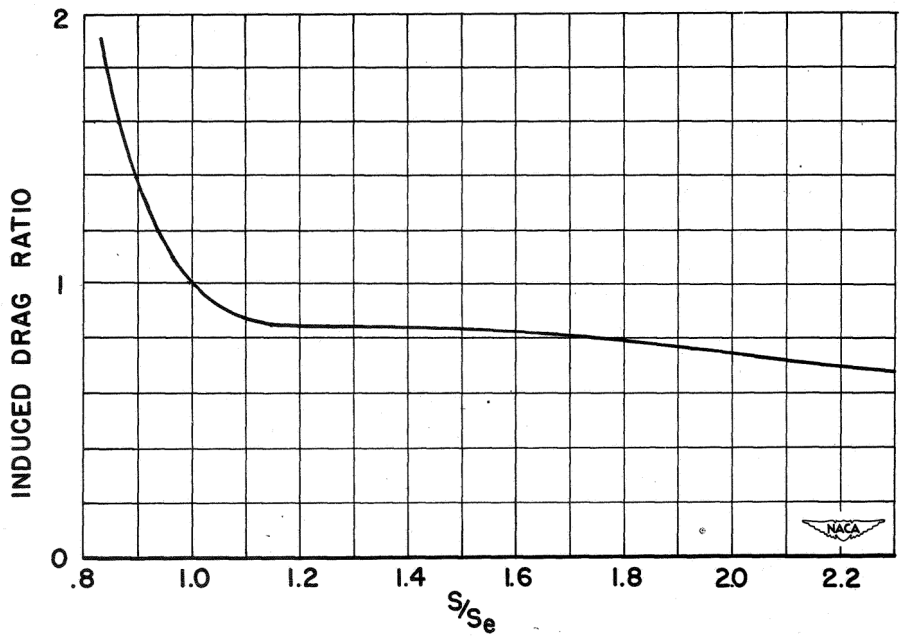

Figure 7: Ratio of Elliptical and non-elliptical wingspans to induced drag ratio, from Robert Jones

2.1.2 Introduction to Applied Bell-Curve Span Loads: The Prandtl-D

Ludwig Prandtl's bell-curve theory gained significant recognition with the development of two NASA aircraft in 2017, headed by Dr. Bowers [4]. After a significant analysis of Prandtl's 1933 theory, it was concluded that the manipulation of the outboard wing geometry manifested into the creation of induced thrust at the wingtips [13]. With an elliptical lift distribution, downwash created as a result of circulation, γ, is constant along the wing. The presence of constant downwash results in a horizontal force component of the overall resultant force, and is the source of induced drag along the span of the wing. With a bell-curve lift distribution, there exists a transition from downwash to upwash near the 70 % span location. The resultant force in this outboard area of upwash is directed forward over the vertical YZ plane, and creates induced thrust at the wing tips, which can be visualized in *Fig. 8*. This induced thrust decreases the overall horizontal drag force induced by lift, and theoretically lowers the wing's induced drag coefficient. They concluded from Prandtl's publication

in 1933 that the desired bell-curve lift distribution could be modeled with the equation below.

$$\Gamma = \Gamma_{y_0}(1 - x^2)^{\frac{3}{2}} \tag{2.1.8}$$

For design purposes and change in nomenclature, this equation was interpreted and changed. The new form of the equation is shown below, which defines the lift distribution as a function of semi-span location and local lift distribution at the wing root, $L'_{y_0=0}$. Γ is changed to L' due to the Kutta-Joukowski condition, and assuming air density ρ_∞ and cruise velocity V_∞ are constant.

$$L' = L'_{y_0=0}[1 - (\frac{x}{b/2})^2]^{\frac{3}{2}} \tag{2.1.9}$$

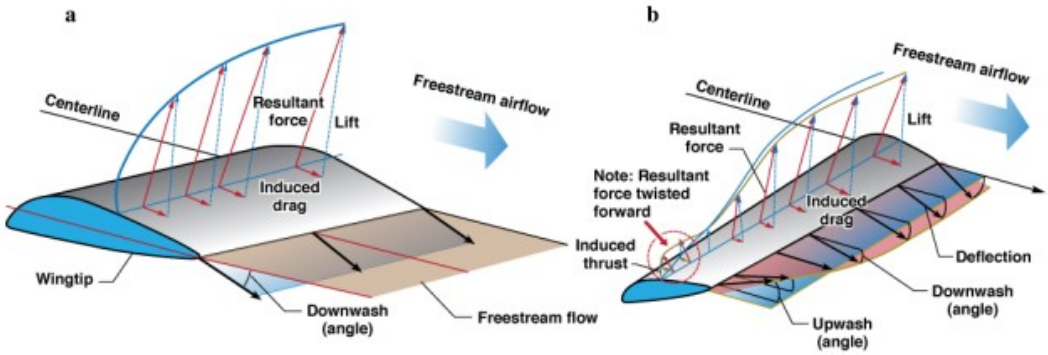

Figure 8: Resultant Force Vectors: Elliptical v Bell-curve Span Loading (Bowers)

The resultant force's vertical component is lift, and induced drag is the "consequence" of producing lift. This is true for both induced drag and induced thrust; as lift increases, induced drag on the inboard wing section increases, and induced thrust on the outboard section of the wing increases. Control surfaces that increase lift in this region, such as ailerons or flaperons, also have the potential for increasing thrust, so downward (positive) deflection of an aileron in the upwash region of a bell-curve wing induces a yawing moment on the aircraft. In a coordinated turn, which involves opposite and equal deflection of ailerons, proverse yaw can be created from an increase in induced thrust at one wing tip, which allows an aircraft to yaw in the direction it's rolling. Normally for an elliptically loaded wing, increasing lift on one wing also increases drag, which in turn creates adverse yaw. This is usually overcome by a rudder or similar control surface in the rear of the aircraft, so the aircraft can yaw in the same direction it's rolling in.

A significant part of Bower's theory uses the creation of proverse yaw and the assumption that bird have a bell-curve span loading to explain why they're capable of creating coordinated turns without the use of a yaw device, such as a rudder. This same theory applied to an aircraft means that an optimal aileron size and placement could create enough proverse

yaw to entirely eliminate the need for a vertical stabilizer or yaw device in cruise, which would also in turn decrease the overall structural weight and drag being produced by an aircraft.

Figure 9: NASA's Prandtl-D in flight, designed and built by Dr. Bowers and his team

Dr. Bowers and his team applied this theory to two sub scale flying wing aircraft, using geometric twist to achieve the desired bell-curve shape. Airfoil twist varied between 8.3 degrees and -1.7 degrees from root to tip. The chosen planform shape was Horten's H XC aircraft at 25 % scale. Both aircraft were designed and developed to demonstrate coordinated turns and proverse yaw creation in flight without the use of vertical stabilizers of any kind. Each aircraft was remotely controlled and bungee-launched into a glide, averaging a minute and a half flight time. One of the aircraft, the 12.5 ft flying wing Prandtl-D, is shown in *Fig. 9*. Flight test data showed that the aircraft were yawing in the same direction of banking, proving the creation of proverse yaw and performance of coordinated turns. The scale, overall design, and design theory was applied and built on by Scott Weekley and Cole Kelly (myself) for the development of Bellwether in 2020.

The Bell-curve span loading has been applied to several other experimental aircraft in recent years, including a forward swept supersonic wing, an oblique wing, and a double wing, each with it's own successes and failures [8] [21] [6]. The most promising example of the application of this unique span load past the Prandtl-D developed by NASA is the straight flying wing, Biom.

2.1.3 Maximizing Proverse Yaw: The Biomimetic Flying Wing

The topic of wing design manipulation to increase the amount of proverse yaw was studied by Jonathan Richter and his group at Washington University in 2019, which supported Kevin

Hainline's development of a straight flying wing called the Biom. Because aircraft with bell-curve span loading can perform coordinated turns in flight through inducing thrust at the wing tips, this demonstrated the idea that unswept wings could maintain lateral directional stability in flight without the need for rear stabilizers, and provides the motivation behind this thesis document. Even though rear stabilizers aren't needed for flying wings, this suggests that straight wings implementing the same span load could result in smaller, les necessary vertical stabilizers. Work has been done in this area by Martin Carrizalez, who instead of focusing on flying wings, sought to minimize the size of the vertical stabilizer by optimizing non-elliptical lift distributions, specifically modified bell-curve shaped span loads [5]. Results showed that Bell-curve lift distributions applied to new wing designs offered a 44.3 % decrease in vertical stabilizer weight.

Mentioned within the work of Kevin Hainline at Washington University, were several interesting benefits from a straight flying wing against a swept flying wing, such as Dr. Bower's Prandtl-D aircraft. In summary, straight flying wings with similar wing geometries and flight conditions as swept flying wings have more performance improvements.

First, low-fidelity analysis suggests that efficiency is tied closely to $\cos \Delta$, so a flying wing like the Prandtl-D (with a quarter chord sweep angle of 20 degrees) has a 6% reduction in aerodynamic performance. From a control standpoint, the difference is more subtle: flying wings need to be highly optimized when carrying payloads, since control surface deflection is needed to trim the aircraft, and control surface deflection can negatively impact the lift distribution and drag of the aircraft in cruise. Although the pitch control of a swept flying wing is considerably higher, Hainline and Richter believe that straight, morphing wings and highly optimized wing geometries, with the proper flight controller, can overcome this disadvantage to achieve higher aerodynamic performance [9]. And comparatively, birds (who are believed to have bell-curve lift distributions and also have straight wings, per Bowers [4]) can make beautiful coordinated turns and demonstrate pitch control without vertical stabilizers or large pitch "control surfaces". Also, without the additional induced drag or stabilizer drag needed by an elliptically loaded wing, a straight tapered flying wing has increased performance and efficiency over its elliptical counterparts [20].

The study done by Richter was conducted using a straight tapered bio-mimetic flying wing as the initial geometry, and modifications to the aircraft's wing geometry was made in order to measure the resulting proverse yaw generated in coordinated turns (*See Fig. 10*) . This was done by varying taper ratio, wing chord, wing length, twist distribution at the wingtips, and outboard control surface sizing of the original vehicle, which was developed by Hainline in 2017 to study the lateral-directional control space for unswept flying wings [9]. Each variation in the aircraft used a combination of geometric and aerodynamic angle of attack to fit the bell-curve lift distribution detailed by Prandtl in 1933 (*See Fig. 13*), and initial testing of the most effective control surface deflection angle was conducted using OpenVSP (a open source numeric panel solver). Both Hainline and Richter used XFLR5, a low-fidelity analysis tool utilizing a built in Vortex Lattice method, VLM2. The results can be seen in *Fig. 11*.

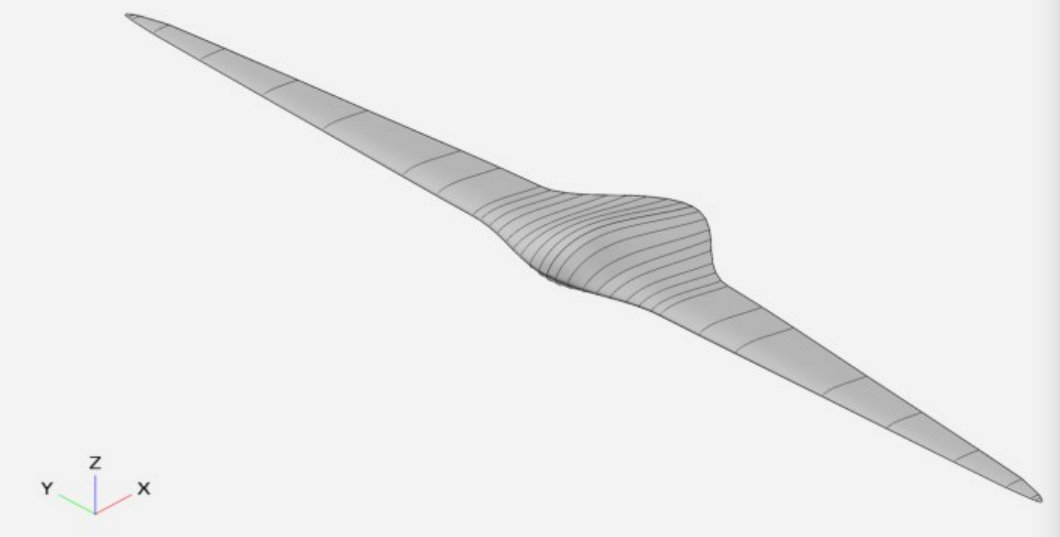

Figure 10: The original Biomimetic straight tapered flying wing before modification

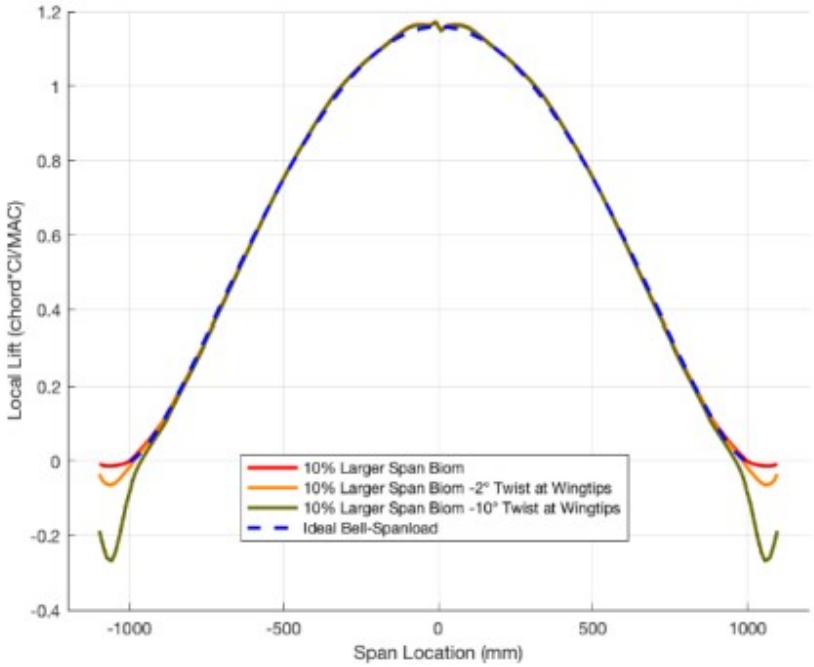

Figure 11: Several different varied lift distribution shapes explored by Richter

Results showed that every variation in wing geometry resulted in a considerable increase in proverse yaw power, which was measured by comparing yaw moment coefficient, C_N versus lift coefficient, C_L. It was also concluded that the maximum proverse yaw control power exists between 76 and 82 % of the semi span, just outboard of the mid-span vortex seen at the transition point between downwash and upwash. This occurs near the 70 % semi span location. Wings with changed geometry that moved the mid-span vortex towards the root generally had more proverse yaw control power, since the region of upwash was larger and therefore increased induced thrust with aileron deflection, and this was seen in the models

that had 20 % larger control surfaces and 10 % larger span (*See Fig. 12*). But, conclusive evidence of this breaks down when considering the models with 30 % larger and smaller wingtips, and these changes to the wing's geometry did not correlate with any proportional increases in proverse yaw control power. Models that have control surfaces ranging the entire upwash sections created large downwash sections saw neutralized proverse yaw creation. Richter concluded that a wing with 10 % more span and 10 % more twist, with control surfaces spanning 80 - 100 % of the outboard semi span produced 16 times more proverse yaw control power than the original configuration [20].

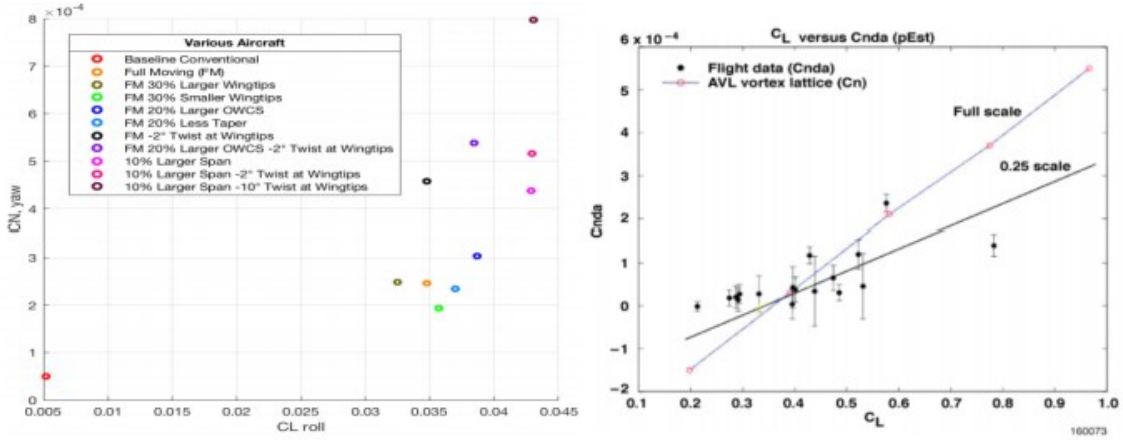

Figure 12: A comparison between Richter's proverse yaw control power figures and measurements from Dr. Bowers

This study, although focusing entirely on proverse yaw control, shows the efficacy of a controllable, stable, straight flying wing with a bell-curve span load. Because the modified aircraft for this thesis will have a fuselage and tail for pitch control, pitch control is not as closely considered for the Monarch wing. Although, because little work has been done on the stability of straight wings with bell-curve span loads, Richter's study adds more confidence for building and flight testing the new Monarch wings without rigorous stability analysis. What Richter's results lack, is the performance proof; understandably, a straight flying wing with no control or stabilizing surfaces needs to be able to perform coordinated turns in flight, but there was no comparison to an elliptically loaded tube-and-wing aircraft that's capable of the same mission. Achieving a morphing wing geometry, from a materials and mechatronics perspective, is incredibly difficult and was not discussed in Richter or Hainline's work, and this consideration needs to be a part of this body of work. Hainline's work also doesn't specify how closely the actual aircraft's lift distribution matches Prandtl's bell-curve distribution, and only provides a "theoretical" lift distribution. Most importantly, Hainline's work doesn't discuss it's performance benefits over any other aircraft.

What Monarch seeks to prove, is that a tube-and-wing aircraft with a straight, bell-curve span load, can outperform its straight and swept flying wing and elliptical tube-and-wing counterparts. The development of Biom and its complex (and potentially heavy) morphing and control considerations for the given mission could have been avoided by choosing

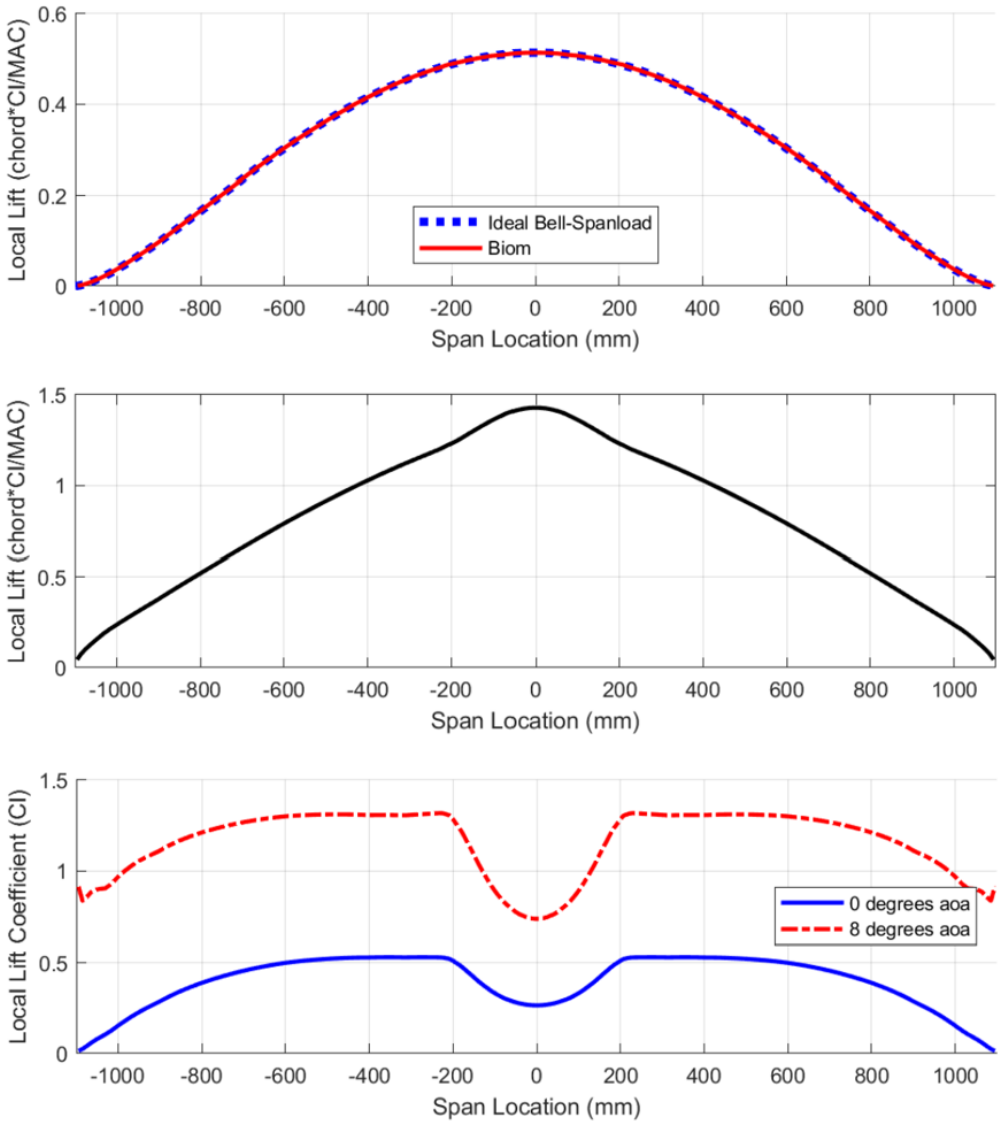

Figure 13: Biom's Lift Distribution (assumed), calculated Local Lift Near Stall (8 degrees aoa), and Local Lift Coefficients for 0 and 8 degrees aoa

a conventional aircraft configuration with the performance improvement of a bell-curve lift distribution. Monarch, which is designed to achieve this, has a low drag fuselage and tail, which offers even more pitch control and stability simplicity than Biom without considerable drag increase, internal complexity, or alteration to the wing's lift distribution.

2.1.4 Wrapping it Together: Bellwether, The New Flying Wing

Recently, the application of a bell-curve lift distribution has been explored by Scott Weekley and Cole Kelly (myself) at Oklahoma State with the development of Bellwether, a 26ft flying wing that draws inspiration from the work of Dr. Bowers at NASA and seeks to further

improve the performance of flying wing aircraft with bell-curve lift distributions (*See Fig. 14*). To maintain a connection to NASA's Prandtl-D aircraft, the chosen constraint was the geometric layout and planform shape of the aircraft, and the scale was chosen based off of potential applications of the aircraft at Oklahoma State. Also characteristic of Dr. Bower's flying wing was the lack of vertical stabilizers, in the form of a rear tail or wingtips. Aside from reducing induced drag further, demonstrating proverse yaw for coordinated turns was a large milestone to hit.

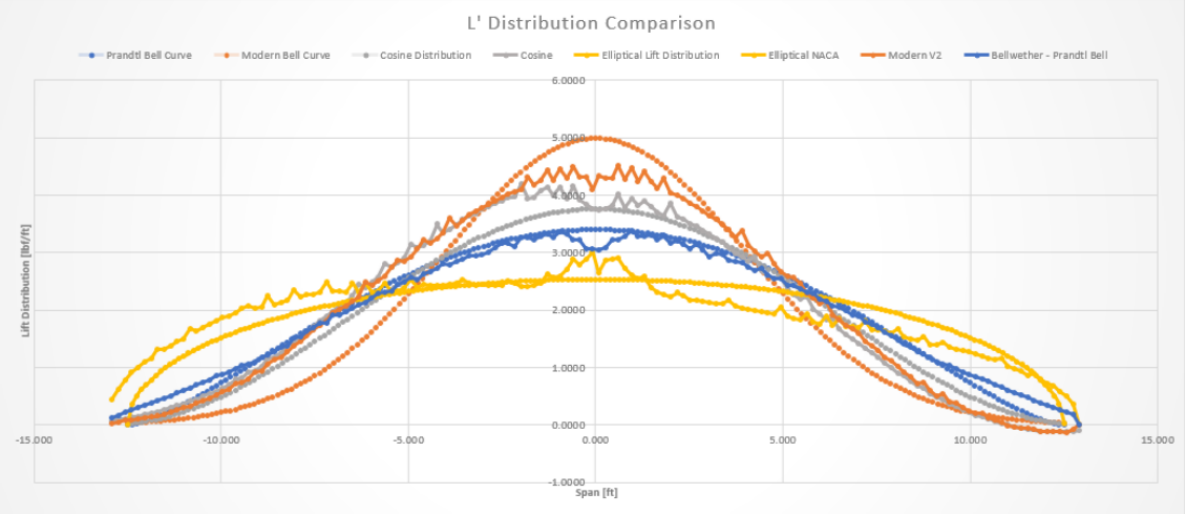

Figure 14: Bellwether Case Study: Comparison between Theoretical and CFD Lift Distributions

Aerodynamic analysis included a study conducted on the effects of different bell-curve shape variations that allowed for the same amount of lift generated at a given flight regime, then solved for the geometric twist values using a modified 3-dimensional lifting line theory and Vortex Lattice method to account for the sweep, inspired by the work of Phillips at Utah State University [18]. Analysis started by an airfoil down-select, of which a modified NACA2412 and Wortmann FX 74-CL5-140 hybrid, named Bellwether1, was chosen for the wing's root airfoil. This new airfoil has familiar ties with the Albatross, of which Dr. Bowers used as a perfect example of coordinated bird flight without the use of a vertical tail, which is the goal of flight testing Bellwether [4]. It's shape and similarity to other bird wings can be visualized in *Fig. 15*. The new Bellwether1 airfoil closely resembles the cross section of the albatross wing, and also operates in the low Reynolds number regime [17].

The RAE101 airfoil was chosen for the tip, to keep the amount of geometric twist to a minimum when achieving zero lift. Further design steps included an analysis of the Prandtl bell curve outlined by Ludwig Prandtl in 1933 [19], compared to a Cosine distribution, the Modern Bell curve (found in common statistical bell curve distributions), and an elliptical span loading without a constrained wingspan. The curves were each implemented into a CAD iteration of Bellwether by changing the local geometric angle of attack for ten different semi-span locations, analyzed using low-fidelity results in AVL from XFLR5 and then using

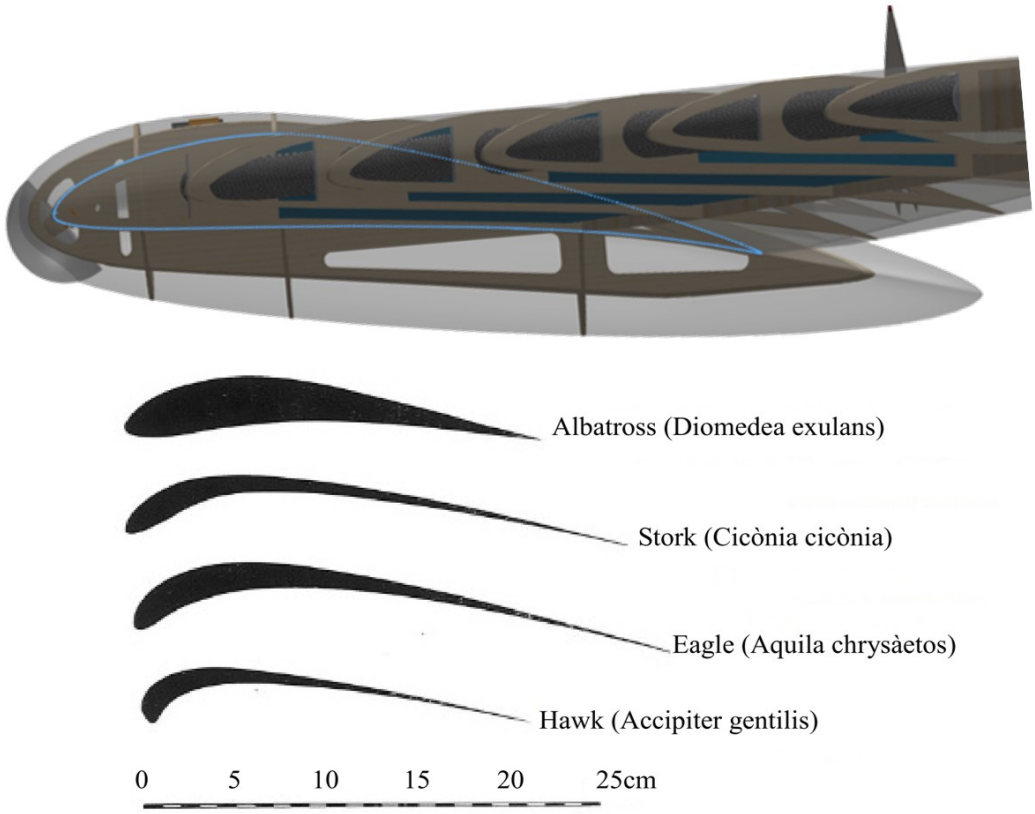

Figure 15: Comparison of Bellwether root airfoil (top) and Albatross wing cross section (bottom)

high-fidelity CFD in STAR-CCM+ with multiple mesh resolutions.

An important takeaway from CFD analysis was the observable trailing vortex location, by creating a vector plane downstream of the wing and observing the magnitude of circulation in that region. This was important for connecting CFD analysis to the theory: A bell-curve lift distribution has a transition point along its semi-span (near 70 %) where downwash turns into a region of upwash. At this transition point is where a majority of the vortex shed is expected to occur (*See Fig. 16*). An elliptical lift distribution, because it has downwash along the entire wing, has a trailing vortex shed directly at the wingtip, where high pressure air slips around the wingtip into the low pressure zone above the wing. When completing CFD analysis, this held true: the elliptical wing had a large circulation spike observable directly behind the wingtips, and the bell-curve lift distribution has a much wider, less intense vortex shed, with the highest amount of circulation at the expected downwash-upwash transition point (*See Fig. 17*).

The results from Scott's work show the 1933 Prandtl bell curve lift distribution giving the highest performance while still maintaining proverse yaw creation, as demonstrated by Dr. Bower's Prandtl-D aircraft, and this specific lift distribution was selected for the final design of Bellwether. At an angle of attack of 0 degrees, Bellwether demonstrated a lift to

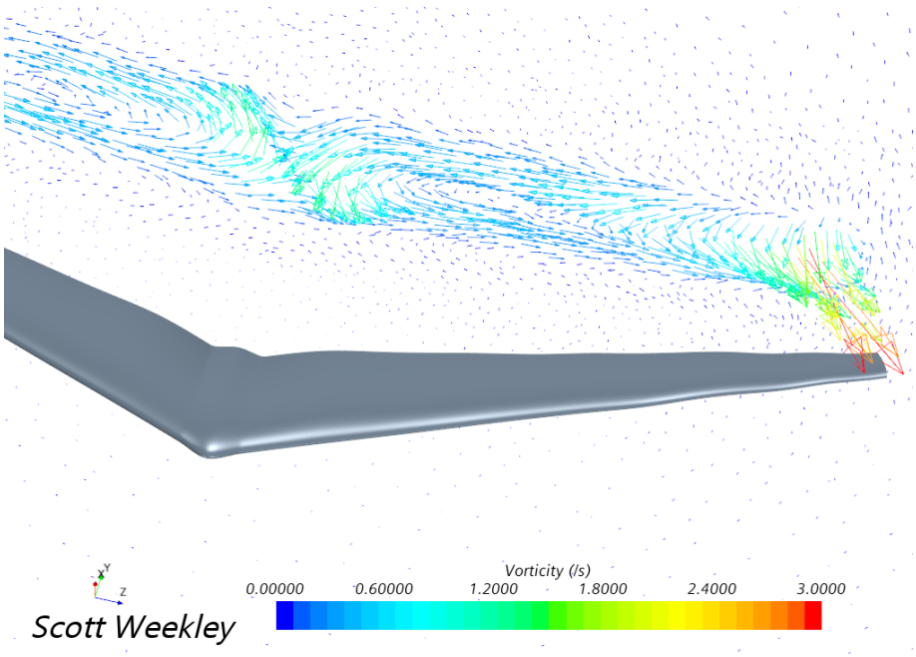

Figure 16: Vorticity Scene of Bellwether with an Elliptical Lift Distribution

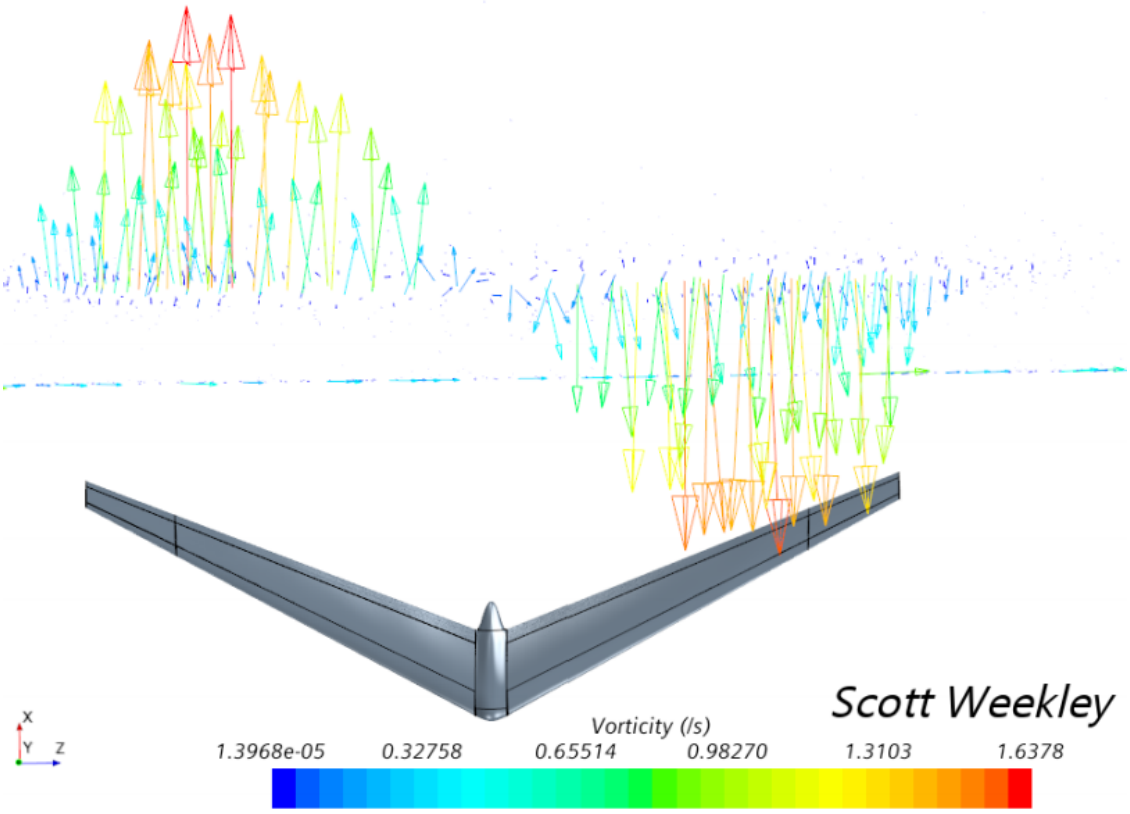

Figure 17: Vorticity Scene of Bellwether with a Bell-Curve Lift Distribution

drag ratio of 20.1, compared to 14.1 for elliptical, 19.1 for cosine, and 16.7 for the statistically based bell curve. Bellwether also demonstrated nearly 0.2 lbf-ft of proverse yaw moment in a coordinated turn compared to the elliptical distribution, which had -1.35 lbf-ft of adverse yaw for the same flight conditions and control surface deflection angle. This was expected, since the elliptical lift distribution has no region of upwash at the wingtips, to modify the force vector for control surface deflection. The modern bell curve and the cosine bell curve's demonstrated a higher amount of proverse yaw, but lift to drag was prioritized over turn coordination for the final model to be manufactured. These were calculated using CFD in STAR-CCM+, which combines induced drag and viscous drag components.

Scott detailed the analysis comparisons between low and high fidelity techniques flawlessly, but the major discrepancy between this study and this body of work, is the lack of wingspan limitations when comparing bell-curve and elliptical lift distributions. Ludwig Prandtl's work explicitly states that bell-curve lift distributions are 11 % more efficient when there isn't a constrained wingspan. As seen in *Fig. 14*, the same planform shape was used for all the lift distributions in the case study, and therefore the same wingspan. As mentioned by Scott in his work, the case for a direct comparison between Prandtl's 1921 and 1933 bodies of work is unsubstantiated here, even if there is a performance increase between the two. The following body of work for Monarch, which details the direct comparison between the elliptical and bell-curve lift distributions, will work to fill in this knowledge gap, and seek to truly compare the two as per the stringent constraints in Prandtl's theory: fix wing area, lift, root bending moment, and increase the wingspan by 22 % to observe an 11 % reduction in induced drag.

Figure 18: Isometric View of Bellwether, Airfoil Variation

Oklahoma State University's Unmanned Systems Research Institute (USRI) is slated to begin manufacturing efforts on Bellwether, in hopes to use the flying wing as a platform for a number of data-gathering projects in the future (as of June, 2021). During the analysis phase of Bellwether, Scott and I were successful in designing the internal structure and unmanned systems integration (*See Fig. 18*). The aircraft is composed of a fiberglass skin with a foam

core, carbon fiber wing spars and Aeroply internals, and a variable electric propulsion system with a modular avionics bay for near-infinite mission customization. Future flight testing of Bellwether will be conducted to prove its analyzed aerodynamic efficiency, coordinated turn performance with its proverse yaw, and gather important data to further study the efficacy of bell-curve lifting bodies.

2.1.5 Analyzing the Bell-Curve Lift Distribution: Computational Fluid Dynamics

Aside from low fidelity tools, such as XFLR5, AVL, and OpenVSP, high-fidelity computational fluid dynamics is needed to further validate results found from lesser tools. Avena Vortex Lattice, a vortex lattice analysis tool developed by MIT, was used as the golden standard by Weekley when designing the initial iterations of Bellwether, and the results from this were cross referenced with results from a similar solver in XFLR5 [22]. Vortex Lattice methods simulate the wing as a set of panels with bound vortices, and allows for rapid calculation of lift and induced drag, but high fidelity tools are needed to estimate viscous drag. Although computationally heavy and time consuming to set up and run, Computational Fluid Dynamics (CFD) is a great tool for getting a more accurate picture of the aircraft's performance.

Weekley used STAR-CCM+ to simulate Bellwether's performance at flight conditions. 3D models of Bellwether were created in Solidworks, and imported into STAR-CCM+. From there, a flow domain several wingspans in radius and length was created, and a mesh was created for the flow domain and wing (*See Fig. 19*). Surface controls and prism layers were added to Bellwether itself, to accurately capture flow in the boundary layer over the wing surface. Once a mesh was created, Weekley set up the flow physics using a coupled flow solver with a steady Reynolds-Averages Navier Stokes (RANS) solver. A mesh independence study was used to validate the results of the solved physics, by increasing the base size of the mesh by 20 %, which yielded a % error of 0.1418 and 0.1346 for lift and drag. This same process will be used during CFD analysis of Monarch, to validate the results of the analysis.

Kyle Lukacovic from California Polytechnics State University used a similar setup in STAR-CCM+ to analyze Dr. Bower's Prandtl-D aircraft in formation flight. This study was designed to find the optimal position for multiple Prandtl-D flying wings, to draw similarities to formation bird flight and study efficiency improvements for stacked aircraft. After creation of the Prandtl-D in Solidworks, it was imported into STAR-CCM+ and a flow domain and surface mesh were created. Unlike Weekley, Lukacovic used a segregated flow solver over the coupled flow solver. Segregated flow solvers solved the RANS equations for pressure and velocity, while coupled solved for mass, moment, and energy. As stated by Lukacovic, the coupled solver can help with convergence for compressible flow, but using this solver for Monarch is unnecessary, since it is considered a low-Reynolds, subsonic aircraft with a Mach of 0.032. For incompressible flow, coupled solvers can take longer to converge to a solution, so for time and computational power, Lukacovic used a segregated solver instead [14]. This will be replicated for Monarch.

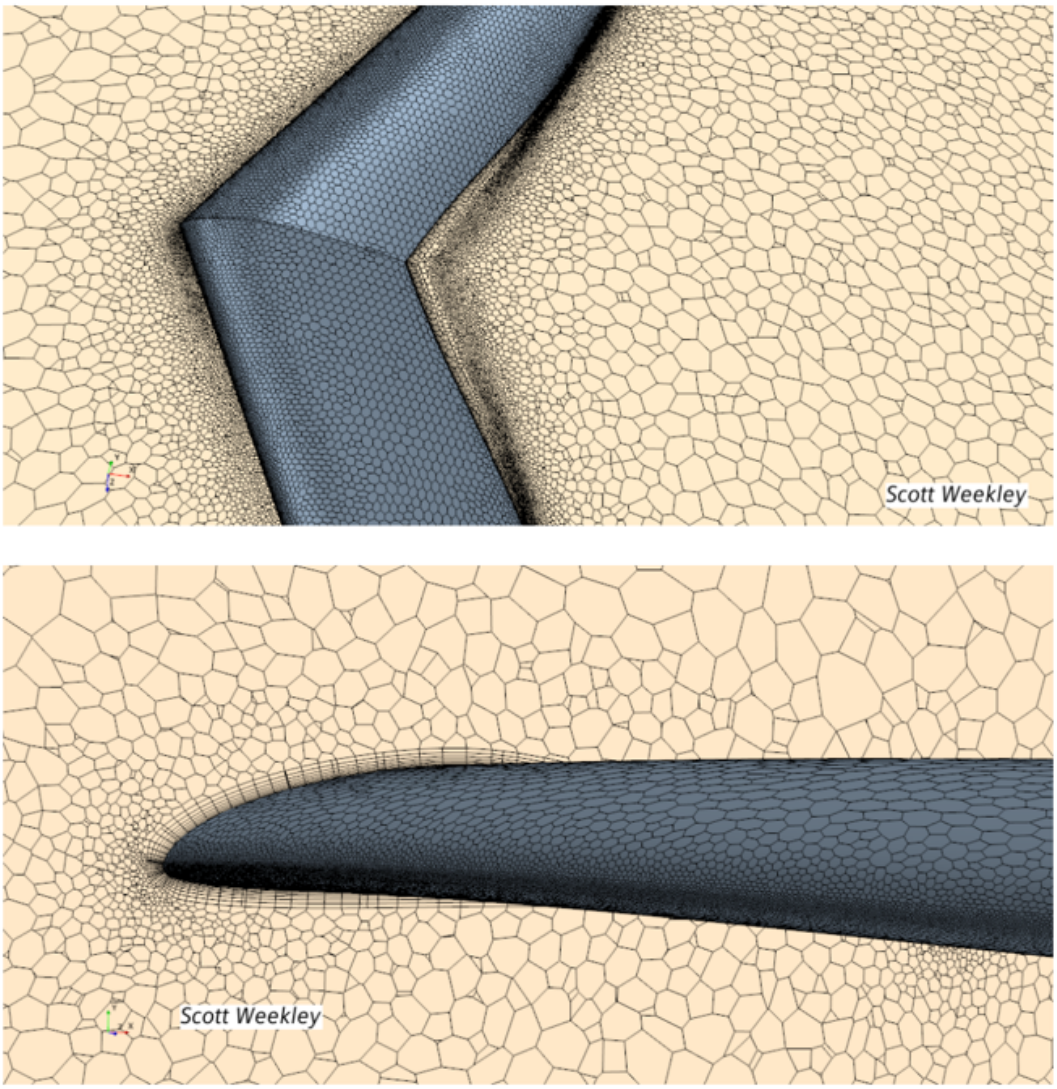

Figure 19: Final Mesh for Bellwether in STAR-CCM+: Overall (top) and Prism Layers (bottom)

2.2 Literature Review: Summary

Ludwig Prandtl's lesser known Bell-curve lift distribution, and its potential aerodynamic performance improvements, are incredibly promising. For a hundred years, the elliptical lift distribution has reigned supreme in the aircraft industry, and has been the golden standard for designing efficient aircraft wings. But as of recent, the potential benefits of adopting the bell-curve distribution have been explored. Most notably is the work of Dr. Bowers at NASA with the development of the Prandtl-D, a 12.3 ft flying wing capable of low induced drag flight and the creation of proverse yaw. This work inspired the creation of Bellwether by Scott Weekley, a 26ft flying wing that worked to improve on Dr. Bower's design and looked at a case study of several different lift distributions. The Prandtl-D was also referenced by

Kyle Lukacovic in a parametric study detailing the optimal position for multiple flying wings to fly in formation, and both new theses tied bell-curve lift distributions to avian flight and utilized CFD as a main analysis tool. Building off of proverse yaw and the Prandtl-D, Hainline and Richter from Washington University developed an unswept flying wing, capable of benefiting from the aerodynamic performance improvement and creation of optimal proverse yaw for coordinated turns. All of these sources will contribute to the creation of Monarch, a conventional tube-and-wing aircraft with a bell-curve span loading, in one way or another. In conclusion:

1. The bell curve lift distribution constrains root bending moment over wingspan, and by optimizing downwash and wing inertia, leads to an 11 % decrease in induced drag for a 22 % increase in wingspan, according to Prandtl. A similar performance increase was explored by Jones in 1950.

2. The Prandtl-D successfully demonstrated a reduction in induced drag through implementation of a bell curve lift distribution, while creating proverse yaw in a coordinated turn, alleviating the need for vertical stabilizers. Missing from Dr. Bower's work, is the lack of connection between flying wings and conventional aircraft for the application of the BCLD. The lack of fuselage and stabilizers leads to less overall aircraft drag, but trimming the aircraft using elevons for mission payloads can potentially ruin the small drag reductions and lift distribution shape. Bower's did not provide an elliptically loaded aircraft to compare the performance of the Prandtl-D to.

3. Many low-fidelity tools have been successful in analyzing the potential performance benefits of the BCLD, including XFLR5 and Avena Vortex Lattice (AVL), which utilize vortex lattice and lifting line theory methods. These tools have been used by Weekley, Hainline, and Richter successfully in the creation of swept and unswept flying wings, and the results are congruent with the base theory. But similar to Dr. Bowers, there was no substantiation to the benefits of their wing configurations over an elliptically loaded wing of similar geometry.

4. High-fidelity Computational Fluid Dynamics has been an effective tool in accurately predicting aerodynamic performance of BCLD aircraft. Mesh resolution, rough mesh sizing, and RANS solvers will be used in the creation of Monarch, and will be referenced from Weekley and Lukacovic's work. This will be used to validate results of low fidelity analysis found in XFLR5 and AVL.

5. Although ineffective in pitch control, the straight flying wing created by Hainline and Richter has demonstrated a level of control and stability unheard of for that aircraft configuration, by means of advanced control units and morphing wings. Impressive as it is, this aircraft configuration has failed to prove its superiority over conventional aircraft configurations in the areas of mission adaptability, weight, complexity, cost, or side-by-side aerodynamic performance.

Each piece of previous work will uniquely contribute to the creation of Monarch, which aims to answer the question: can a conventional tube-and-wing aircraft configuration, adapted

for a bell-curve lift distribution, provide the same performance benefits seen from Prandtl's work, but unlike previous researchers, be designed to be easy to analyze and simple to implement on existing air frames?

CHAPTER III

DESIGN THEORY

3.1 Wing Design Theory

The following theory used for redesigning the wing for the Volantex ASW28 will focus on inviscid, incompressible flow theory from John Anderson's Fundamentals of Aerodynamics. Due to the average chord length, flight velocity, and air characteristics, the maximum Reynolds number experienced by this aircraft in flight is on the order of magnitude of 125,000, with cruise flight closer to 90,000. For the purpose of analyzing the airfoil and wing's aerodynamic behavior, the flow will be considered inviscid and incompressible. Because the new wing has the potential to be twisted aggressively, the stall characteristics of airfoils selected for the root will have to be analyzed.

The redesign for the Volantex ASW28 wing, renamed Monarch, will look at simple low-fidelity analysis techniques, substantiated by high-fidelity CFD, aimed at reducing induced drag and increasing flight performance over an equivalent elliptical configuration. The design of Monarch will be based in Lifting Line theory due to its unswept wings, and the wing will be iterated on until a design is achieved that demonstrates a near-11 % reduction in induced drag. It is important to first review the theory that will act as the building blocks for Monarch's design. These will be detailed in the following work.

3.1.1 Drag in 2-Dimensions

Fundamentally, there exists two different components of drag when considering incompressible flow: viscous (profile) drag and induced drag [2]. Viscous drag, or profile drag, is the sum of skin friction drag, D_f, and pressure drag due to flow separation, D_p, and is due entirely to viscous effects. Due to the bulk of the aerodynamic analysis being performed using finite wing methods, such as Prandtl's Lifting Line Theory, viscous drag effects are not being calculated, and will thus be performed later in the design process using high fidelity analysis through computational fluid dynamics in STAR-CCM+. Because the only modifications between the stock Volantex ASW28 and Monarch are slight changes to the wing geometry, it can be safe to assume the skin friction drag and pressure drag due to separation are negligible during level and steady cruise flight, so long as the planform area and airfoil doesn't change, although an airfoil optimization process will be conducted in later work. Separation drag will only be considered near stall, and although it's important to consider, it will not be considered a fundamental drag source in cruise flight. One important design consideration is keeping the planform area the same for Monarch as for the stock wings. If

planform area is held constant, the major increases or decreases in drag will be observed due to induced drag and changes to profile drag in selection of a more optimized airfoil.

3.1.2 Drag in 3-Dimensions: Downwash and Induced Drag

Induced drag is the consequence of a finite wing creating lift. 2 dimensional airfoil analysis, also commonly referred to as infinite wing analysis, assumes that there is no flow along the span of the wing. When considering a finite wing of some span, this assumption cannot be made. Because a finite wing has defined wingtips, there now exists an opportunity for high pressure air on the bottom of the wing to curl around the wingtips towards the low pressure top side of the wing. This net pressure differential creates a span-wise velocity vector towards the wing tips on the bottom, and a span-wise velocity vector towards the root on the top of the wings (*See Fig. 20*).

Figure 20: Wing's trailing vortex, visualized through red smoke

The combination of these opposing span-wise velocity vectors, as well as the curling of high to low pressure air, creates trailing vortices from the wingtips for many existing wing designs. A trailing vortex is a horizontal "tornado", stretching to infinity downstream of the wing, and is proportional to the amount of lift being created, and therefore the magnitude of the wing's pressure differential. The presence of each wingtip's trailing vortex induces a vertical velocity component traveling over the wing's surface, as seen in *Fig. 21*. This vertical velocity component is referred to as downwash, ω, and occurs perpendicular to the

freestream flow. Span-length downwash is characteristic of wings that have conventional lift distributions, such as the elliptical lift distribution.

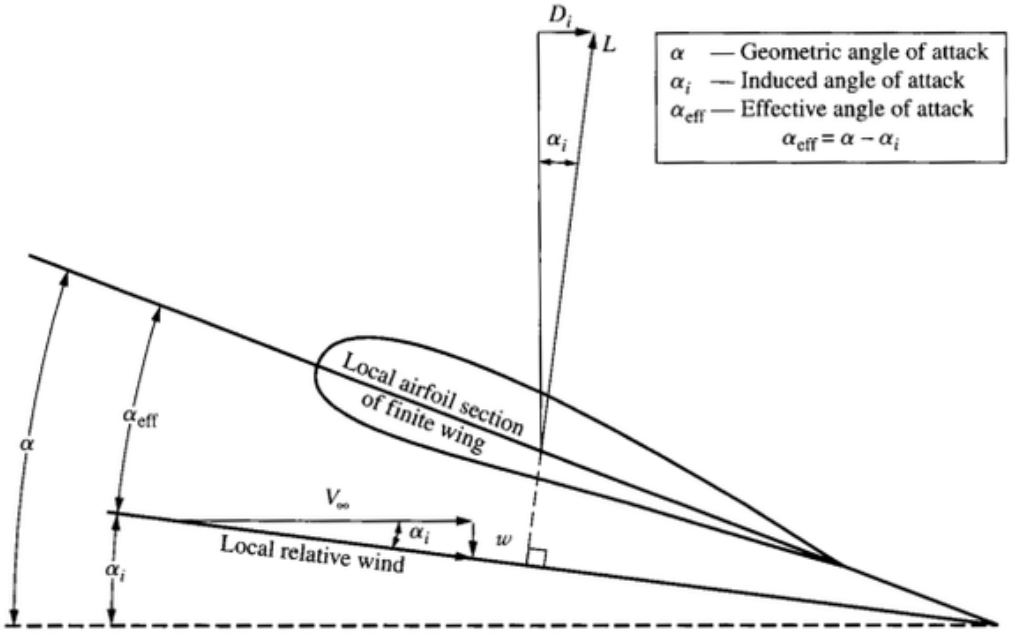

Figure 21: Wing Cross Section, Relationship Between Different α values

When looking at a cross sectional view, the airfoil is now experiencing a freestream velocity and an induced velocity from downwash perpendicular to that of the freestream. The combination of these velocity vectors create an angle of attack that differs from the angle between the chord-line of the airfoil and the freestream velocity, which in 2 dimensional analysis is referred to as the angle of attack. Now, there exists 3 different angle of attack values: induced angle of attack, geometric angle of attack, and effective angle of attack. Geometric angle of attack is the angle between the freestream velocity and the chord line. Induced angle of attack is the angle created when the perpendicular downwash velocity vector is added to the freestream velocity vector, which effectively reduces the angle of attack the airfoil experiences. From this, the angle of attack seen from the airfoil is called the effective angle of attack, denoted as:

$$\alpha_{eff} = \alpha_{GEO} - \alpha_i \tag{3.1.1}$$

Because Lift, a force unique to the wing, is seen perpendicular to the relative wind velocity, it is shown relative to the resultant force of the entire aircraft in the figure above, which is perpendicular to the freestream experienced by the entire aircraft. The force component in the direction of the free stream flow created from the "tilting" of the lift vector by α_i is called induced drag, D_i, and is the third component of drag contributed to an aircraft operating in viscous, incompressible flow. Due to the nature of this thesis defense, and since

the focus is reduction of induced drag, then inherently the process of reducing induced drag involves manipulation of the downwash profile of the wing.

3.1.3 Lifting Line Theory

The approach to analyzing downwash used in the analysis of each iteration of Monarch wing designs involves Prandtl's Lifting Line theory. 2-dimensional aerodynamics shows the presence of circulation, Γ, while lift is being generated by a 2-dimensional airfoil. This can be seen in 3-dimensions through the observation of trailing vortices generated at the wingtips of an aircraft; there is circulation present for a wing traveling in the inviscid, incompressible flow regime proportional to the amount of lift being generated. This relationship comes from the Kutta-Joukowski Theorem:

$$L' = \rho_\infty V_\infty \Gamma_\infty \tag{3.1.2}$$

We also know that circulation, Γ, is the strength of a vortex filament present in a flow, and is proportional to the amount of lift per unit of span divided by freestream air density, ρ_∞ and freestream velocity, V_∞. Ludwig Prandtl's Lifting Line Theory assumes a vortex filament of strength Γ bound to a location in the flow (also known as a bound vortex). Because circulation is present in a flow that is generating a lift force, he assumed the vortex filament was bound to the quarter chord location of a wing, and due to Helmholtz 2nd law of vortex behavior stating that a vortex cannot end in a fluid, the bound vortex creates two trailing vortices at the wingtips in a horseshoe shape (*See Fig. 22*).

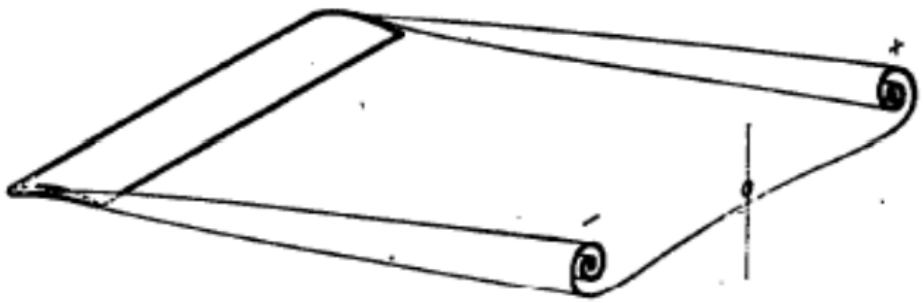

Figure 22: Theoretical Appearance of Wingtip Trailing vortices

Each trailing vortex contributes to the induced velocity component seen at any bound vortex location, y, according to the equation:

$$\omega(y) = -\frac{\Gamma}{4\pi(\frac{b}{2}+y)} - \frac{\Gamma}{4\pi(\frac{b}{2}-y)} = -\frac{\Gamma}{4\pi}\frac{b}{(\frac{b}{2})^2 - y^2} \tag{3.1.3}$$

The left side denotes the effect from the port trailing vortex, and the right side from the starboard trailing vortex. Prandtl saw that the effects of a single bound vortex weren't realistic in analyzing a wing; the downwash seen at each wingtip would be infinite in magnitude. Notice, as y approaches b/2, the bottom of the simplified equation above becomes 0, and the resulting magnitude becomes infinite. Because of this, Prandtl then assumed an infinite number of bound horseshoe vortices to the quarter chord line, each with a strength of $d\Gamma$, and each superimposed on the other. Because of this, the strength of the overall circulation (summation of each $d\Gamma$) grew stronger near the root of the wing. The superimposition of an infinite number of bounded vortices creates a vortex sheet, which in turn induces downwash at each location, y0, along the wing. Lift Distribution, downwash profiles, and trailing vortex sheets can be visualized in *Fig. 23*

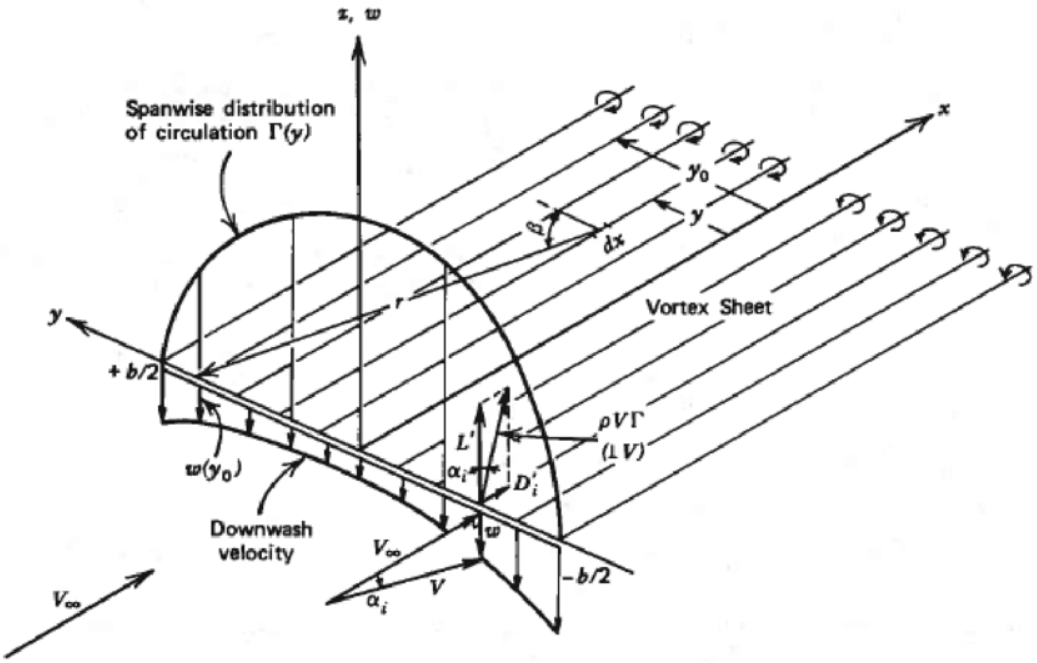

Figure 23: Downwash due to Superimposed Bound Vortices on the Lifting Line, Prandtl

The vertical downwash induced at any location along the lifting line, y0, by the entire trailing vortex sheet, is analyzed using:

$$\omega(y_0) = -\frac{1}{4\pi}\int_{-\frac{b}{2}}^{\frac{b}{2}} \frac{\frac{d\Gamma}{dy}}{y_0 - y}\, dy \tag{3.1.4}$$

The induced angle of attack can also be solved using the downwash distribution and the freestream velocity, with:

$$\alpha_i(y_0) = -\frac{\omega(y_0)}{V_\infty} = -\frac{1}{4V_\infty\pi}\int_{-\frac{b}{2}}^{\frac{b}{2}} \frac{\frac{d\Gamma}{dy}}{y_0 - y}\, dy \tag{3.1.5}$$

Effective angle of attack can be solved for using 2 versions of the sectional (2-Dimensional) lift coefficient equation, one solving for c_l using circulation, Γ, and the lift-slope equation:

$$c_l = 2\pi(\alpha_{eff}(y_0) - \alpha_{L=0}) = \frac{2\Gamma(y_0)}{V_\infty c(y_0)} \tag{3.1.6}$$

$$\hookrightarrow \alpha_{eff} = \frac{\Gamma(y_0)}{\pi V_\infty c(y_0)} + \alpha_{L=0} \tag{3.1.7}$$

Because effective angle of attack is the difference between geometric angle of attack and induced angle of attack, it can be rewritten as Prandtl's Lifting Line Theory:

$$\alpha(y_0) = \frac{\Gamma(y_0)}{\pi V_\infty c(y_0)} + \alpha_{L=0}(y_0) + \frac{1}{4V_\infty \pi} \int_{-\frac{b}{2}}^{\frac{b}{2}} \frac{\frac{d\Gamma}{dy}}{y_0 - y}\, dy \tag{3.1.8}$$

3.1.4 Induced Drag Calculation

Lifting Line Theory will be used as Prandtl intended, but in reverse, to calculate the amount of induced drag being created by the given lift distribution. The idea was that for a given chord distribution, zero-lift α distribution, and total lift being generated, the lift distribution shape could be solved for using Lifting Line Theory to first solve for $\Gamma(y0)$. Instead, the design and analysis of Monarch will be conducted backwards, using the desirable lift distribution shape and determining the geometric angles of attack to obtain it. This process will follow the given steps:

1. Lift Distribution is known from Prandtl's 1933 publication:

$$L' = L'_{y_0=0}[1 - (\frac{y_0}{b/2})^2]^{3/2} \tag{3.1.9}$$

2. From cruise velocity and weight of Volantex ASW28, and assuming both are consistent with Monarch, cruise velocity is solved by assuming a lift coefficient of 0.5, by using:

$$V_{cruise} = \sqrt{\frac{2W}{\rho_\infty C_{L_{stock}} S_{stock}}} \tag{3.1.10}$$

   Cruise velocity was validated with drone footage of the Volantex's maiden flight.

3. From Prandtl's 1933 document, span b is assumed to be 122 % of the stock wingspan (8.33 ft), making the new wingspan of Monarch 10.167 ft.

4. From Monarch wingspan b and weight (3 lbs, from the stock aircraft with batteries and avionics), determine $L'_{y_0=0}$ magnitude so lift distribution L' (1.) integrated over the new wingspan equals the weight of the aircraft.

5. From solved bell-curve lift distribution $L'(y_0)$, solve for Γ_{y_0} distribution using Kutta-Joukowksi Theorem, and resulting $\frac{d\Gamma}{dy}$.

$$\Gamma(y_0) = \frac{L'_{y_0}}{\rho V_\infty} \tag{3.1.11}$$

6. Conduct in-depth airfoil case study of existing sailplane airfoils using XFOIL, and select an airfoil that has a low C_{D_0}, produces the necessary C_L at low angles of attack, and has a large α_{stall}.

7. Determine a chord distribution that achieves a 122 % increase in span, but holds wing area constant (4 sq. ft).

8. From wing geometry, Γ and $\frac{d\Gamma}{dy}$ distributions, cruise velocity, zero-lift α distribution, determine the downwash distribution, $\omega(y_0)$ and inherited $\alpha_i(y_0)$ distribution

9. Using induced angle of attack, α_i, and previously mentioned wing geometry and circulation distributions, determine geometric angle of attack to achieved desired Lift distribution.

10. From induced angle of attack distribution, solve for total amount of induced drag using:

$$D_i = \int_{-\frac{b}{2}}^{\frac{b}{2}} L'(y_0)\alpha_i(y_0)\, dy_0 \tag{3.1.12}$$

11. From total induced drag, derive induced drag coefficient C_{D_i} using:

$$C_{D_i} = \frac{D_i}{q_\infty S} \tag{3.1.13}$$

12. From Solved C_{D_i}, compare the induced drag reduction to the stock Volantex ASW28 wing, which is assumed to have an elliptical lift distribution. If induced drag reduction does not approach 11 % detailed by Prandtl [19], restructure chord distribution and repeat analysis until desired induced drag reduction is achieved.

CHAPTER IV

DESIGN METHODOLOGY

4.1 Design Methodology

The design goal was to decrease the amount of total drag being generated by the Volantex ASW28 stock aircraft (*Fig. 24*) through decreasing the induced drag generated in flight, and to validate the drag reduction through flight testing. To accomplish this, a new wing is to be designed with the bell-curve lift distribution to integrate with the existing fuselage, iterated the design to maximize performance and efficiency, then build and test the new wings against the stock wings on the same aircraft. Constraining the lift and root bending moment aligns with the theory and previous work described above, and allows for simpler manufacturing considerations since the same spar structure used to attach the wings to the fuselage can be utilized by each wing.

Figure 24: Isometric view of the stock Volantex ASW28 air frame

The stock aircraft is composed of a blow-molded plastic fuselage with EPO foam-molded wings and a T-tail. Combined with the fuselage, it has a total wingspan (without winglets) of 8.33 ft and a stock weight of 3 lbs. This includes all built-in components, such as control surfaces and servo attachments, a 2200 mAh LiPo battery, and a FrSky GRX-8 lightweight flight receiver. Several initial flight tests showed two important key factors: first, the estimated cruise speed of the aircraft in steady level flight, which came out to be 36 ft/s via drone footage, and the cheap quality of the control surfaces, which resulted in several ripped aileron hinges and crashes. Both of these will be considered during the manufacturing process of Monarch's wings. Listed in Table 1 are the major characteristic differences between

the stock and modified aircraft, including geometric variables and air frame compositions. The difference in wingspan can be visualized in the CAD mock up of both wings, seen in *Fig. 25.*

Design Attribute	Volantex ASW28 (stock)	Monarch (modified)
Wingspan, b	8.33 ft	10.167 ft
Wing Area, S	3.99 ft^2	3.99 ft^2
Aircraft Weight (No autopilot), W	2.98 lbs (1351g)	3.09 bs (1401g)
Aircraft Weight (GTOW), W	3.53 lbs (1600g)	3.41 bs (1545g)
Airfoil Cross section	ClarkY	MONARCH1 (WASP/sd7032)
Zero-Lift Angle of Attack, $\alpha_{L=0}$	-2.5 deg (-0.0436 rad)	-2 deg (-0.035 rad)
Root Chord, c_{root}	6.5 in	6 in
Tip Chord, c_{tip}	3 in	3.44 in
Wing Composition	Styrofoam	3D Printed LW-PLA
Wing Weight (each)	235 g	260 g
Wing Spars	Steel Square tube (8 mm)	Carbon Fiber Tubes (8.3 mm)

Table 1: Comparison of Aircraft Configurations

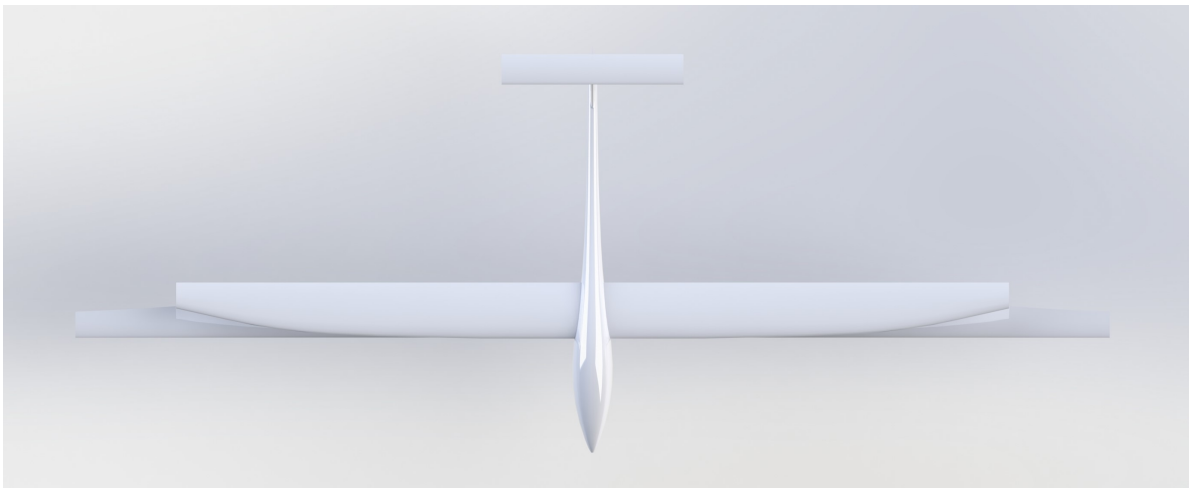

Figure 25: An overlay of the stock wings and the new Monarch wings

Each iteration of Monarch wings during the conceptual design phase will include analysis from both low and high fidelity design tools. These include: MathCad software, XFOIL, XFLR5, AVL (Avena Vortex Lattice), and Computational fluid dynamics in STAR-CCM+, aided by Oklahoma State's supercomputer. Between phases, results from analysis need to 1. match other analysis tools, and 2. demonstrate a performance and efficiency increase, before going onto the next iteration. As previously stated in the introduction, each wing design has several considerations and assumptions that need to be made when tweaking the design variables:

1. Lift being generated by the wings needs to match the weight of the aircraft in cruise. Because the fuselage isn't changing, and assuming the new wing's have a negligible difference in weight compared to the old wings, the amount of lift that both wings generate needs to be 2.98 lbf.

2. The root bending moment generated by each wing needs to be the same, so old wing structural components can be used for each design, and no further structural analysis needs to be conducted. That being said, the root bending moment needs to match that of the stock wings: 2.633 lbf-ft.

3. The stock wings are assumed to have a near-elliptical lift distribution. This means that the Oswald's efficiency factor for the wing set is e=1.

4. Due to the nature of both an elliptical (stock) and bell-curve (Monarch) lift distribution, each wing generates different amounts of lift near the root and tip. Because a bell-curve lift distribution generates more lift on the inboard section of the wing, then the lift generated near the root will be greater than or equal to that of the elliptical, which implies either a larger chord or a more aggressive angle of attack. Each increase also increases the amount of profile drag being created, and therefore a balance needs to be made.

5. A bell curve lift distribution implies that the loading trails off to 0 lbf/ft at the wingtips, and also implies the slope of $\frac{d\Gamma}{dy_0}$ is zero at the wingtips [4]. Because of this, the airfoil cross section of the wing will either remain constant or will likely vary along the span from a cambered airfoil to a symmetric, low lift one. This will keep the amount of twist minimized near the tip, since the symmetric airfoil will be placed near 0 degrees angle of attack to satisfy this requirement. Both configurations will need to be tested.

6. Elliptically loaded wings that are also elliptical in shape do not have a change in geometric angle of attack, and this is observable from the stock aircraft's wing geometry. Because the new Monarch wing will possibly have variable airfoil cross sections, the wing twist will be drastic from root to tip, on the order of 5 - 10 degrees. Because of this, if a composite approach to manufacturing is selected, non-linear parting boards and molds are to be inherited, which will be difficult to build.

7. Being able to achieve the desired lift distribution shape will either change the taper, the airfoil cross section, or the amount of twist, while other design variables are held constant, as implied by Prandtl's Lifting Line Theory:

$$\alpha(y_0) = \frac{\Gamma(y_0)}{\pi V_\infty c(y_0)} + \alpha_{L=0}(y_0) + \frac{1}{4V_\infty \pi} \int_{-\frac{b}{2}}^{\frac{b}{2}} \frac{\frac{d\Gamma}{dy}}{y_0 - y}\, dy \tag{4.1.1}$$

   As seen by the equation above, because the shape of the lift distribution and therefore the circulation distribution $\Gamma(y_0)$ is constant (see Prandtl's bell-curve equation), as well as flight velocity and span in order to achieve a design Lift and C_l, then the only variables that will change include zero lift angle of attack $\alpha_{L=0}$ (from airfoil data), chord, and geometric angle of attack, $\alpha(y_0)$. Each iteration should focus on the manipulation of these variables.

The following analysis will focus heavily on the optimization of wing configuration to decrease induced drag, but the amount of total drag will also have to be considered for several low-fidelity solvers, high fidelity CFD, and flight testing; it is beyond the scope of this work to perform pressure sensing analysis on a real wing or implement a Trefftz plane into CFD to analyze induced drag for those methods, which measures aerodynamic properties at an infinite length downstream - something that cannot be achieved in CFD with the given computing power [16]. Even though the amount of profile drag being experienced by the aircraft will be higher than induced, the ratio of induced drag to profile drag during cruise flight will be unknown. Therefore, it is important to consider the profile drag while designing the new Monarch wings. This involves an extensive airfoil analysis for the redesign of the wings, which will aim to maintain high $C_{L_{MAX}}$ and $\alpha_{C_{L_{MAX}}}$, while providing a lower local drag coefficient (independent from 3D induced drag), C_{D_0}. By knowing the airfoil drag characteristics and having low fidelity analysis conducted on profile drag and high fidelity analysis of overall drag, the theoretical induced drag can be easily backed out of the aircraft's measured performance.

4.2 Airfoil Theory and Selection

Airfoils are the 2-dimensional building blocks of wing sections, and are responsible for determining most of the aerodynamic performance of an aircraft. Airfoils experience 2 different types of forces: pressure forces (perpendicular to surface) and shear forces (parallel to surface). Combined, these contribute to the lift, drag, and moment created by an airfoil section, and inherently the lift, drag, and moment the wing creates. The estimation of an airfoil's aerodynamic properties was pioneered by Ludwig Prandtl and his colleagues during 1912 and 1918, including the 3-dimension effects on finite wings (namely induced drag), and was published soon after [19]. The content of his work has been the backbone of aerodynamic theory since, and is referenced multiple times throughout this paper.

A new airfoil is being selected for Monarch due to the unknown nature of the aircraft's current airfoil. The stock wings have a flat bottom surface, which implies a Clark-Y airfoil variant, but the thickness is larger than the base Clark-Y geometry and the trailing edge is aggressively filleted, making the specific airfoil unknown and hard to identify. Slicing the wing to determine the airfoil is not an option, since flight testing the wings is needed to provide a baseline for aerodynamic performance. Proceeding with an incredibly obscure airfoil and designing it into the new Monarch wings is irresponsible; therefore, selecting a new airfoil of which the aerodynamic performance is known seems to be the responsible next step. In doing so, an airfoil with desirable stall characteristics will be selected, but most importantly, an airfoil with a low viscous drag coefficient, C_{D_0}, will be needed, as this will increase the ratio of induced drag to profile drag for the wing - the amount of induced drag performance will be easier to measure and observe if it makes up a larger portion of the wing's overall drag profile. When comparing the two wings in future discussion, this will be reiterated, and it is expected that the new wing's drag reduction will be largely contributed to the reduction in profile drag. Therefore, low fidelity analysis will focus greatly on induced drag performance, and initial analysis done with profile drag build-up will be cross-validated

with CFD results to see if the figures match. By validating overall drag reduction across low fidelity analysis, high fidelity CFD, and flight testing, it can be assumed that the induced drag performance solved for initially is accurate.

When selecting a suitable airfoil for the new wing on Monarch, Reynolds number regime and bench-marking were the main tools used. For a cruise lift coefficient, C_L=0.5, the expected cruise velocity of the stock aircraft, Volantex ASW28, is expected to be 36 ft/s. Considering standard day conditions of Stillwater, Oklahoma and the cruise velocity, as well as an average chord of 5.9 inches, the expected cruise Reynolds number is between 80,000 and 120,000. This was computed using:

$$Re = \frac{\rho_\infty V_\infty c_{avg}}{\mu_\infty} \tag{4.2.1}$$

This is considered lower Reynolds number flight, but high enough where major aerodynamic properties seen in performance charts stay relatively the same.

From this, low Reynolds number airfoils and common sailplane airfoils were bench marked and selected [23][24] [1]. These included: e387, k3311, MH30, MH32, MH117, RG15, s3021, sa7035, sd7003, sd7032, sd7037, sd8000, and WASP airfoils.

From the 13 different selections, each airfoil was analyzed using XFOIL software, which allows for iterative airfoil analysis in both inviscid and viscous flow [7]. In XFOIL, viscous flow at a Reynolds number of 80,000 was selected for analysis, and each airfoil was analyzed between -5 and 15 degrees, stepping by 1 degree, and that data was exported into an Excel spreadsheet for ease of comparing the data sets. Viscous analysis is important during this design phase, since stall from flow separation will need to be considered, since the root wing sections will likely have a higher angle of attack. At low Reynolds numbers, flow separation will occur at lower angles of attack, so airfoils selected past this point will nee to perform well in the low Reynolds number regime, and demonstrate higher stall angles, α_{stall} [24]. Flow separating first at the root for bell-curve loaded wings was found to be true from the work of Seung Yoo at NASA Armstrong Flight Research Center under Dr. Bowers, which saw the Prandtl-D stalling near 17 degrees aoa, with main flow separation occurring in the inboard quarter of the span [25]. Data from airfoil analysis included: lift and drag coefficients, moment coefficient, and x locations of flow separation for each angle of attack. Each airfoil's respective performance for each angle of attack was plotted on the same graph, and the down-selection process began.

First to compare was C_L vs. α data. Because the initially estimated geometric angles of attack for the wing root seen in Bellwether [22] ranged between 5 and 10 degrees, peak $C_{L_{max}}$ values and their respective alphas were considered (*See Fig. 26*). Airfoils that had higher $\alpha_{C_{L,MAX}}$ and didn't have flow detachment around 9 degrees angle of attack, aoa, were prioritized and considered for drag analysis. Several airfoils, such as the MH30, sd7037, sd7003, and k3311 had flow separation between 8 and 10 degrees aoa, and were not considered in further steps of airfoil down-select. It is also important to note, the amount of camber is

generally correlated to a higher zero lift angle of attack, $\alpha_{L=0}$, which is an important component when computing the geometric angle of attack, α_{GEO}, withing Lifting Line Theory [24][2]. Because of this, a lower value for this is desirable.

CL Data											
Alpha	E387	MH32	MH117	RG15	s3021	sa7035	sd7032	sd8000	WASP	*sd7032/WASP*	MONARCH1
-5	-0.3269	-0.4008	-0.3995	-0.416	-0.3962	**-0.4017**	**-0.3854**	-0.4267	**-0.3802**	*-0.3828*	-0.3662
-4	-0.1772	-0.3228	-0.3153	-0.3367	-0.3933	**-0.3071**		-0.3409	**-0.3002**		-0.2809
-3	0.0036	-0.2238	-0.2279	-0.2373	-0.1993	**-0.2051**	**-0.1609**	-0.2476	**-0.2085**	*-0.1847*	-0.182
-2	0.1507	-0.1265	-0.0855	-0.1988	-0.0373	**-0.1043**	**0.0198**	-0.1766	**-0.1144**	*-0.0473*	-0.0382
-1	0.2918	-0.0416	0.0673	-0.078	0.1502	**-0.003**	**0.1808**	-0.0714	**0.063**	*0.1219*	0.149
0	0.4021	0.1109	0.2247	0.0056	0.305	**0.1904**	**0.3258**	0.0126	**0.2688**	*0.2973*	0.3278
1	0.4986	0.2899	0.3806	0.2049	0.4365	**0.3644**	**0.4895**	0.1996	**0.4559**	*0.4727*	0.4736
2	0.5887	0.472	0.5206	0.3883	0.5447	**0.5123**	**0.6242**	0.3962	**0.5781**	*0.60115*	0.6065
3	0.6906	0.5995	0.6225	0.5584	0.6363	**0.634**	**0.737**	0.5488	**0.6881**	*0.71255*	0.7139
4	0.7921	0.7148	0.7355	0.6851	0.7327	**0.7376**	**0.8573**	0.6568	**0.7868**	*0.82205*	0.8164
5	0.8811	0.8194	0.8466	0.7821	0.8341	**0.8388**	**0.9567**	0.7457	**0.8818**	*0.91925*	0.9192
6	0.9849	0.9082	0.9459	0.8656	0.9309	**0.9327**	**1.0585**	0.8319	**0.975**	*1.01675*	1.0126
7	1.1071	0.9843	1.0243	0.9334	1.0082	**1.0211**	**1.1506**	0.9194	**1.0658**	*1.1082*	1.1056
8	1.174	1.0451	1.0896	1.007	1.0764	**1.0963**	**1.2402**	1.0028	**1.1486**	*1.1944*	1.191
9	1.1291	1.1062	1.1623	1.0583	1.0828	**1.1615**	**1.3161**	1.059	**1.2179**	*1.267*	1.2674
10	1.2248	1.1239	1.2203	1.064	1.0923	**1.2089**	**1.3743**	1.0733	**1.2314**	*1.30285*	1.3176
11	1.2232	1.0602	1.2097	0.9916	1.1328	**1.1954**	**1.3849**	0.9836	**1.2397**	*1.3123*	1.3427
12	1.175	0.9643	1.1218	0.9254	1.115	**1.1589**	**1.3695**	0.8774	**1.2519**	*1.3107*	1.3294
13	1.0954	0.9073	1.0001	0.8481	1.0414	**1.0995**	**1.332**	0.8169	**1.2057**	*1.26885*	1.2771
14	0.9735	0.8513	0.8751	0.8293	0.9436	**0.9339**	**1.2726**	0.8576	**1.1129**	*1.19275*	1.1821
15	0.9727	0.8934		0.846	0.8957	**0.8961**	**1.2174**	0.8576	**0.9344**	*1.0759*	0.9602

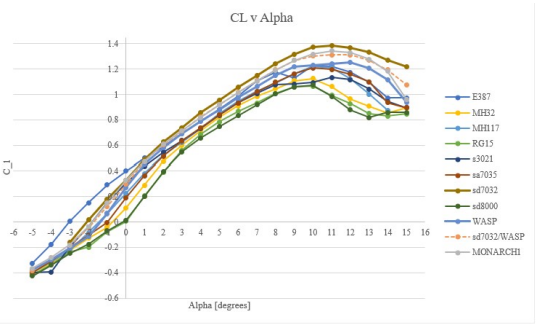

Figure 26: Down-selected airfoils and their respective C_{L_α} curves

Next, C_D was considered. Because this is a 2D analysis of the airfoil cross section and not a 3-dimensional analysis taking into effects of 3-dimensional flow (namely induced drag), profile drag is considered. As stated before, it was initially assumed that profile drag stayed relatively consistent between all iterations of the wing design, so selecting an airfoil with a low C_D over the operational alpha regime was important. It is crucial that the drag coefficient for the selected airfoil is lower than the stock wing's airfoil, the ClarkY, for a majority of the alpha regime it will be operating in (namely, -2 to 8 degrees). Drag coefficient increases drastically at angles associated with the airfoils flow detachment, and these trends are seen in *Fig. 27*. Because of this, the sd8000, MH32, MH117, RG15 airfoils were not selected for further down-select, because they produced a higher C_D at higher alpha values than other airfoils being considered. E387 and k3311 airfoils produced too high of a C_D value over an alpha regime of -2 to 8 degrees. The remaining airfoils (s3021, sa7035, sd7032, and WASP) averaged a C_D=0.02, and were selected for further analysis. Comparitively, the stock wing's ClarkY airfoil shows a C_d = 0.022, meaning the new airfoil will have a 10 % reduction in drag for 2 dimensional flow.

CD Data						
Alpha	s3021	sa7035	sd7032	WASP	*sd7032/WASP*	*MONARCH1*
-5	0.0637	0.05885	**0.07227**	**0.06097**	*0.06662*	0.06263
-4	0.055	0.03348		**0.03533**		0.03769
-3	0.03011	0.0235	**0.03221**	**0.02526**	*0.028735*	0.0291
-2	0.02253	0.01912	**0.02541**	**0.02102**	*0.023215*	0.02185
-1	0.01761	0.01598	**0.02032**	**0.01669**	*0.018505*	0.01801
0	0.01819	0.01792	**0.02119**	**0.01736**	*0.019275*	0.01873
1	0.01869	0.01869	**0.02107**	**0.01673**	*0.0189*	0.01874
2	0.01943	0.01829	**0.0205**	**0.01664**	*0.01857*	0.01815
3	0.0205	0.01751	**0.02019**	**0.01714**	*0.018665*	0.01823
4	0.02127	0.01763	**0.01973**	**0.01838**	*0.019055*	0.01902
5	0.02141	0.0185	**0.02077**	**0.02007**	*0.02042*	0.02039
6	0.02019	0.02015	**0.02239**	**0.02229**	*0.02234*	0.02218
7	0.02022	0.02275	**0.02445**	**0.02498**	*0.024715*	0.02493
8	0.02305	0.02613	**0.02736**	**0.0279**	*0.02763*	0.02774
9	0.0316	0.03266	**0.0301**	**0.02898**	*0.02954*	0.03068
10	0.03955	0.04104	**0.03434**	**0.03385**	*0.034095*	0.03425
11	0.05014	0.05082	**0.03765**	**0.04219**	*0.03992*	0.04252
12	0.06617	0.06299	**0.04455**	**0.05519**	*0.04987*	0.05087
13	0.0882	0.084	**0.05795**	**0.07111**	*0.06453*	0.06765
14	0.12409	0.1499	**0.0791**	**0.09651**	*0.087805*	0.0925
15	0.15909	0.19254	**0.10309**	**0.16013**	*0.13161*	0.1702

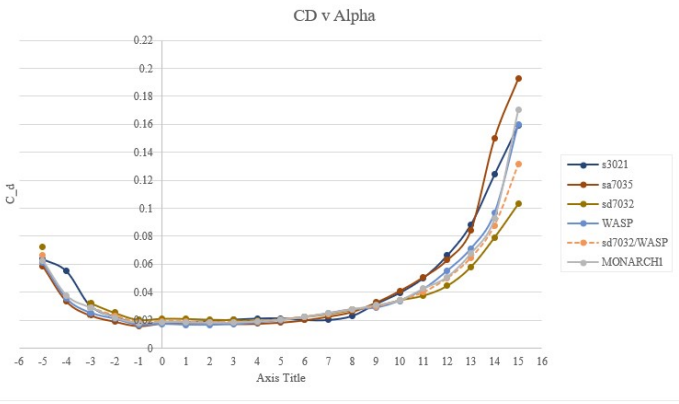

Figure 27: Down-selected airfoils and their respective C_{D_α} curves

Next, the remaining 4 airfoils were analyzed for L/D and C_M performance. The s3021 airfoil was discontinued from the process due to an odd decrease in L/D over an alpha range from 2 to 7 degrees, where it's estimated most of the wing's geometric alpha values will operate. The remaining 3 airfoils averaged a $(L/D)_{max}$ between 44 and 47 between 4 and 8 degrees aoa (*See Fig. 28 and 29*), and all possessed favorable C_{M_α} curves, giving negative values through all angles of attack.

L/D Data					
Alpha	sa7035	sd7032	WASP	*sd7032/WASP*	MONARCH1
-5	-6.825828	-5.33278	-6.235854	*-5.784316776*	*-5.847038161*
-4	-9.17264		-8.497028		*-7.45290528*
-3	-8.72766	-4.995343	-8.254157	*-6.624749915*	*-6.254295533*
-2	-5.455021	0.7792208	-5.442436	*-2.331607498*	*-1.748283753*
-1	-0.187735	8.8976378	3.7747154	*6.336176597*	*8.273181566*
0	10.625	15.375177	15.483871	*15.42952397*	*17.50133476*
1	19.497057	23.232084	27.250448	*25.24126591*	*25.27214514*
2	28.009841	30.44878	34.741587	*32.59518351*	*33.41597796*
3	36.207881	36.503219	40.145858	*38.32453853*	*39.16072408*
4	41.837777	43.451597	42.807399	*43.12949795*	*42.9232387*
5	45.340541	46.061627	43.936223	*44.99892528*	*45.08092202*
6	46.287841	47.275569	43.741588	*45.5085788*	*45.65374211*
7	44.883516	47.059305	42.666133	*44.8627188*	*44.34817489*
8	41.955607	45.328947	41.168459	*43.24870307*	*42.93439077*
9	35.56338	43.724252	42.025535	*42.87489367*	*41.31029987*
10	29.456628	40.020384	36.378139	*38.19926162*	*38.47007299*
11	23.522235	36.783533	29.38374	*33.08363638*	*31.5780809*
12	18.398158	30.740741	22.683457	*26.71209894*	*26.13328091*
13	13.089286	22.985332	16.955421	*19.97037668*	*18.87804878*
14	6.2301534	16.088496	11.531448	*13.80997155*	*12.77945946*
15	4.6540978	11.809099	5.8352589	*8.822178849*	*5.64159812*

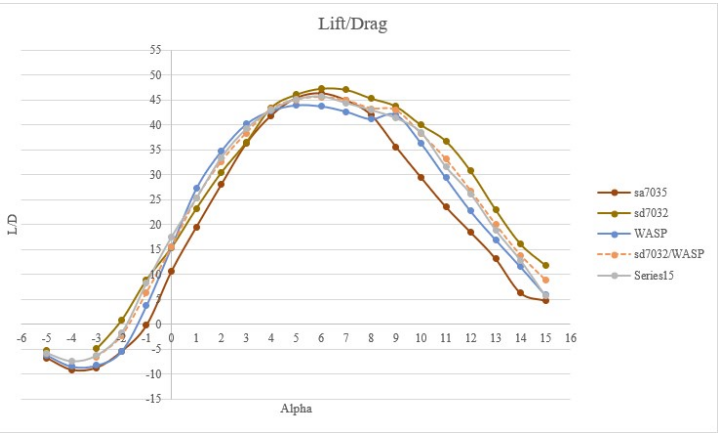

Figure 28: Down-selected airfoils and their respective L/D curves

CM Data					
Alpha	sa7035	sd7032	WASP	*sd7032/WASP*	MONARCH1
-5	-0.0308	-0.0283	-0.0267	*-0.0275*	-0.0329
-4	-0.041		-0.0396		-0.0479
-3	-0.0396	-0.0604	-0.0374	*-0.0489*	-0.0503
-2	-0.0376	-0.0744	-0.0357	*-0.05505*	-0.057
-1	-0.0365	-0.0799	-0.0491	*-0.0645*	-0.0699
0	-0.055	-0.0869	-0.0683	*-0.0776*	-0.0832
1	-0.0672	-0.0947	-0.0806	*-0.08765*	-0.0879
2	-0.0714	-0.0959	-0.0795	*-0.0877*	-0.0881
3	-0.0689	-0.0933	-0.0761	*-0.0847*	-0.0845
4	-0.0641	-0.0911	-0.0716	*-0.08135*	-0.0806
5	-0.0594	-0.0876	-0.0672	*-0.0774*	-0.0771
6	-0.0549	-0.0845	-0.0628	*-0.07365*	-0.073
7	-0.0503	-0.0809	-0.0584	*-0.06965*	-0.0693
8	-0.0446	-0.0772	-0.0531	*-0.06515*	-0.0648
9	-0.0385	-0.0718	-0.0457	*-0.05875*	-0.0592
10	-0.031	-0.0647	-0.0318	*-0.04825*	-0.0505
11	-0.0207	-0.0534	-0.0203	*-0.03685*	-0.0401
12	-0.0163	-0.0447	-0.0126	*-0.02865*	-0.029
13	-0.0228	-0.0427	-0.0088	*-0.02575*	-0.0232
14	-0.0607	-0.0478	-0.019	*-0.0334*	-0.0313
15	-0.083	-0.0579	-0.0586	*-0.05825*	-0.0785

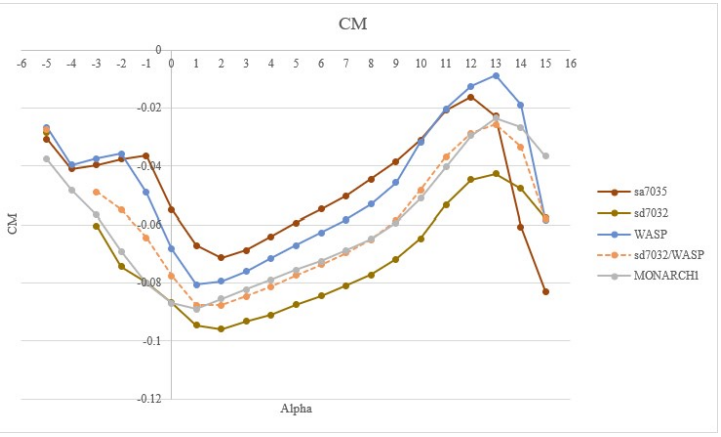

Figure 29: Down-selected airfoils and their respective C_{M_α} curves

From this analysis, the sd7032 airfoil performed the best, with a $C_{L_{max}}$=1.4 at 11 degrees, a $\alpha_{L=0}$=2.3 degrees, C_D values below 0.4 for all alpha values, and the lowest average magnitude for C_M. This airfoil was selected as the initial root airfoil for the first iteration of the wing, Monarch1, because of these values. Although, the WASP airfoil also had desirable performance; it had the lowest C_D value of the final three airfoils, as well as the longest lasting peak for $(L/D)_{max}$. Because each airfoil had favorable traits, a hybrid was created by interpolating and averaging the profiles of both airfoils. This new hybrid, dubbed the MONARCH1 airfoil, was interpolated using XFOIL, exported as a .DAT file to XFOIL, and run at 80,000 and 100,000 Re. The resulting airfoil produced similar C_{L_α} curves, a lower C_D

curve than that of the sd7032, and L/D values between 7 and 15 % higher than the sd7032 for alphas between -1 and 4 degrees. Because of this, the hybrid airfoil, MONARCH1, was taken and selected as the main airfoil for the new Monarch wing. In Figures 7 through 10, the averaged performance data between the sd7032 and WASP airfoils, as well as the new alpha sweep from the MONARCH airfoil, are shown on the graphs. For future wing iterations that impliment a varying airfoil cross section, linearly interpolating the Monarch1 and RAE101 airfoils along the span was done, and those cross sections are shown in *Fig. 30*. This process will be discussed further in following sections.

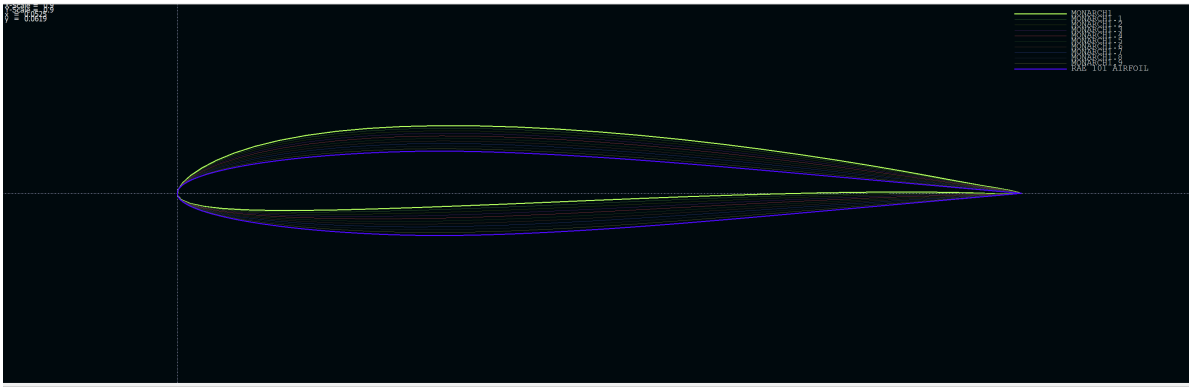

Foil direct design

	Name	Thickness (%)	at (%)	Camber (%)	at (%)	Points	TE Flap (°)	TE XHinge	TE YHinge	Show	Centerline	Style
1	Spline foil	9.04	29.40	0.00	0.00	158	0.00	0.00	0.00			
2	MONARCH1	9.65	26.75	3.32	40.36	61	0.00	0.00	0.00	✕		
3	MONARCH1.1	9.67	26.85	2.99	40.36	61	0.00	0.00	0.00	✕		
4	MONARCH1.2	9.70	27.93	2.65	40.34	61	0.00	0.00	0.00	✕		
5	MONARCH1.3	9.72	28.05	2.32	40.46	61	0.00	0.00	0.00	✕		
6	MONARCH1.4	9.75	27.95	1.99	40.46	61	0.00	0.00	0.00	✕		
7	MONARCH1.5	9.78	31.35	1.66	40.56	61	0.00	0.00	0.00	✕		
8	MONARCH1.6	9.82	31.35	1.33	40.56	61	0.00	0.00	0.00	✕		
9	MONARCH1.7	9.86	31.45	1.00	40.66	61	0.00	0.00	0.00	✕		
10	MONARCH1.8	9.90	31.55	0.67	40.66	61	0.00	0.00	0.00	✕		
11	MONARCH1.9	9.94	31.55	0.34	40.76	61	0.00	0.00	0.00	✕		
12	RAE 101 AIRFOIL	9.99	30.03	0.00	0.00	171	0.00	0.00	0.00	✕		

Figure 30: Linearly Interpolated Airfoil cross sections, including Monarch1 (yellow) and Rae101 (blue)

4.3 Low Fidelity Analysis: Setup

Data from airfoil analysis was taken into low fidelity analysis, which will be discussed in detail in the following work. Low fidelity analysis focused on utilization of several analysis programs: MathCad with a written Lifting Line Theory solver, XFLR5 with both Lifting Line and Vortex Lattice solvers, and AVL, another vortex lattice method analysis tool that uses a similiar Trefftz plane method to solve for aerodynamic performance characteristics. Lifting Line theory analysis results in MathCad will be confirmed in XFLR5, and VLM analysis in XFLR5 will be confirmed in AVL. The results for lift and drag, lift and drag coefficients, moment coefficients, and L/D will be considered when choosing a final iteration of Monarch's wings. Several iterations will be explored and compared to the stock elliptical wing configuration, including: a straight taper wing, and bell-curve chord distribution wing, and a non-tapered, rectangular wing. Each iteration will look at a constant airfoil version

and a varying airfoil version, each using the MONARCH1 airfoil solved for previously, and the varying airfoil will consider a linearly interpolating airfoil from a MONARCH1 at the root to a RAE101 symmetric airfoil at the wingtip. Total, 6 different wing iterations will be analyzed with 4 different solvers, and the most efficient wing design will be chosen for high fidelity CFD analysis in STAR-CCM+ and 3D manufacturing flight testing.

4.3.1 MathCad Setup

MathCad is a hybrid program, combining coding and the ease of written equations to create a program that can be used for a multitude of engineering applications. Unlike coding programs, like Python or Matlab, MathCad doesn't have to be used linearly, and allows for real time equation solving and graphing withing having to run scripts. This tool was selected because of how rapidly variables can be changed for immediate visual and calculated results, although these equations can take a while to solve.

The baseline geometry of the Volantex Aircraft and the new Monarch aircraft were defined early in the programming stage, as well as zero-lift alpha values, $\alpha_{L=0}$, for each of the airfoils (root and tip of both aircraft). Because the major geometric alterations came from chord distribution, this was defined for both the stock and Monarch wing, and this was changed along with zero-lift alpha for analyzing each wing iteration. Important design considerations made for each successive Monarch wing iteration (reiterated from previous sections):

1. Weight is held constant at $W = L$ =3 lbs
2. Monarch Wingspan is held constant at b =10.167 ft, 22 % longer than the stock wingspan, b_{stock} =8.33 ft
3. Design Lift Coefficient is held constant at $C_L = 0.5$
4. Wing Area is held constant at S =4 sq. ft.

Baseline stock wing performance was solved for first, which defined the root bending moment and wing area that Monarch needed to match. This was done by following the following design steps, and was repeated by each wing iteration:

1. Define the amount of lift needed in cruise flight: $W = L$ =2.977 lbs, or 3 lbs for simplicity
2. Define baseline geometry: b_{stock} =8.33 ft, and chord distribution matched an elliptical distribution, so chord was defined as:

$$c_{stock}(y) = \sqrt{1 - \frac{y^2}{(b_{stock,half})^2}} c_{tip} + (c_{root} - c_{tip}) \tag{4.3.1}$$

   This was confirmed to yield a wing area of $S_{stock} = 4ft^2$.

3. Zero-lift alpha distribution was solved for, as an input into the LLT equation later on:

$$\alpha_0(y) = \alpha_{0,root} + |\frac{(\alpha_{0,root} - \alpha_{0,tip})y}{b_{stock,half}}| \tag{4.3.2}$$

4. Cruise Velocity is solved for:

$$V_{cruise} = \sqrt{\frac{2L}{\rho_{Stillwater} C_L S_{stock}}} \tag{4.3.3}$$

5. Lift Distribution was defined, and integrated over the wingspan to confirm it matched the amount of Lift needed (3 lbs)

6. Root Bending moment was solved for by integrating the product of lift distribution and span location. For the baseline geometry, and all Monarch iterations, root bending moment to be matched is $M_{root} = 2.633 lbf ft$

7. Solve for circulation distributions, Γ and $\frac{d\Gamma}{dy}$ using Kutta Joukowski theorem:

$$\Gamma' = \frac{L'}{\rho_{Stillwater} V_{cruise}} \tag{4.3.4}$$

8. Using chord distribution $c(y)$, Circulation distributions $\Gamma'(y)$ and $\frac{d\Gamma'}{dy}(y)$, cruise velocity V_{cruise}, zero-lift alpha distribution $\alpha_0(y)$, effective, geometric, and induced angles of attack can be solved for by using Lifting Line Theory:

$$\alpha(y_0) = \frac{\Gamma(y_0)}{\pi V_\infty c(y_0)} + \alpha_{L=0}(y_0) + \frac{1}{4V_\infty \pi} \int_{-\frac{b}{2}}^{\frac{b}{2}} \frac{\frac{d\Gamma}{dy}}{y_0 - y}\, dy \tag{4.3.5}$$

9. Using airspeed V_{cruise}, wing area $S_{Monarch}$, circulation distribution $\Gamma(y)$ and induced angle of attack α_i, induced drag coefficient is calculated using:

$$C_{D_i} = \frac{2}{V_{cruise} S_{Mon}} \int_{-\frac{b}{2}}^{\frac{b}{2}} \Gamma(y)\alpha_i(y)\, dy \tag{4.3.6}$$

4.3.2 XFLR5 and AVL Setup

To confirm the results found from MathCad, a known and regularly used program was selected. XFLR5 allows for integrated XFOIL analysis and basic aircraft configuration design, and is able to analyze the given geometry using LLT and vortex lattice method solvers, which yields both induced drag and profile drag components for a given wing geometry. To keep the design process simple, the resulting wings analyzed in MathCad were built in XFLR5 in 6 inch semi-span sections, yielding 8 sections for the stock wing and 11 sections for Monarch. Because this body of work focuses on the aerodynamic efficiency improvements of the wing, the fuselage and tail were not considered in any low-fidelity analysis phases.

Each iteration of the wing was constructed using the solved geometric angles of attack for every 6 inch section in MathCad, the iterated chord geometry, and the airfoil cross sections of interest. This setup can be visualized in *Fig. 31.* Each solver used XFOIL data solved for prior, ranging from a Reynolds number of 50,000 to 200,000, which contributed to the profile drag buildup of each wing iteration being analyzed.

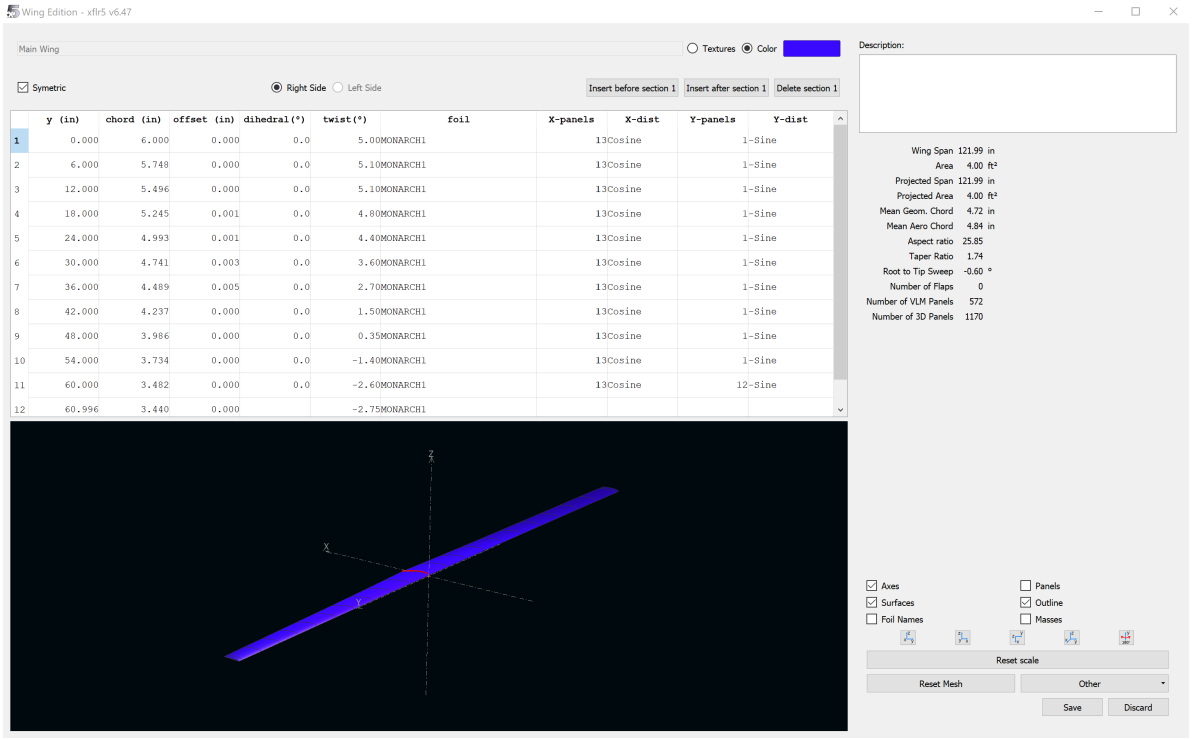

Figure 31: An example of the XFLR5 Geometric Buildup UI

Avena Vortex Lattice is highly compatible with XFLR5. Unlike XFLR5, AVL is strictly a vortex lattice solver, and uses the different sections creating the wing in XFLR5 for panel buildup in the software. Using a Trefftz plane, AVL is able to solve directly for induced drag, as well as compute estimated induced angle of attack along the span, local lift coefficients, and a range of stability derivatives for more in-depth stability and control analysis (*See Fig. 32*). Both programs would be incredibly helpful for alpha and beta sweeps, but because this aircraft configuration is a conventional tube and wing, and not a flying wing like Dr. Bower's or Scott Weekley's aircraft, the beta sweep is unnecessary due to a large amount of stability being contributed from its T-tail setup.

4.4 Computational Fluid Dynamics: Setup

Although this body of work focuses on reduction of induced drag, overall drag reduction of the wing redesign needs to be explored: because the ratio of induced to profile drag is unknown in cruise for this aircraft, and profile drag is expected to be on the order of 4x

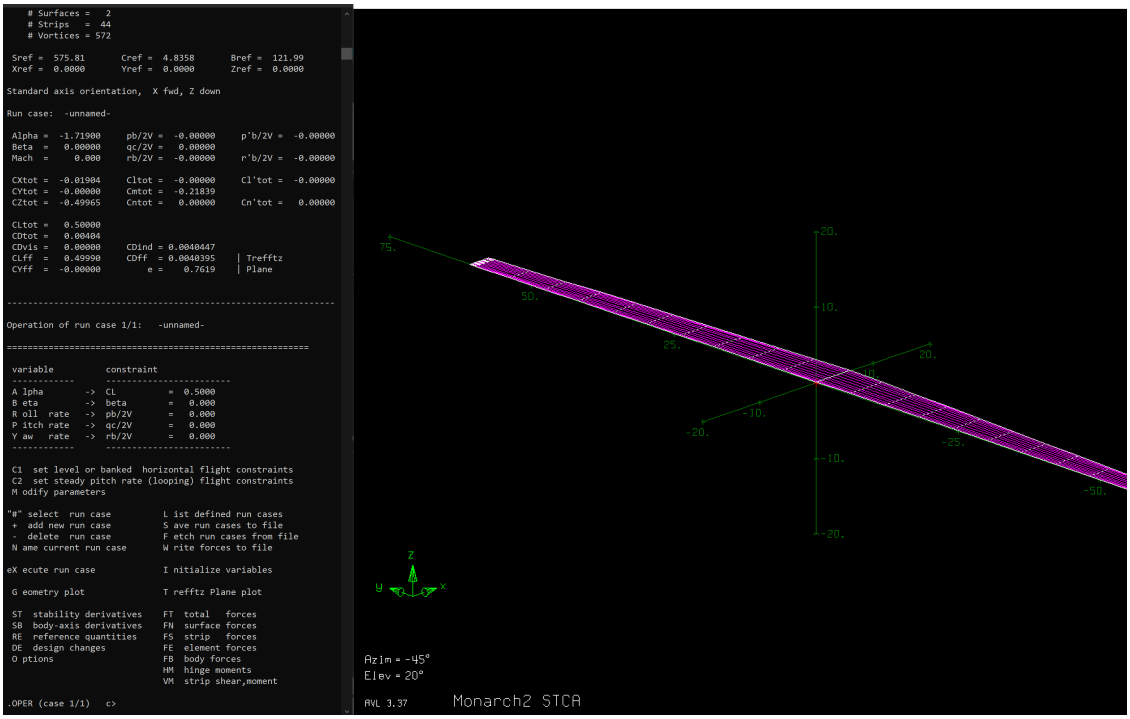

Figure 32: An example of the AVL Wing Panel Buildup UI

the amount of induced, an 11 % reduction in induced drag will only contribute to a near 2 % reduction in overall drag. The airfoil cross section of the Monarch wings is different than that of the stock Volantex wings, so the overall drag needs to be considered with more accuracy and 3D flow effects need to be visualized. Together, CFD will assist in showing a more complete picture of the expected profile and induced drag amounts during cruise flight for the final iteration of Monarch, and this will be compared to the mostly 2 dimensional predictions from low fidelity solvers. To accomplish this, computational fluid dynamics in STAR-CCM+ will focus on accurately predicting the lift and total drag characteristics of the wing.

4.4.1 Initial Setup and Physics Considerations

The final, most efficient iteration of Monarch will be imported into STAR-CCM+ as a parasolid for meshing and solving. Because meshing and running the physics continuum will be assisted by Oklahoa State's High Performance Computer Center's (HPCC's) super computer, Pete, the amount of cells and size of the wings flow domain can be increased substantially over a standard personal computer's capacity to solve. Because of this, a cylindrical flow domain was chosen, with a diameter of 29.5 ft, an upstream distance of 20 ft and a downstream distance of 60 ft. This can be seen in *Fig. 33*.

After defining the flow domain and prescribing an angle of attack for the aircraft, which will assist in completing an alpha-sweep for stall characteristics, each surface was defined as a boundary in the flow simulation. The cylinder walls were defined as a freestream with an

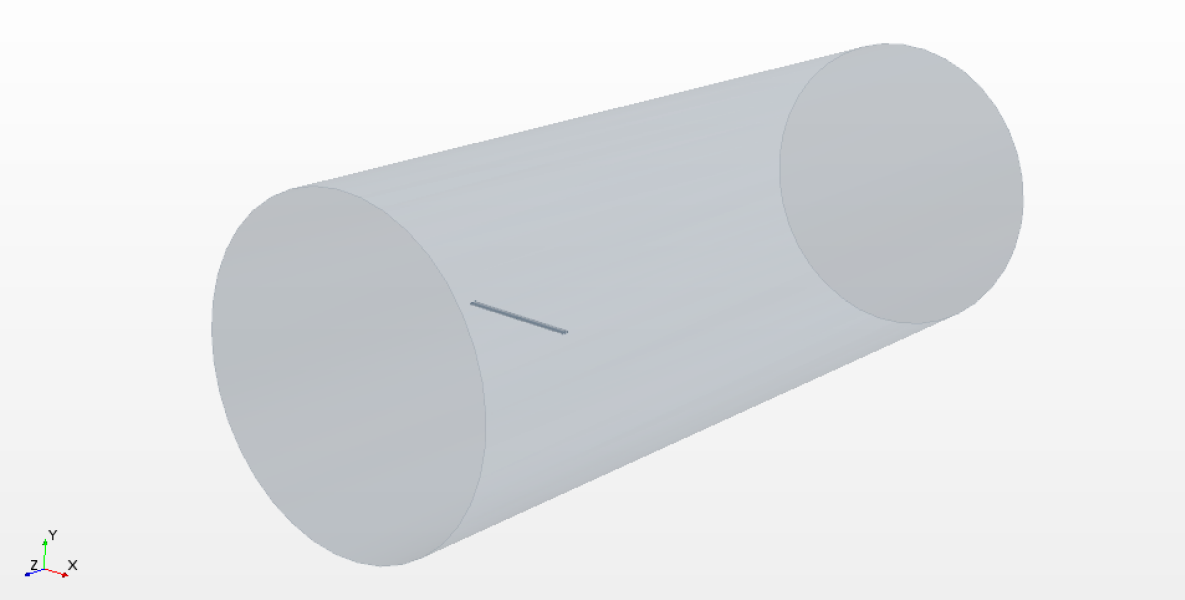

Figure 33: Isometric View of the Flow Domain in STAR-CCM+

initial Mach number of 0.032, consistent with a flight velocity of 36 ft/s at 1000 ft altitude, the inlet defined as a velocity inlet with an initial flow velocity of 36 ft/s, and the outlet as a pressure outlet.

From this, a physics continuum was added to properly simulate airflow over the wing surface. Unlike Weekley and similar to Lukacovic, a segregated flow solver was selected with RANS (Reynolds-Averaged Navier Stokes) to analyze the flow, since pressure and velocity were of interest over flow energy, and consideration was made for minimizing the amount of computing time. A final consideration was treating air as a steady, ideal gas due to its extremely low Mach number. A detailed list of all the physics solvers is included.

STAR-CCM+ Physics Continuum
y+ Wall Treatment
Cell Quality Remediation
Ideal Gas (Air)
K-Omega Turbulence
Reynolds-Averaged Navier-Stokes
Segregated Flow
Segregated Fluid Isothermal
Steady
3-Dimensional Flow
Turbulent Flow
Wall Distance

Table 2: Physics continuum used for STAR-CCM+ analysis of Monarch

Additionally, derived planes were added for future looks at mesh continuity, monitors and plots were added for analyzing force, force coefficients, and moments, and after a flow simulation was added, a force accumulation table was added to analyze the wing's lift and drag distribution. This process was detailed and shown in the work of Weekley and myself [22], and can provide accurate descriptions of force being generated along the span of the wing (*See Fig. 34*). This will be used to compare lift distributions across low and fidelity analysis.

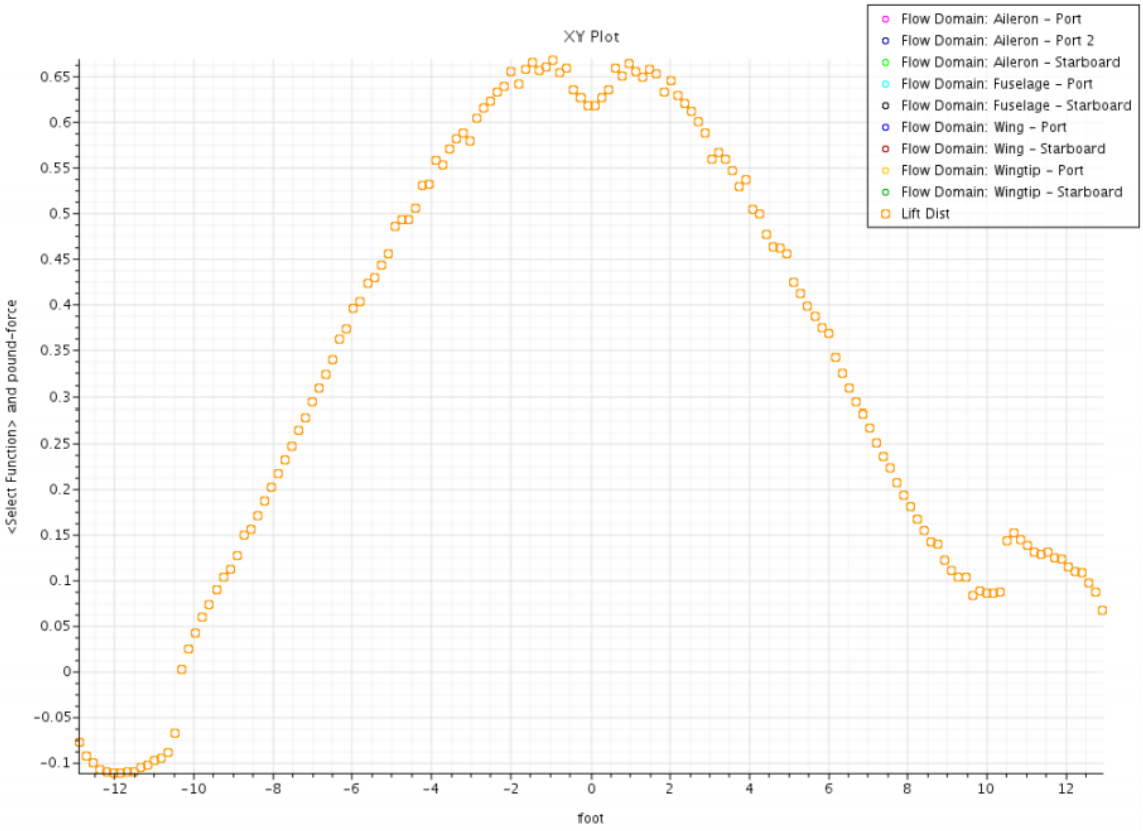

Figure 34: Scott Weekley's analyzed lift distribution of an aircraft with a "modern bell" span loading in roll, in STAR-CCM+

4.4.2 Mesh Independence

Conducting a mesh independence study was crucial for setting up a STAR-CCM+ analysis, since variations in drag from induced drag reductions are small. This implies that the variation in CFD results cannot be dependent on the mesh base size or surface controls. To validate future results, 5 mesh settings with varying base sizes were explored for an iteration of the Monarch wing, and the results were compared to each other for continuity. This mesh used prism layers along the wing surface to capture the flow in the boundary layer, surface controls to refine the mesh size along the wing's leading and trailing edges, and a wake to capture in higher resolution the flow downstream of the wing. Details about mesh settings

can be found in *Table 3* and the final mesh is shown in *Fig. 35*.

Surface	Mesh Control	M2	M3	M4.1	M4.2	M4.3
Default	Base Size	0.75m	0.6m	0.75m	0.75m	0.675m
—	Target Surface Size	0.3m	0.24m	0.3m	0.3m	0.27m
—	Min Surface Size	75mm	60mm	100mm	93.7mm	84.4mm
—	Surface Growth Rate	1.3	1.3	1.45	1.5	1.5
—	Prism Layers	10	10	14	15	15
—	Prism Layers Thickness	8mm	8mm	8mm	8mm	8mm
Leading Edge	Target Surface Size	3mm	2.4mm	3mm	3mm	2.7mm
—	Prism Layers	10	10	14	15	15
—	Prism Layer Thickness	8mm	8mm	8mm	8mm	8mm
—	Min Surface Size	0.75mm	0.6mm	1mm	0.938mm	0.844 mm
Wing Surface	Target Surface Size	5.625mm	4.5mm	9.375mm	7.5mm	6.75mm
—	Prism Layers	10	10	14	15	15
—	Prism Layer Thickness	8mm	8mm	8mm	8mm	8mm
—	Min Surface Size	0.75mm	0.6mm	1mm	0.938mm	0.844 mm
Wake	Wake Distance	7.5m	7.5m	7.5m	7.5m	7.5m
—	Wake Angle	3deg	3deg	5deg	5deg	5deg
—	Wake Size	10 %	10 %	10 %	10 %	10 %
Cell Count	—	12,247,017	21,933,985	4,125,900	4,365,872	10,898,455
—	—	—	—	—	—	—
Monarch	CL	0.57856	0.57900	0.58162	0.582856	0.582241
@ 0deg aoa	CD	0.02526	0.02510	0.02596	0.025967	0.025539
—	L/D	22.9078	23.0686	22.405	22.446	22.798

Table 3: Mesh Independence Study Settings

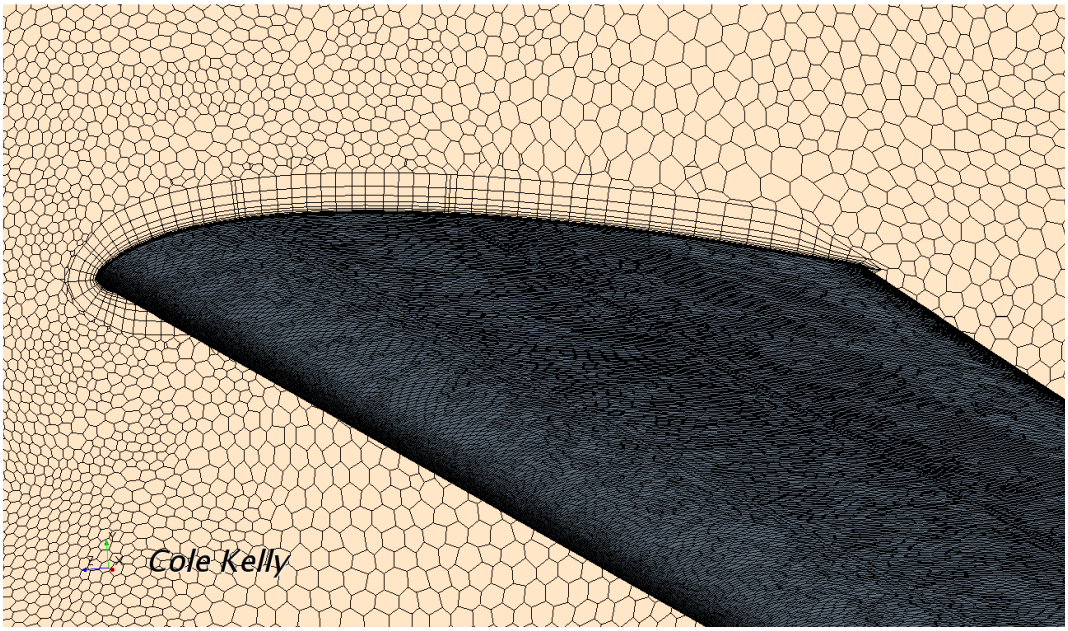

Figure 35: Isometric view of the final surface mesh in STAR-CCM+, showing prism layers

Variation in mesh settings was not uniformly controlled; several meshes demonstrated good base sizes and proportional flow domain sizes while having poor wing surface prism layers, while others improved on different settings and held others constant. For example, M4.1 to M4.2 focused on decreasing minimum cell size on wing surfaces to obtain a smoother leading edge and increasing surface growth rate for uniformity, while holding every other major setting constant from M4.1.

The boundary layer was sized using Equation 4.41, which approximates the boundary layer thickness for a flat plate, and this was calculated for the root chord of 6.5 in and its Reynolds number of 87,000 for cruise flight. This yielded a boundary layer of 6.3mm, so 8mm was

chosen to encompass the entirety of the boundary layer.

$$\delta = \frac{0.37x}{Re^{\frac{1}{5}}} \tag{4.4.1}$$

The measure of how well the mesh's prism layers encompass the boundary layer is referred to as a Wall y+ value. Prism layers are orthogonal cells that border the wing surface boundaries, and vary inversely in thickness the farther away from the body they are. As per Table 2, the final mesh uses 15 prism layers with a total prism layer thickness of 8 mm. When they fully capture the boundary layer of the aircraft, the wall y+ value should reside near 1 for the aircraft surface. Using Mesh 4.3, the wall y+ value ranges from 0.0058 to 0.99 for the entire wing surface, as seen in *Fig. 36*. This guarantees a higher level of accuracy for the results of running the analysis.

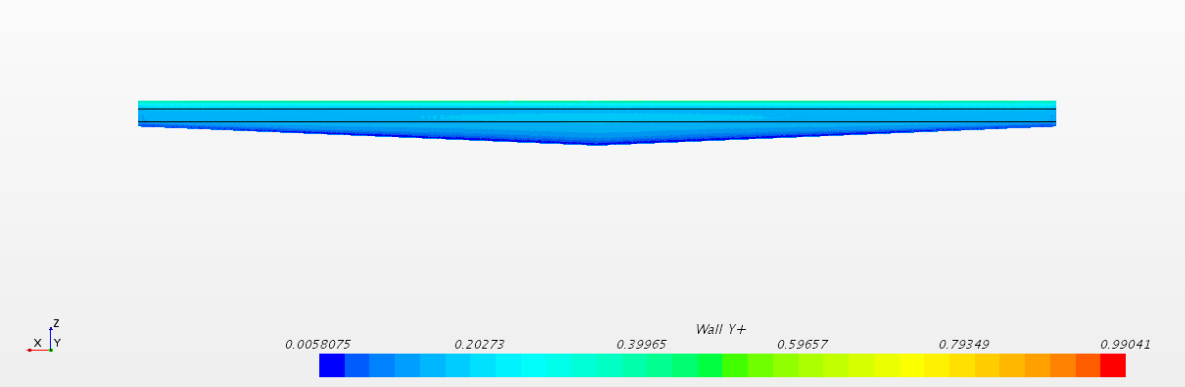

Figure 36: Wall Y+ range for the straight taper Monarch wing iteration in STAR-CCM+

Overall, the surface and prism layer refinement lead to a large variation in overall cell count, but a reduction from 21 million to 4.3 million cells over the course of several mesh iterations was crucial to reducing run time on the super computer, and this was achieved by increasing target and minimum surface sizes to an appropriate level. Each mesh was run on a Bell-curve chord distribution iteration of Monarch, referred to later as BCVA (Bell curve with Varying Airfoil), and analysis was performed for 1200 steps or until coefficient values reached a constant value. The end result, M4.3, used a 10 % reduction in base size and other cell attributes, and achieved a % difference between different coefficient values of 0.11 % for C_L, -1.66 % for C_D, and 1.56 % for L/D. This was preceded by a 0.21 % difference from coefficient values from M4.1 to M4.2, which focused on surface finish for the leading edge. Because of small differences in the analysis results for these mesh settings at different base sizes, the final mesh to be used for analyzing the Monarch wing iterations is M4.3 (settings are included in Table 2).

CHAPTER V

ANALYSIS RESULTS

5.1 Volantex ASW28: Baseline wing geometry and Analysis Results

To conduct a thorough experiment and an accurate comparison between the stock Volantex wings and Monarch's wings, the stock wings need to be analyzed using the same methods as Monarch. This implies modeling the stock wing geometry in MathCad for LLT, XFLR5 into AVL, and in Solidworks to import into STAR-CCM+ for CFD. The airfoil cross section is estimated to be a ClarkY, based off of the wing's characteristic flat underside. Using chord measurements along the semi-span and the measured wingspan, a model was created in Solidworks to determine the wing area that Monarch needs to match, which resulted in 3.99 sq. ft. (rounded up to 4 sq. ft. for simplicity). Also characteristic to the stock wing is a chord distribution that matches an elliptical lift distribution shape, as seen in *Fig. 37*. Due to the stock wings having no geometric twist and a constant airfoil, the stocks wings are assumed to have a perfect elliptical lift distribution (e = 1). This is confirmed in Mathcad, by modeling the chord distribution as elliptical and confirming the wing area solved for in Solidworks.

After defining the needed lift (3 lbs), which resulted from an observed cruise velocity of 36 ft/s and a resulting C_L of 0.5, and a prescribed elliptical lift distribution (as described above), the lift distribution needed to produced 3 lbs of lift came out to:

$$L'_{stock}(y) = 0.455\frac{lbf}{ft}\sqrt{1 - \frac{y^2}{(\frac{b}{2})^2}} \tag{5.1.1}$$

This suggests that the local lift per unit span at the root is 0.455 lbf/ft (*See Fig. 38*). Integration of the lift distribution over each semi-span location yielded a root bending moment of 2.633 lbf*ft for each wing. As previously stated, this number will be checked and matched by the new bell curve lift distribution for each Monarch wing iteration.

Following the previously outlined design steps, $C_L(y)$, $\Gamma(y)$ and $\frac{d\Gamma}{dy}(y)$ distributions are solved for next (*See Fig. 39 and 40*). Lift coefficient distribution was solved for by dividing local lift per unit span by dynamic pressure $q = \frac{1}{2}\rho V^2$ and local chord $c(y)$, and circulation distributions were solved for by Kutta Joukowski theorem and its differentiation.

Using this information, the induced, effective, and geometric angle of attacks were solved for using a reversed Lifting Line Theory. It is important to note, that MathCad is not

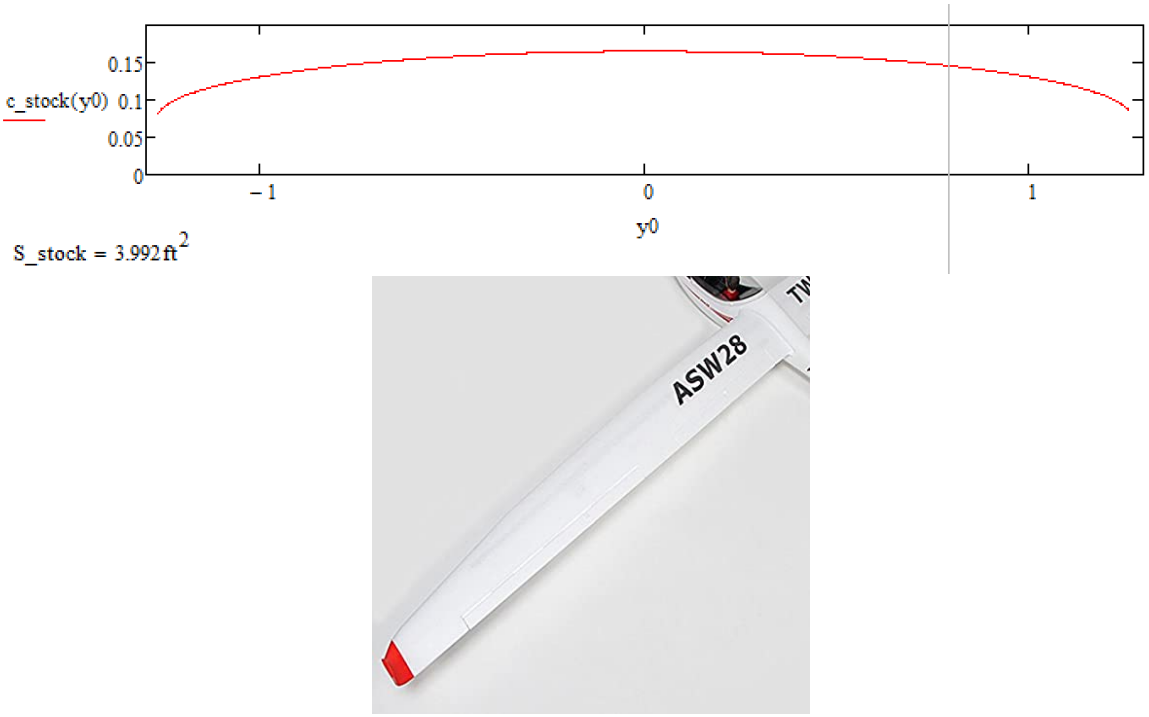

Figure 37: Chord Distribution of the stock wings in MathCad (top) and Real Wing (bottom)

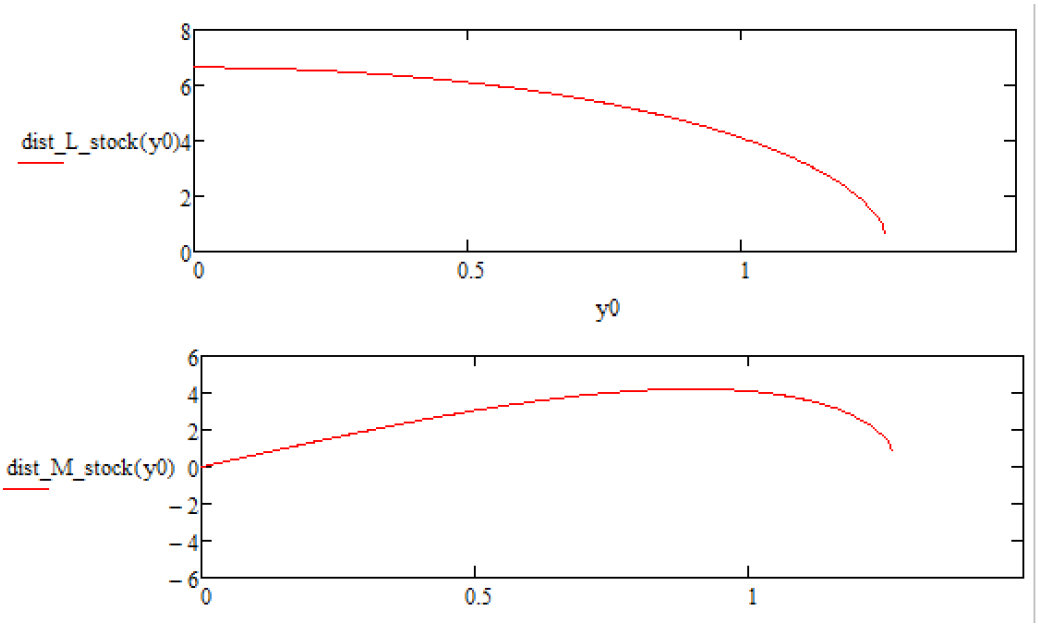

Figure 38: Lift and Moment Distribution for the stock Volantex ASW28 wing (semi-span, in meters)

an intensive solver, and data represented is incomplete. This is believed to be due to two things: characteristic of the elliptical lift distribution is a sharp discontinuity in downwash to upwash at the wingtips, which can be attributed to a sharp pressure differential in this region represented by the slope of the elliptical shape going to $-\infty$ at b = b/2 (see equation

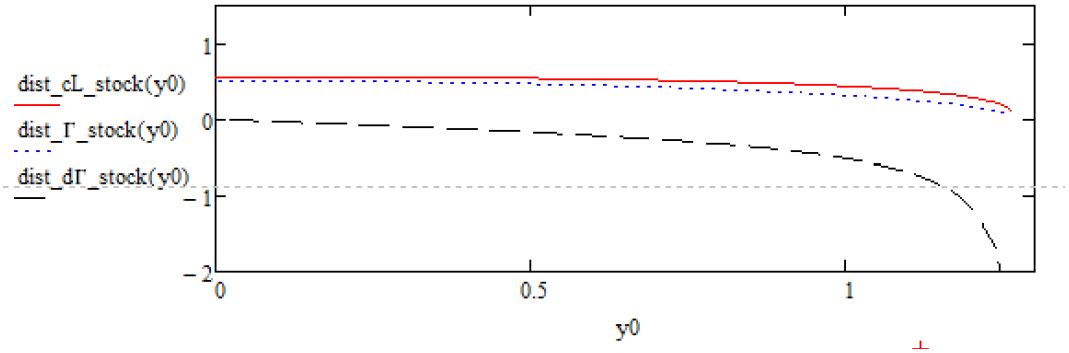

Figure 39: Lift Coefficient, Circulation, and differentiated circulation distributions for the stock Volantex wing

4.4.1), and the way the span distribution is represented, which is in 1/100th foot increments, and how those data points interact with the sharp discontinuity at the wingtips.

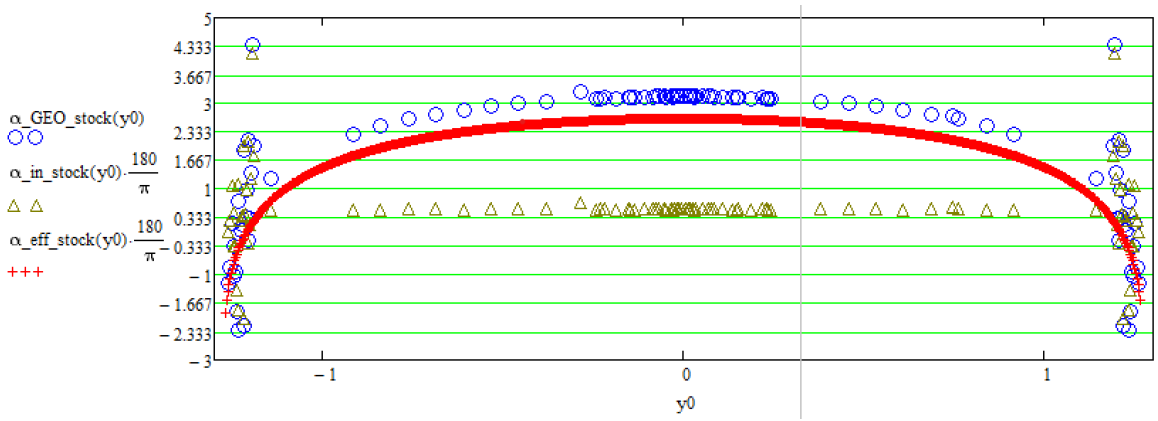

Figure 40: Effective, Induced, and Geometric alpha distributions for the stock Volantex wing (in degrees)

The solved for geometric angle of attack distribution for the original wing is on par with previous expectations. Ranging from 3 degrees to -1, it resembles an elliptical shape as well, and combined with an elliptical chord distribution, it will yield a perfectly elliptical lift distribution, with an Oswald's efficiency factor of e = 1. Important to note, this is not characteristic of the actual Volantex wing, since it was foam-molded with no geometric twist, and relies on its wing shape to yield a near-elliptical span loading. Because the wing isn't exactly elliptical in nature, like the Spitfire mentioned earlier in this work, it is assumed that the actual wing performs slightly less efficiently than an ideal case. For a direct comparison to the elliptical lift distribution, to align with Prandtl's findings, a perfect elliptical span load will be necessary for comparison to the bell curve loading of Monarch. Because of this, it is expected that the Monarch wings will have a higher aerodynamic efficiency than the stock, foam wings that came with the sailplane. As to the degree of this difference, that will be explored in the results from low fidelity analysis.

Because induced angle of attack data was incomplete (*See Fig. 40*), and knowing that the induced angle of attack is constant along an elliptically loaded span, α_i was calculated using theory from Anderson [2]:

$$\alpha_{i,elliptical} = \frac{\Gamma(y=0)}{2b_{stock}V_{cruise}} \tag{5.1.2}$$

Using this induced angle of attack, cruise velocity, wing area, and circulation, the induced drag coefficient was solved for using equation 4.3.6. For the perfect elliptical stock wing (MathCad only), the found induced drag coefficient was:

$$C_{D_{i,stock}} = .004621 \tag{5.1.3}$$

For an elliptical wing, this can also be calculated using:

$$C_{D_{i,elliptical}} = \frac{C_L^2}{\pi eAR} \tag{5.1.4}$$

This figure. will now be the benchmark for comparison for all 6 iterations of the Monarch wing, which will be discussed in further sections. This represents the lowest induced drag coefficient possible for a constrained wing span, and each iteration will aim at improving on this value by a magnitude of 11 %, which is congruent with the theory discussed in Prandtl's 1933 work.

Taking the geometry of the ideal elliptically loaded wing (twisted from Mathcad results) and the stock wing (no twist) into XFLR5, analysis showed expected and standard results for elliptical wings. The stock wings (untwisted) with the CLarkY airfoil performs consistently over the analysis methods with a L/D_i of 109 to 113.6. In contrast, the twisted ideal wing designed with the Mathcad results showed higher L/D ratios, specifically for VLM methods, which seemed to overestimate induced drag coefficient values compared to the designed value in MathCad. LLT drag buildup in XLFR5 yielded a viscous drag coefficient of 0.01697 - 0.01699, showing that induced drag makes up near 22% of total drag in cruise (*See Tables 4 and 5*). These figures will be compared to the following iterations of Monarch in future analyses.

5.2 Monarch Iterations and Results

6 total iterations of Monarch were explored during the low fidelity design phase. As previously stated, each wing iteration uses constant values for wing area $S = 4$ sq. ft., wingspan $b = 10.167$ ft, cruise velocity $V_{cruise} = 36$ ft/s, lift coefficient $C_L = 0.5$, and root bending moment $M_{root} = 2.633$ ft lbf. Each wing also uses the exact same lift distribution shape to

Attribute	XFLR5 LLT	XFLR5 VLM2	AVL
α	1.55	2.00	1.766
C_L	0.5	0.5	0.5
C_{D_i}	0.00459	0.00450	0.0044
D_i	0.0273 lbf	0.0268 lbf	0.0262 lbf
C_{D_P}	0.01697	—	—
D_P	0.101 lbf	—	—
$C_{D,TOTAL}$	0.02156	—	—
D_{TOTAL}	0.128 lbf	—	—
D_i/D_{TOTAL} —	—	20.9%	—
L/D_i	108.94	111.11	113.64

Table 4: Low Fidelity Performance of Stock Wing, untwisted

Attribute	MathCad	XFLR5 LLT	XFLR5 VLM2	AVL
α	0	-0.89	-0.54	-0.80
C_L	0.5	0.5	0.5	0.5
C_{D_i}	0.004621	0.0047	0.00432	0.00423
D_i	0.0275 lbf	0.0280 lbf	0.0257 lbf	0.0252 lbf
C_{D_P}	—	0.01699	—	—
D_P	—	0.1012 lbf	—	—
$C_{D,TOTAL}$	—	0.02169	—	—
D_{TOTAL}	—	0.129 lbf	—	—
D_i/D_{TOTAL}	—	21.6%	—	—
L/D_i	108.21	106.38	115.74	118.2

Table 5: Low Fidelity Performance of Ideal Stock Wing, twisted

match, which follows:

$$L'_{Bellcurve} = 0.509\frac{lbf}{ft}(1-(\frac{y}{b/2})^2)^{\frac{3}{2}} \tag{5.2.1}$$

Similar to the elliptical lift distribution, the local lift per unit span being generated at the root is 0.509 lbf/ft, which creates 3 lbs of lift when integrated along the 10.167 ft span. Following the same design process outlined in 4.3.1, the geometric angle of attack distribution and induced drag coefficient was calculated for each iteration.

Because the only variables able to change are airfoil cross section (which controls $\alpha_{L=0}$ and chord shape $c(y)$, several different wing shapes were explored. The governing equations and resulting wing shapes (semi-span) can be seen in *Fig. 41.* These included:

1. Hershy Bar Wing (MACCA, MACVA, CCCA, or CCVA): No taper, no sweep, with a constant chord length of the Mean Aerodynamic Chord (MAC), 4.764 in.

2. Straight Taper Wing (STCA, STVA): No sweep, with a taper ratio of 0.573 from a root chord of 6 in to a tip chord of 3.44 in

3. Bell-Curve Chord Wing (BCCA, BCVA): A wing with a bell-curve wing shape, with a root chord of 6 in and a tip chord of 3 in.

$$c\_Mon\_BCCA(y0n) := (6in - 3in)\left[1 - \left(\frac{y0n}{bhalf\_new}\right)^2\right]^{\frac{3}{2}} + 3in$$

$$c\_Mon\_STCA(y0n) := -\left|\frac{6in - 3.44in}{bhalf\_new} \cdot y0n\right| + 6in$$

$$c\_Mon\_MACCA(y0n) := 4.764in$$

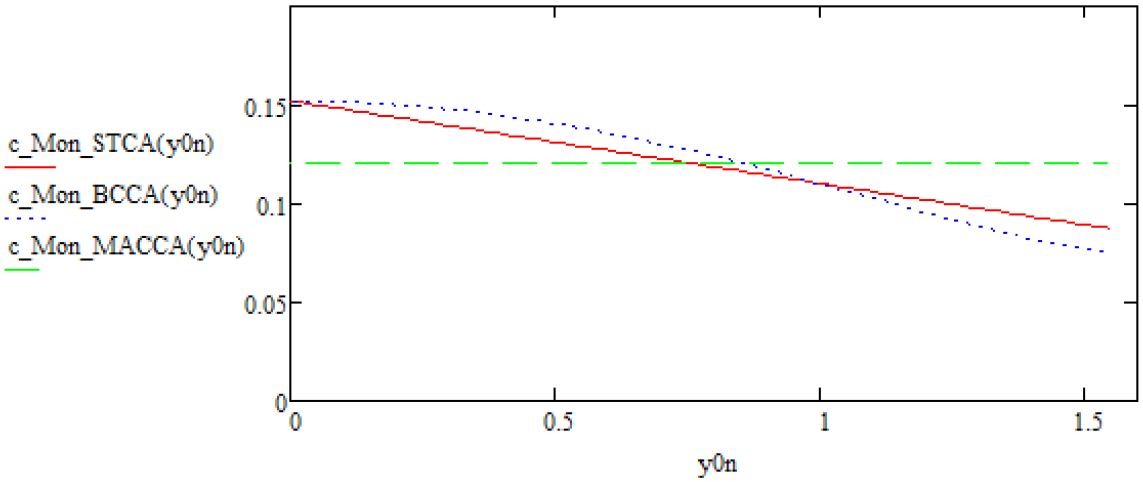

Figure 41: Different governing equations for chord distribution for Monarch wing iterations

Each iteration had two variations: one used a constant airfoil cross section (MONARCH1 airfoil, a hybrid between the sd7032 and WASP) referred to as a -CA (constant airfoil) variant, and a linearly interpolated airfoil cross section starting with a Monarch1 at the wing root and transitioning to a RAE101 symmetric airfoil at the tip, referred to as a -VA (variable airfoil) variant. The motivations for each were simple: Hershy bar and straight taper wings are incredibly popular in existing aircraft, including existing gliders and HALE aircraft (the Global Hawk uses a straight taper wing), and the bell curve shape was explored because like the elliptically shaped stock Volantex wings, the geometric twist is likely to be less aggressive since the planform matches the span load and is expected to produce it naturally. Varying the airfoil from a high-camber Monarch1 cross section to a symmetric RAE101 at the wingtips was also expected to yield a less aggressive wing twist, since the wingtip can be at a neutral angle of attack to produce zero lift. This being the case, less wing twist inherently means greater ease of manufacturing, less emphasis on achieving the desired wing twist profile, and therefore a more consistent design to achieve. Each airfoil

variation and its respective performance is seen in *Fig. 42 and 43*.

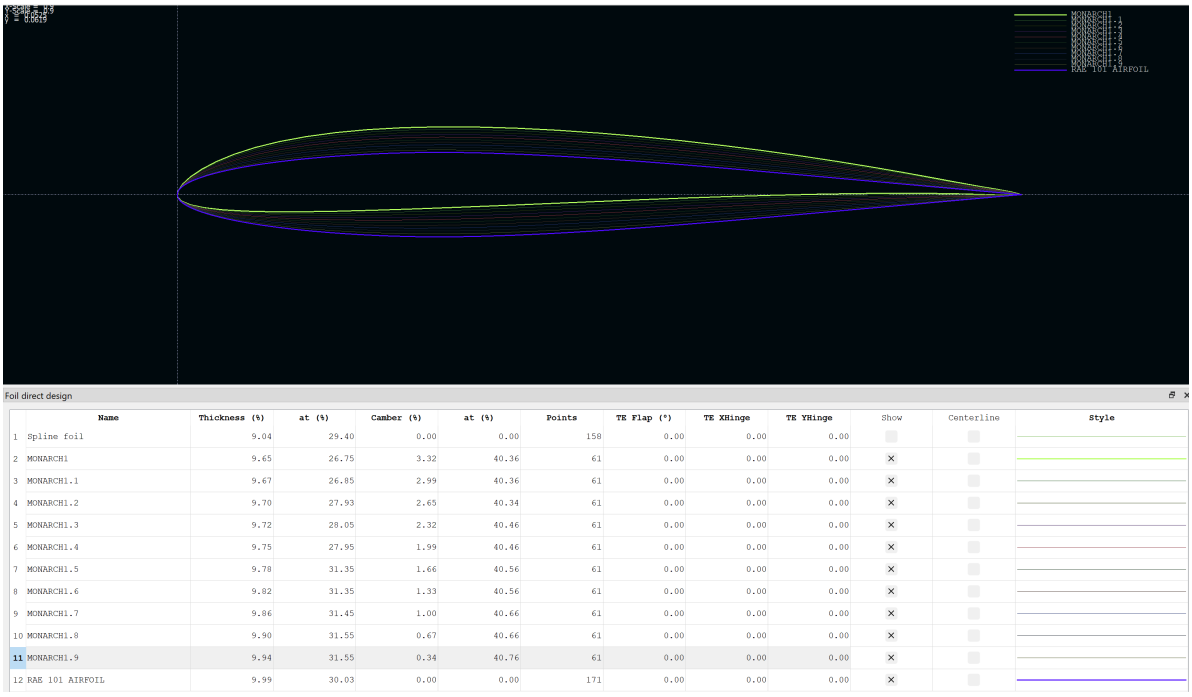

Foil direct design

	Name	Thickness (%)	at (%)	Camber (%)	at (%)	Points	TE Flap (°)	TE XHinge	TE YHinge	Show	Centerline	Style
1	Spline foil	9.04	29.40	0.00	0.00	158	0.00	0.00	0.00			
2	MONARCH1	9.65	26.75	3.32	40.36	61	0.00	0.00	0.00	✕		
3	MONARCH1.1	9.67	26.85	2.99	40.36	61	0.00	0.00	0.00	✕		
4	MONARCH1.2	9.70	27.93	2.65	40.34	61	0.00	0.00	0.00	✕		
5	MONARCH1.3	9.72	28.05	2.32	40.46	61	0.00	0.00	0.00	✕		
6	MONARCH1.4	9.75	27.95	1.99	40.46	61	0.00	0.00	0.00	✕		
7	MONARCH1.5	9.78	31.35	1.66	40.56	61	0.00	0.00	0.00	✕		
8	MONARCH1.6	9.82	31.35	1.33	40.56	61	0.00	0.00	0.00	✕		
9	MONARCH1.7	9.86	31.45	1.00	40.66	61	0.00	0.00	0.00	✕		
10	MONARCH1.8	9.90	31.55	0.67	40.66	61	0.00	0.00	0.00	✕		
11	MONARCH1.9	9.94	31.55	0.34	40.76	61	0.00	0.00	0.00	✕		
12	RAE 101 AIRFOIL	9.99	30.03	0.00	0.00	171	0.00	0.00	0.00	✕		

Figure 42: Linearly Interpolated Airfoil cross sections, including Monarch1 (yellow) and Rae101 (blue)

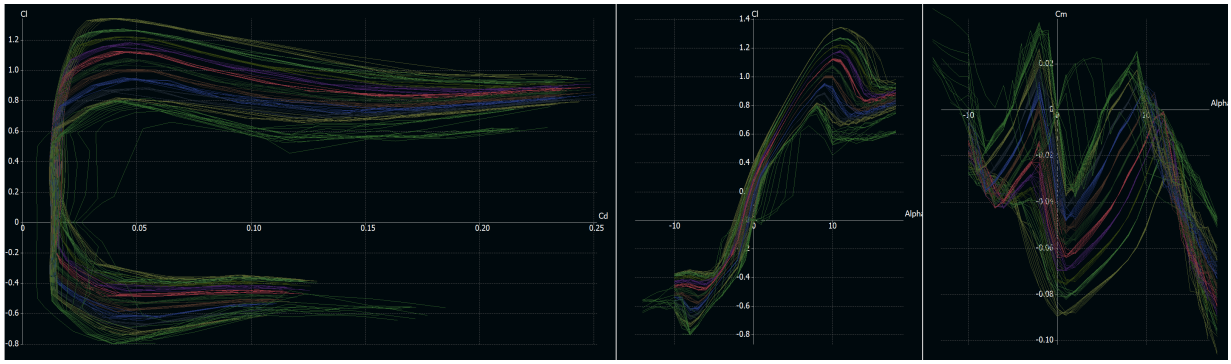

Figure 43: Linearly Interpolated Airfoil cross section variation in C_L vs C_D, C_L vs α, and C_M vs α, from XFOIL analysis

5.2.1 Iteration 1: Hershy Bar Wing (CCCA, CCVA)

The first iteration of interest was a basic wing layout, which consisted of a constant chord along the span of 4.76 inches. Like all other iterations, this yielded a constant wing area and implemented the same lift distribution shape detailed in equation 5.2.1. As previously stated, a constant airfoil and linearly varying variation of this wing were both analyzed in

MathCad, XFLR5, and AVL. The Monarch1 airfoil has a $\alpha_{L=0}$ of -2 degrees (-0.035 rad), and according to previously solved for XFOIL analysis of each airfoil variant (from Monarch1 to RAE101), the $\alpha_{L=0}$ distribution is linear from -2 deg to 0 deg. These considerations were made in the MathCad code, and geometric angle of attack distribution and induced drag coefficient was solved for.

Analysis Results: Mathcad

Shown in *Fig. 44* is the geometric twist profile for the constant airfoil Hershy bar wing, CCCA. Characteristic of this design is constant camber being present along the span, so to achieve zero lift at the wing tips, the amount of washout is near Monarch1's $\alpha_{L=0}$. This value, which is near -2.75 degrees, isn't the same as the $\alpha_{L=0}$ due to the presence of a negative induced angle of attack at the wingtips, which combined with the effective angle of attack (matches Monarch1's $\alpha_{L=0}$) creates a lesser value. This is expected, since the redirection of the force vector past the 70 % semi-span location yields an upwash profile and therefore a negative induced angle of attack.

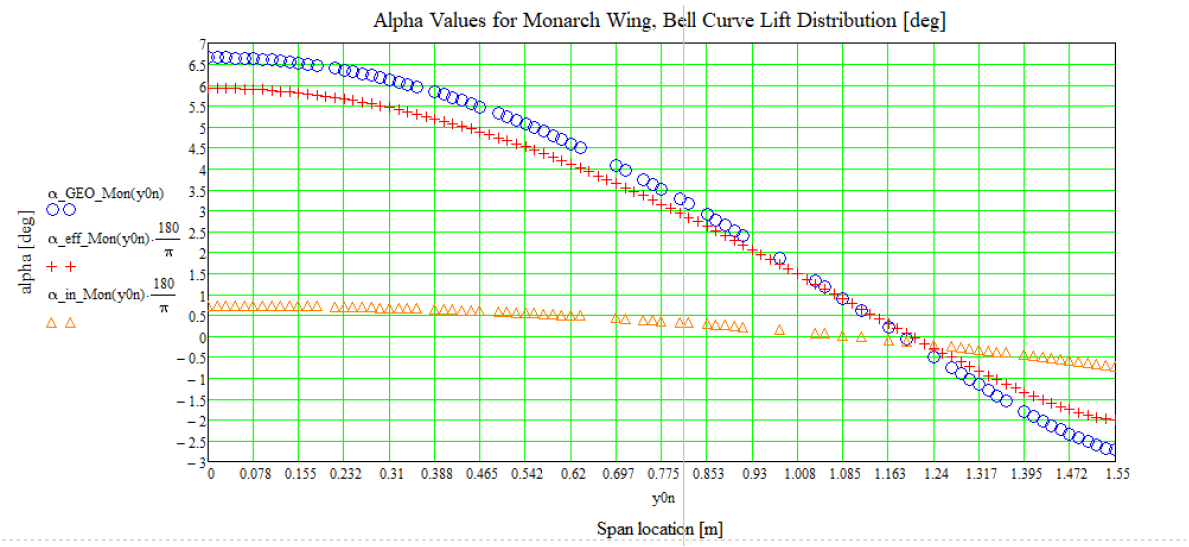

Figure 44: Geometric Twist Profile for CCCA, solved using LLT

For the varying airfoil variation of the Hershy bar wing, the geometric twist is shown in *Fig. 45*. Induced angle of attack distribution is the same for each variation, but since the wingtip airfoil, the RAE101, has a 0 degree $\alpha_{L=0}$, the twist in this region is less drastic. This makes the varying airfoil version of the Monarch iterations desirable, since there is less room for error and more ease for manufacturing. Even though the final Monarch wing will be 3D printed and geometric twist aggression doesn't matter as much, this needs to be a consideration made if a different manufacturing approach is taken in the future. Compared to the 9.5 degree difference between root and tip of the constant airfoil variation, the 7.5 degree difference for this variation is overall less drastic and is expected to have a lower profile drag coefficient (which will be solved for later in AVL and XFLR5).

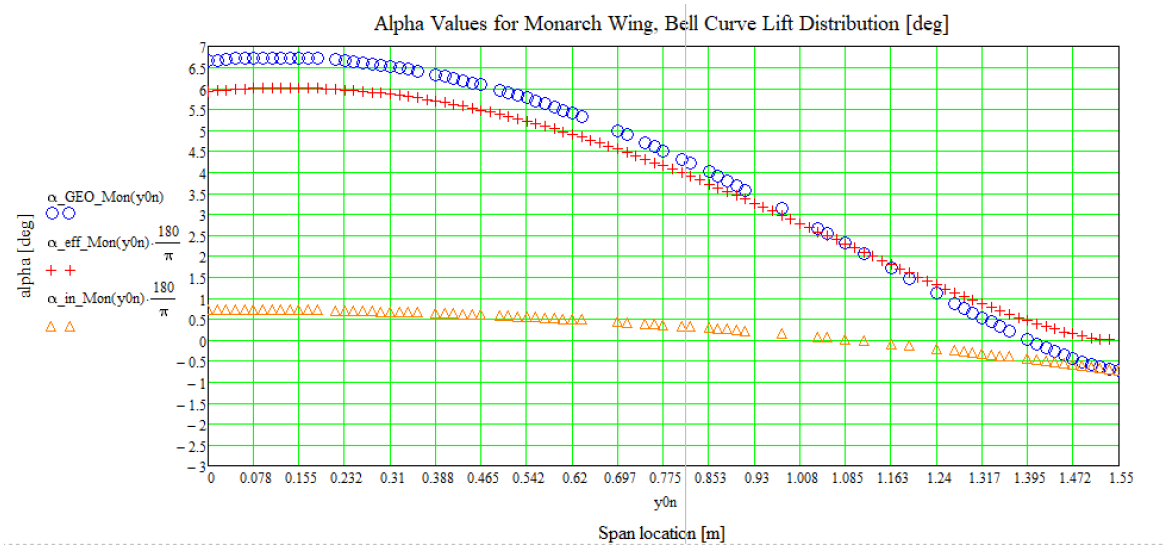

Figure 45: Geometric Twist Profile for CCVA, solved using LLT

For the given lift distribution and resulting induced angle of attack data, which is constant for each variation of the Hershy bar wing, the induced drag coefficient was calculated to be:

$$C_{D_{i,BellCurve}} = 0.004368 \tag{5.2.2}$$

This value is constant for every iteration of Monarch, since the chord distribution only affects effective angle of attack and geometric twist, and induced drag coefficient is only dependent on cruise velocity, wing area, lift distribution shape and induced angle of attack. This value yields a 5.47 % reduction in induced drag, which is considerably less (about half) of the expected induced drag reduction, as stated by Ludwig Prandtl [13]. Modification of design variables while constraining wingspan, wing area, lift and root bending moment did not improve this figure, and this could be a consequence of the Mathcad software being used; only deviations from the listed constraints yielded a larger induced drag reduction. Although less than expected, this number is unique, as none of previous sources considered in previous works look at a comparison between similarly constrained wings with different lift distribution shapes, including Dr. Bower's work. This will be discussed in further detail in the conclusions section of this work.

Analysis Results: XFLR5 and AVL

The geometric twist profile was taken into XFLR5 for the construction of the wing (*See Fig. 46*). Each wing was split into ten 6 inch sections, and a geometric twist was applied at the beginning of each of the sections, and analyzed using XFLR5's built-in Lifting Line and Vortex Lattice solvers at 36 ft/s. With Lifting Line, viscous drag components for each wing

section were included based on the airfoil assigned for each section, as previously solved for in XFOIL, so induced and overall drag coefficient were direct outputs of the solver. Vortex lattice method (VLM2 Inviscid) focuses directly on the lifting effects of bound vortices along the wingspan, and doesn't not include viscous (profile) drag affects.

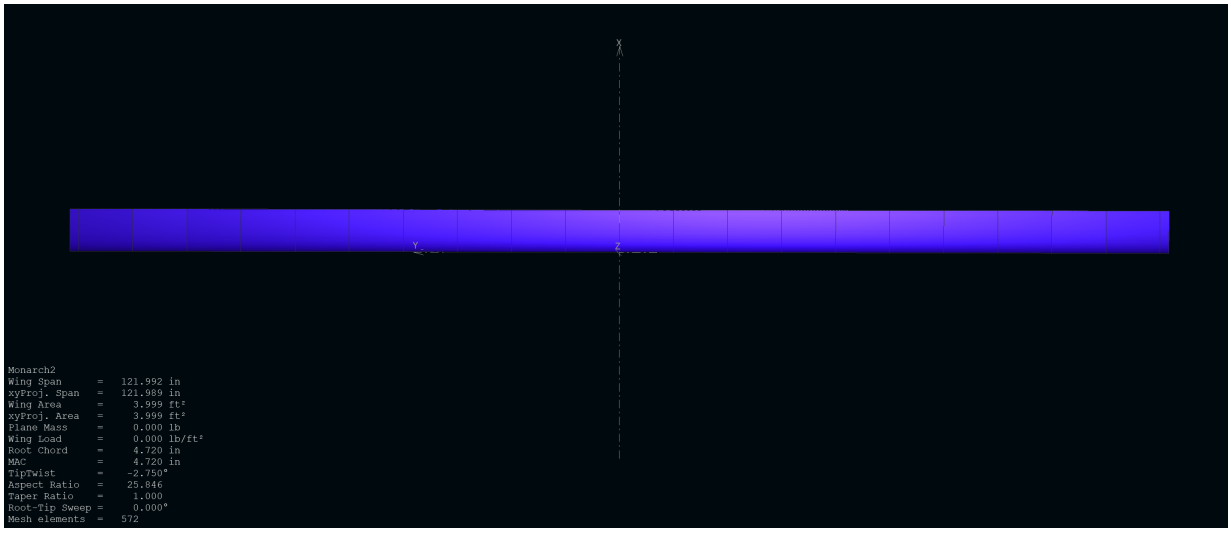

Figure 46: Hershey Bar wing planform, as seen in XFLR5

Both analyses were run from -5 to 15 degrees by 0.5 degree increments. As a result, induced drag, lift distribution, and downwash profiles are shown in the XFLR5 UI (*See Fig. 47 and 48*). One thing not considered while setting up each analysis is the unique angle of attack that each wing will need to achieve a lift coefficient of $C_L = 0.5$. Because the lift distribution and geometric twist profiles in MathCad are perfectly smooth functions, and XFLR5 uses ten linear sections to create each wing, the subtle differences in the geometry yielded slightly altered lift distributions and angle of attack profiles. This consideration will be discussed later in results.

Shown in *Fig. 47 and 48* is the resulting lift distribution and downwash profile for the Hershy bar wing, constant airfoil configuration and varying airfoil configuration using the Lifting Line solver. These wings achieve a lift coefficient of $C_L = 0.5$ at -1.3 and -1.16 degrees angle of attack (aoa). Although this differs from the expected 0 degree aoa in MathCad analysis, the lift distribution demonstrates a bell curve shape and the downwash to upwash transition occurs at the 73 % semi-span location, which is only 2 % different from the expected 70.4 % location detailed in Prandtl's analysis [13] [4] [22]. This is likely due to the reduced attitude of the wing to achieve a lift coefficient of 0.5. Comparing the two lift distributions, the constant airfoil variant demonstrates a smoother bell curve shape and a more consistent upwash profile at the wingtips, two signs that the wing is following the theory outlined by previous works.

Using VLM2, the same wing achieved a lift coefficient of 0.5 at -1.38 degrees. Because AVL uses a similar method to solving for the wing's performance as XFLR5's VLM2 Inviscid

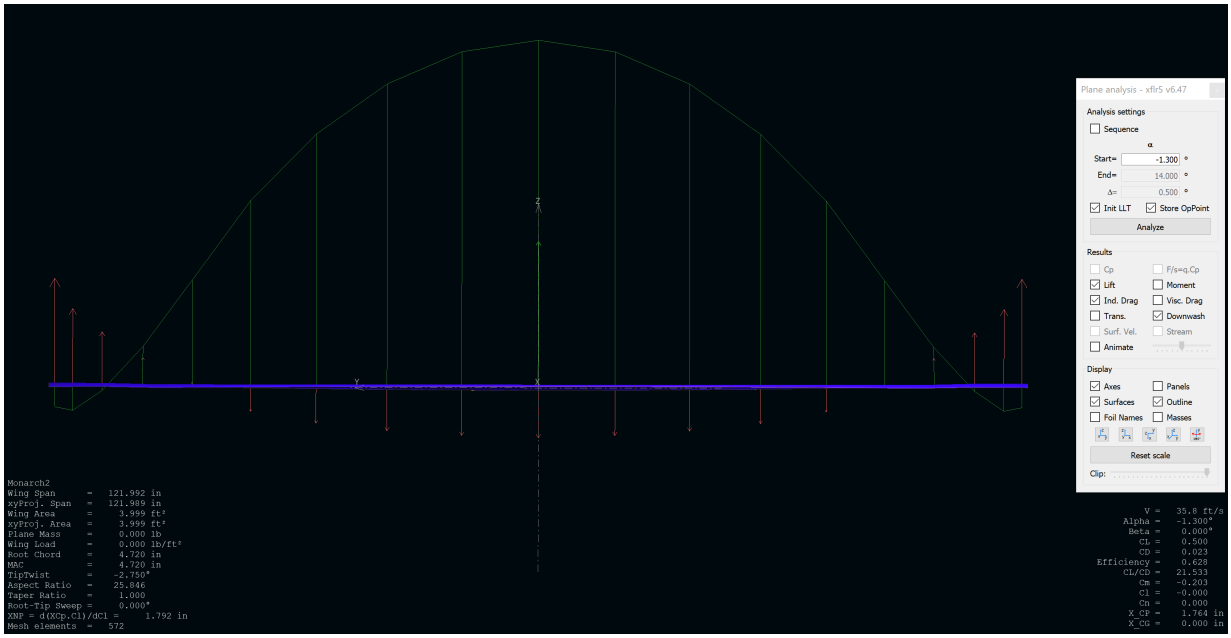

Figure 47: LLT Results in XFLR5 for CCCA

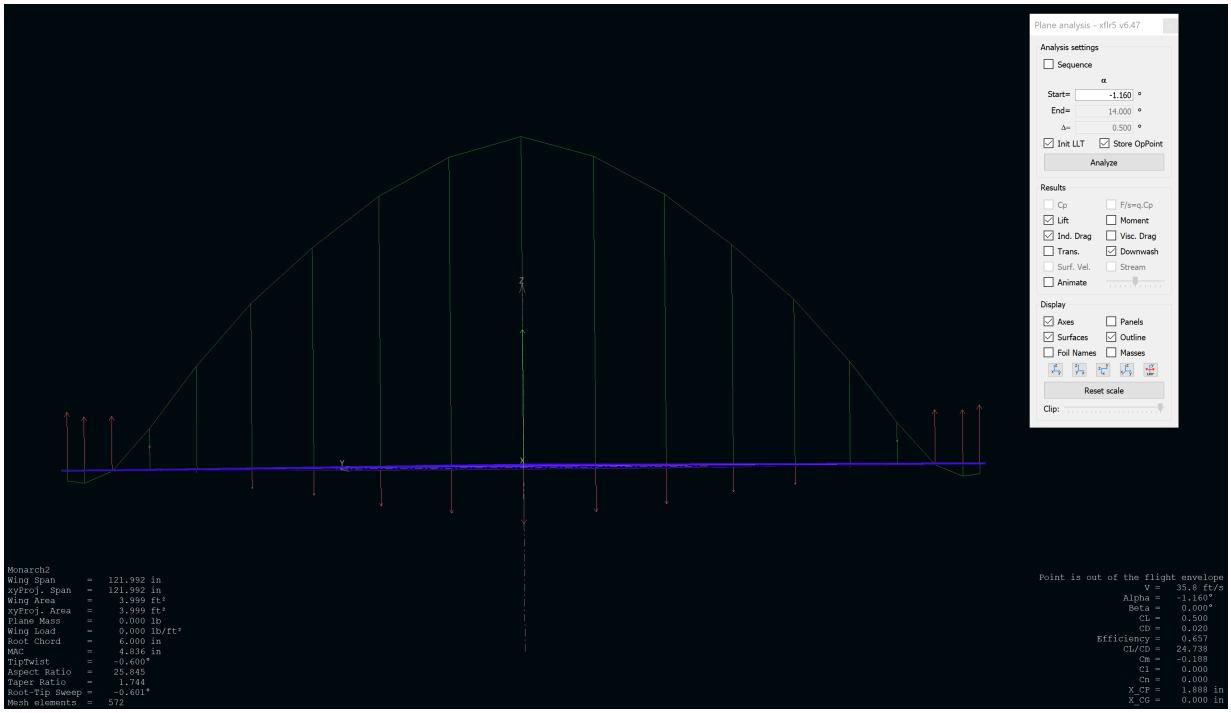

Figure 48: LLT Results in XFLR5 for CCVA

solver, the results are fairly equivalent. With the same wing geometry imported directly into AVL from XFLR5, the wing measured a $C_{D_{i,VL}} = 0.004$ and 0.0041, which puts its inviscid L/D between 122 and 124. All performance values can be seen for the Hershy bar wing configuration in Table 4.

LLT in XFLR5 and Vortex Lattice in XFLR5 and AVL were repeated for the varying airfoil Hershy bar wing, and the performance is recorded in Table 5. Even though each configuration was designed to have the same C_L and C_{D_i} in Mathcad, it yielded a smaller induced drag coefficient (0.0047 vs. 0.0049) with LLT in XFLR5, but a larger induced drag coefficient for Vortex Lattice solvers - 0.0044 and 0.0046 compared to the constant airfoil's 0.0040 and 0.0041. This trend is noticeable for all configurations:

1. LLT solver in XFLR5 usually yields a larger induced drag coefficient value than VLM solvers
2. LLT solver in XFLR5 yields a higher C_{D_i} for constant airfoil wing variants
3. VLM solver in XFLR5 and AVL yields a higher C_{D_i} for varying airfoil wing variants

Attribute	MathCad	XFLR5 LLT	XFLR5 VLM2	AVL
α	0	-1.3	-1.38	-1.75
C_L	0.5	0.5	0.5	0.5
C_{D_i}	0.00437	0.00490	0.00400	0.00408
D_i	0.0260 lbf	0.0292 lbf	0.0238 lbf	0.0243 lbf
C_{D_P}	—	0.01833	—	—
D_P	—	0.109 lbf	—	—
$C_{D,TOTAL}$	—	0.023	—	—
D_{TOTAL}	—	0.137 lbf	—	—
D_i/D_{TOTAL}	—	21.3%	—	—
L/D$_i$	114.469	102.040	124.776	122.540

Table 6: Low Fidelity Performance of Monarch, CCCA

Attribute	MathCad	XFLR5 LLT	XFLR5 VLM2	AVL
α	0	-1.160	-0.76	-0.97
C_L	0.5	0.5	0.5	0.5
C_{D_i}	0.00437	0.00470	0.00444	0.00461
D_i	0.0260 lbf	0.0280 lbf	0.0262 lbf	0.0275 lbf
C_{D_P}	—	0.01553	—	—
D_P	—	0.0925 lbf	—	—
$C_{D,TOTAL}$	—	0.02023	—	—
D_{TOTAL}	—	0.120 lbf	—	—
D_i/D_{TOTAL}	—	23.2%	—	—
L/D$_i$	114.468	106.380	113.080	108.412

Table 7: Low Fidelity Performance of Monarch, CCVA

Overall, for the Hershy bar wing variants, the constant airfoil along the span yielded smaller induced drag coefficients, and therefore larger L/D ratios. Because the geometric twist was more drastic for the constant airfoil variant, its profile drag coefficient is higher.

This was expected, since the geometry lacks simplicity and drag coefficients for local wing sections were expected to increase with twist. This trend can be seen in each iteration of the Monarch wings, which will be described in following sections.

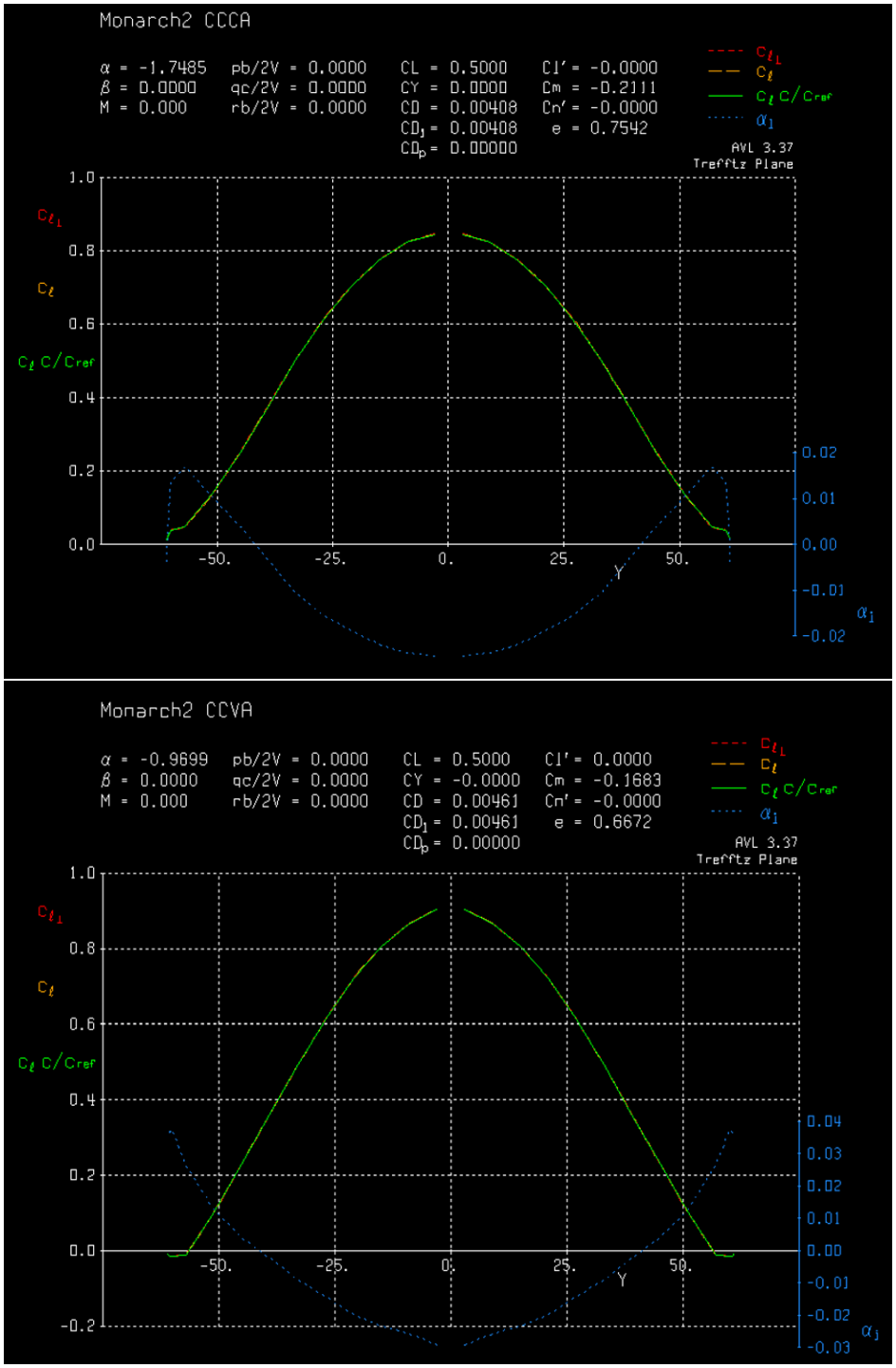

Figure 49: AVL output for CCCA, CCVA showing C_L and cC_L/MAC distributions

Shown in *Fig. 49* is local C_L and cC_L/c_{ref} distributions for each wing, corrected for a

constant lift coefficient of 0.5. This correction, although it changes the lift coefficient loading of each Hershy bar wing variant, is important for considering the operating conditions of the wing, more specifically the upwash conditions and potential stall characteristics of the wing. From this figure, the constant airfoil wing has a wider range of overall angles of attack before stall can occur, as the root is operating at a smaller lift coefficient to create 3 lbs of lift in cruise. Both demonstrate a bell curve lift distribution, as chord is kept constant, but the varying airfoil variant CCVA creates down force at the wingtips during cruise, which is a significant performance loss (see Fig. 43, bottom).

In contrast to the performance increase of the constant airfoil variant, the varying airfoil variant of the Hershy bar wing has a larger area of upwash at the wingtips, and a wider range of induced angles of attack, which would allow for more proverse yaw creation on the wing in a turn. But, because this is not a prioritized design choice due to the amount of yaw control from a vertical tail, the constant airfoil variant is more promising, due to its more desirable stall characteristics and better induced drag performance at operating conditions. This consideration will be observed in following wing iterations.

5.2.2 Iteration 2: Bell-Curve Chord distribution (BCCA, BCVA)

The second and most promising aircraft iteration was the Bell-curve chord distribution wing. This created a wing with a more significantly sized root area, which will hold the most lift, and a skinnier wingtip where lift generation reaches zero. The motivation for this configuration was simple; a larger chord where more lift is generated per unit span should result in a smaller local angle of attack, making the wing less twisted than the Hershy bar or tapered wing. Although this means a smaller wing section at the wingtip to make into an aileron, the geometry is simpler for future manufacturing efforts, if composite layups are needed for larger or different purposed wings.

Analysis Results: Mathcad

The same design steps used for the Hershy bar wing configuration were used to analyze the bell-curve chord wing (BCCA, BCVA) for both constant airfoil and interpolated airfoil variations. As expected, and following the results from the Hershy bar wing, the constant airfoil variant has a larger amount of twist from the root to the tip, regardless of having the same design lift distribution (*See Fig. 50 and 51*). This is also expected to increase profile drag coefficient, but yield lower induced drag coefficients in proceeding analysis at a constant lift coefficient. As with all wing iterations, the calculated induced drag coefficient in MathCad is $C_{D_{i,Mathcad}} = 0.00437$.

The theory held true; root geometric twist for the BCCA and BCVA variants produced the same amount of lift at 5 degrees, compared to 6.5 of the Hershy bar wings. This is due to the chord increasing from 4.76 (CCCA, CCVA) to 6.5 inches, and the reduction in angle of attack for this region means better stall performance, which is a major concern for a wing

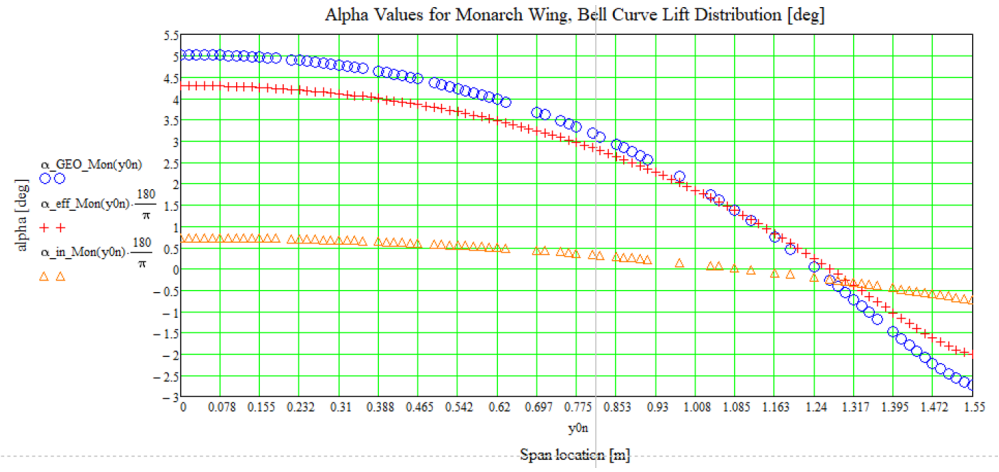

Figure 50: MathCad Geometric Twist, BCCA

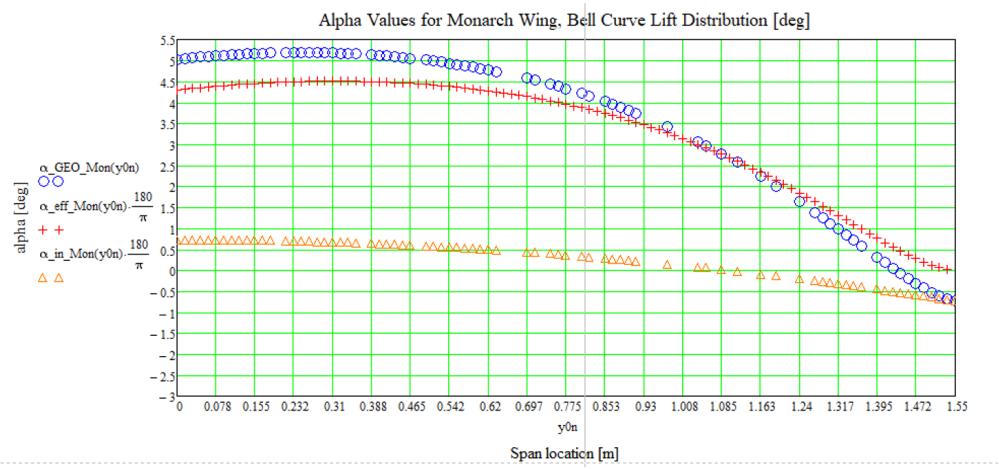

Figure 51: MathCad Geometric Twist, BCVA

with this much twist. At high aircraft angles of attack, the root is expected to stall first: The Hershy bar wing, with a root aoa of 6.5, would stall if the aircraft's overall angle of attack exceeded 5 degrees. The bell curve chord wing variants help increase the stall angle of attack of the vehicle.

Analysis Results: XFLR5 and AVL

Following the same prescriptions, geometric twist values for every 6 inches along the span were designed into each variant of the Bell-curve shaped wing. The same airfoil sections were used from the Hershy bar configuration, as well as the solvers for the given airspeed, with changes being made only to geometric twist and chord length. As for every variant of the wing, wing area was constant. The unique shape of the bell curve chord distribution can be seen in *Fig. 52*.

Running the same VLM2 and LLT analysis as the Hershy bar wing variants, the Bell-

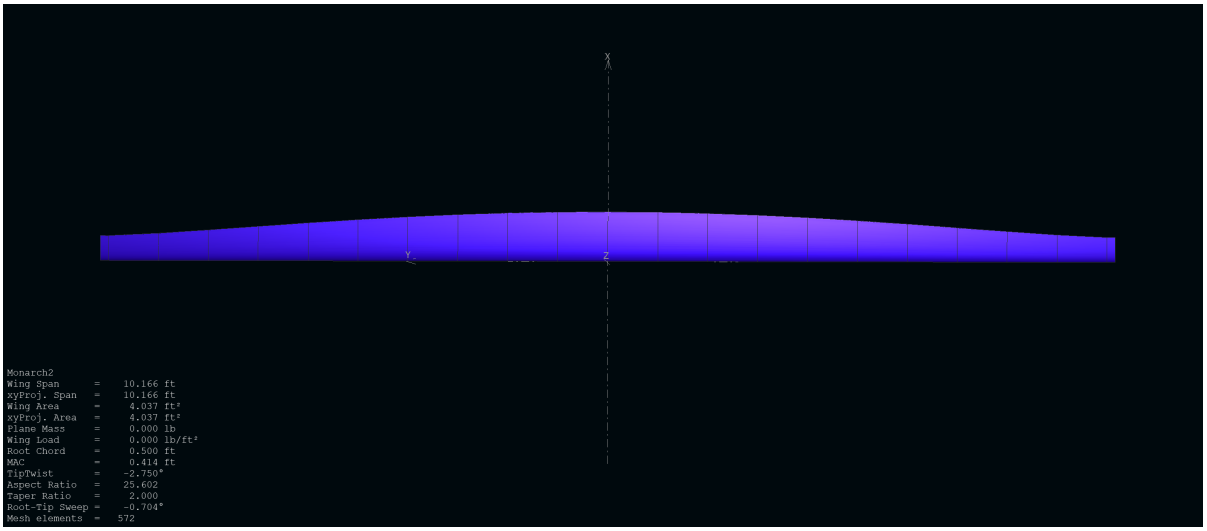

Figure 52: Wing Shape for BCCA in XFLR5

Attribute	MathCad	XFLR5 LLT	XFLR5 VLM2	AVL
α	0	-1.28	-1.23	-1.583
C_L	0.5	0.5	0.5	0.5
C_{D_i}	0.004368	0.00509	0.0040	0.004226
D_i	0.0260 lbf	0.0303 lbf	0.0238 lbf	0.0252 lbf
C_{D_P}	—	0.01657	—	—
D_P	—	0.0987 lbf	—	—
$C_{D,TOTAL}$	—	0.02166	—	—
D_{TOTAL}	—	0.1290 lbf	—	—
D_i/D_{TOTAL}	—	23.5%	—	—
L/D$_i$	114.469	98.23	119.922	118.3263

Table 8: Low Fidelity Performance of Monarch, BCCA

Attribute	MathCad	XFLR5 LLT	XFLR5 VLM2	AVL
α	0	-1.12	-0.68	-0.88
C_L	0.5	0.5	0.5	0.5
C_{D_i}	0.004368	0.00480	0.005	0.004787
D_i	0.0260 lbf	0.0286 lbf	0.0298 lbf	0.0285 lbf
C_{D_P}	—	0.0151	—	—
D_P	—	0.0899 lbf	—	—
$C_{D,TOTAL}$	—	0.01991	—	—
D_{TOTAL}	—	0.1185 lbf	—	—
D_i/D_{TOTAL}	—	24.1%	—	—
L/D$_i$	114.468	104.166	108.343	104.449

Table 9: Low Fidelity Performance of Monarch, BCVA

curve shaped wing variant performance values are tabulated in *Table 8 and 9*. Initially, this wing choice was preferred from an ease of manufacturing standpoint, but analysis shows

poorer performance compared to the Hershy bar configuration for similar variants. Consistently, the constant airfoil variant, BCCA, had a -4 difference in L/D for each analysis run, both LLT and vortex lattice. This held true for the varying airfoil variants of both wing iterations as well.

L/D is a decent indicator of lift to induced drag performance, but the variation in the solved induced drag coefficients is problematic. So far, the most accurate solving method consistent to the Lifting Line theory outlined in MathCad is vortex lattice analysis in AVL, with a % difference of 3.3 and 9.1 % for CCCA and CCVA variants. Considering consistency from a L/D standpoint, the constant airfoil variant demonstrated lower % differences across the board.

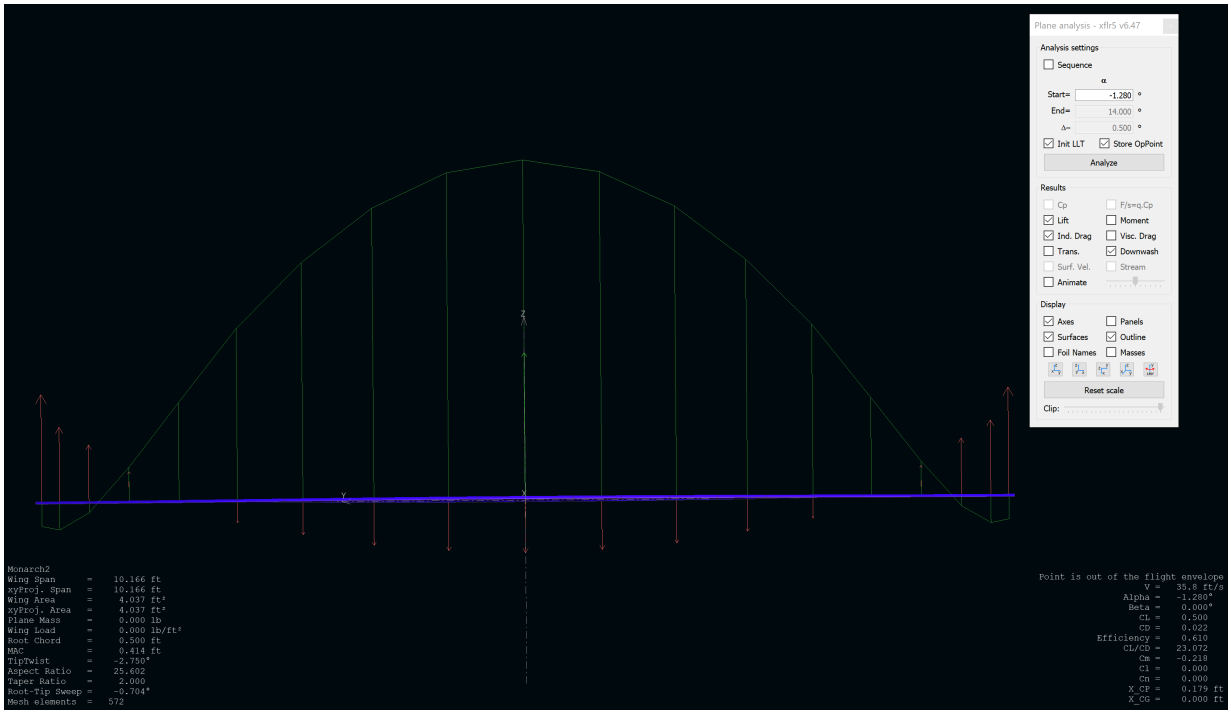

Figure 53: LLT Results in XFLR5 for BCCA

LLT analysis is shown for the BCCA and BCVA variants in *Fig. 53 and 54*. Although lift distributions for these wings are smoother, the observable upwash profiles follow the same trend as seen for the Hershy bar wing configurations; constant airfoil wings show a more consistent, smooth upwash region. Although this is qualitative assessment, continuity in this area is critical, as it demonstrates a more consistent flow assessment. This will be looked at closely in CFD analysis, as low fidelity analysis tools have their drawbacks and limitations, but so far, the results from these analyses show the constant airfoil wing variants having a better loading profile and improved performance over varying airfoil counterparts. The AVL readouts for this wing variant are shown in *Fig. 55*.

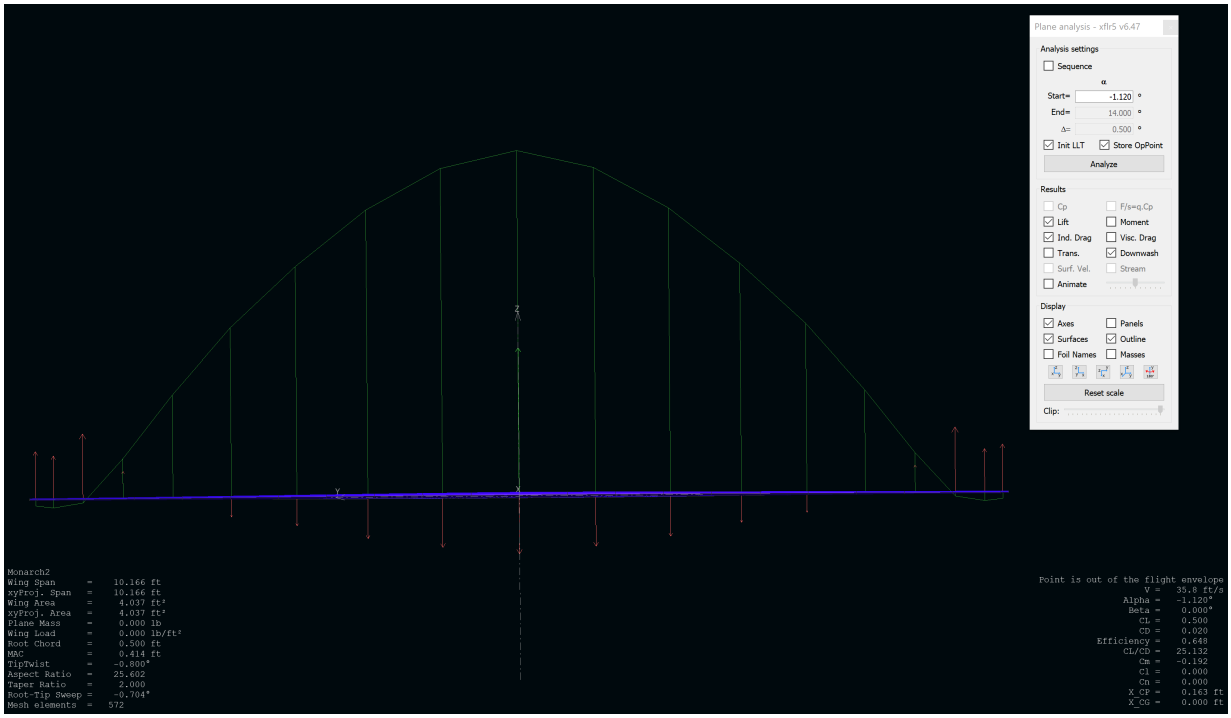

Figure 54: LLT Results in XFLR5 for BCVA

5.2.3 Iteration 3: Straight Taper

The straight taper wing iteration (STCA and STVA variants) held the most promise after completing analysis on the previous wing iterations, as it combined benefits of the previous two. The Hershy bar wing demonstrated better aerodynamic performance considering overall C_{D_i} and L/D, but the bell curve wing showed less aggressive twist distributions, which is desirable from a manufacturing standpoint. Both wings configured with a constant airfoil cross section demonstrated increased performance, more consistent results across difference low-fidelity solvers, and more consistent flow and downwash profiles across the wings in cruise flight. The geometry for this wing variant is shown in *Fig. 58*.

Analysis Results: Mathcad

Mathcad analysis was run on this wing iteration consistent to previous wing iterations. The resulting twist distribution is incredibly similar to the bell-curve shaped wing's geometric twist distribution, with higher local angles of attack for the first quarter of the semi-span, since comparatively, chord decreases at a faster rate and each wing section requires a higher aoa to produced the needed lift for the bell-curve lift distribution. Consistent with previous iterations, the varying airfoil variant requires less washout at the wingtips, and as observed previously, will more than likely result in a weaker upwash region at the wingtips (*See Fig. 56 and 57*). Consistent with previous Mathcad analysis results, the induced drag coefficient for this wing is $C_{D_i} = 0.437$.

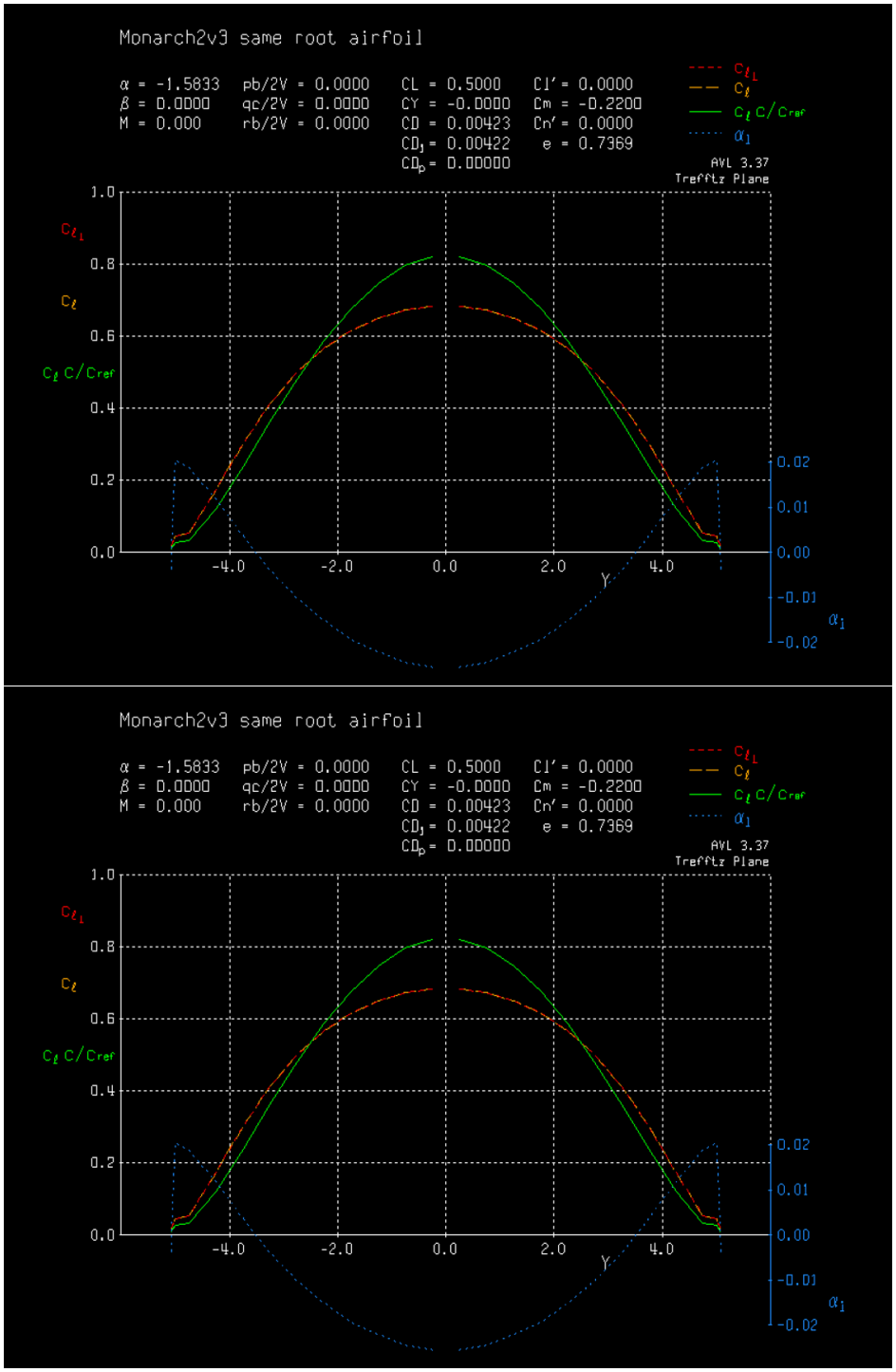

Figure 55: AVL output for BCCA, BCVA showing C_L and cC_L/MAC distributions

Analysis Results: XFLR5 and AVL

The results found from XFLR5 and AVL analysis for the straight taper wing are the most promising of all the wing iterations (*See Tables 10 and 11*). The constant airfoil variant achieved the highest consistent lift to (induced) drag ratio across all solvers when analyzing

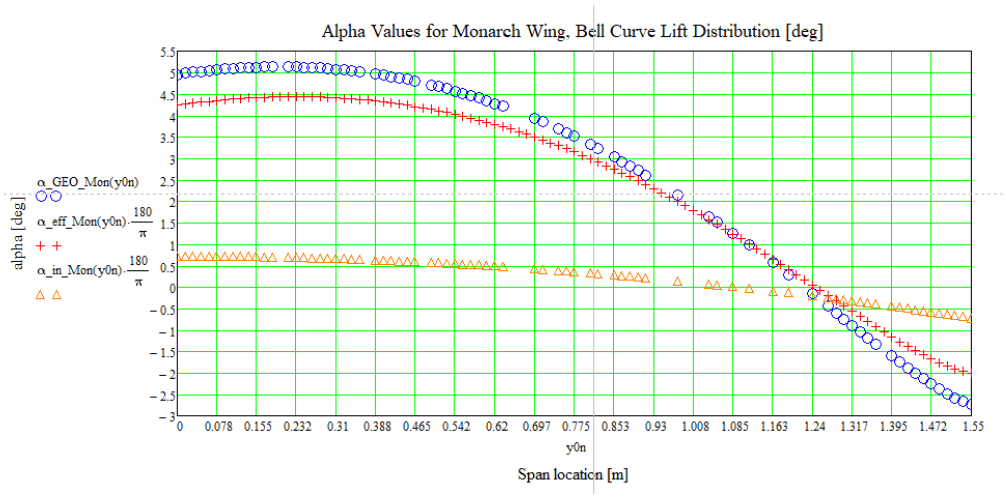

Figure 56: MathCad Geometric Twist, STCA

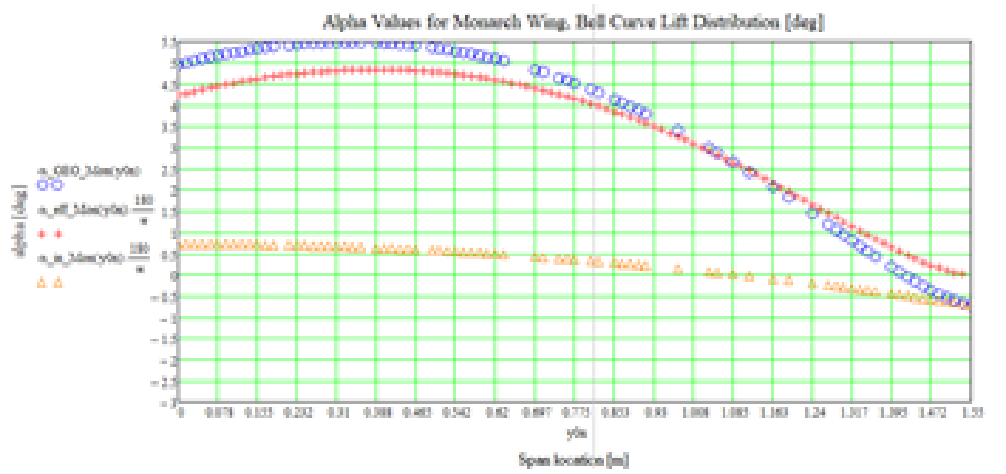

Figure 57: MathCad Geometric Twist, STVA

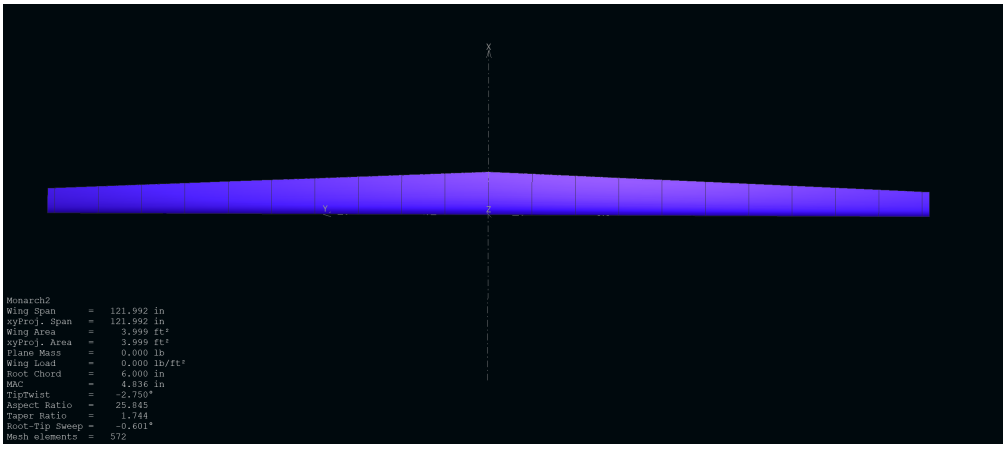

Figure 58: STCA Wing Shape in XFLR5

Attribute	MathCad	XFLR5 LLT	XFLR5 VLM2	AVL
α	0	-1.37	-1.36	-1.719
C_L	0.5	0.5	0.5	0.5
C_{D_i}	0.004368	0.00492	0.0040	0.0040447
D_i	0.0260	0.0293 lbf	0.0238 lbf	0.0241 lbf
C_{D_P}	—	0.01711	—	—
D_P	—	0.102 lbf	—	—
$C_{D,TOTAL}$	—	0.02204	—	—
D_{TOTAL}	—	0.1312 lbf	—	—
D_i/D_{TOTAL}	—	22.3%	—	—
L/D$_i$	114.469	101.626	125.258	123.618
% Reduction of C_{D_i}	5.63%	-6.27%	14.41%	13.3%

Table 10: Low Fidelity Performance of Monarch, STCA

Attribute	MathCad	XFLR5 LLT	XFLR5 VLM2	AVL
α	0	-1.16	-0.76	-0.968
C_L	0.5	0.5	0.5	0.5
C_{D_i}	0.004368	0.0047	0.004	0.0046102
D_i	0.0260 lbf	0.0280 lbf	0.0238 lbf	0.0275 lbf
C_{D_P}	—	0.01553	—	—
D_P	—	0.0925 lbf	—	—
$C_{D,TOTAL}$	—	0.02023	—	—
D_{TOTAL}	—	0.1205 lbf	—	—
D_i/D_{TOTAL}	—	23.2%	—	—
L/D$_i$	114.468	106.383	112.606	108.455

Table 11: Low Fidelity Performance of Monarch, STVA

at a constant C_L of 0.5, achieving a L/D of 125.26 and 123.62 for the vortex lattice methods. Compared to the original stock wing's induced drag of $C_{D_{i,Elliptical}}$ of 0.004621, this equates to a % Difference in induced drag of 14.41% and 13.3% compared to the baseline elliptical induced drag coefficient specified in section 5.1, and a 11.7% and 8.4% reduction in induced drag compared to the stock wing (untwisted), which is closer to the magnitude expected by Prandtl's original works.

Following the same trend, but seeing a much larger disparity, is the difference in L/D for VLM methods compared to the LLT method in XFLR5; the STCA variant achieved the second lowest L/D ratio for the given incidence angle, a 101.62. This is concerning but not unorthodox, since every wing performed poorly during XFLR5's LLT analysis and achieved a lower L/D than predicted in MathCad.

Looking at the lift distributions for the LLT, it is clear why it performed so poorly; even though the lift coefficient is 0.5, there are larger regions of negative lift at the wingtips, even though it operates with a bell curve lift distribution (*See Fig. 59*). With this, this wing

variant also has the highest negative angle of attack to achieved the needed C_L value, at a -1.36. Shown in *Fig. 61* is the resulting AVL, confirming a low induced drag coefficient and consistent bell-curve shape for cC_L/MAC.

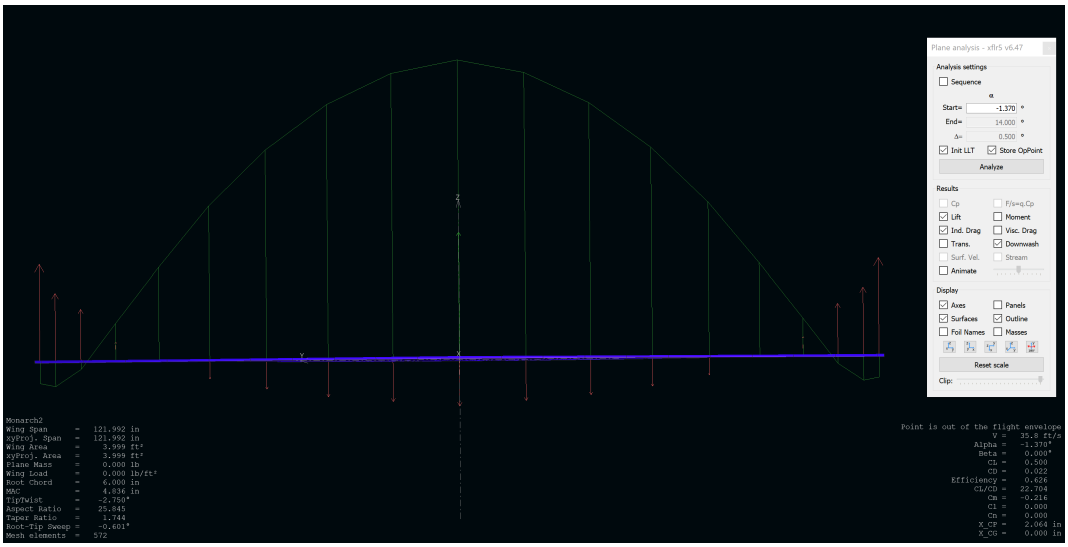

Figure 59: LLT Results in XFLR5 for STCA

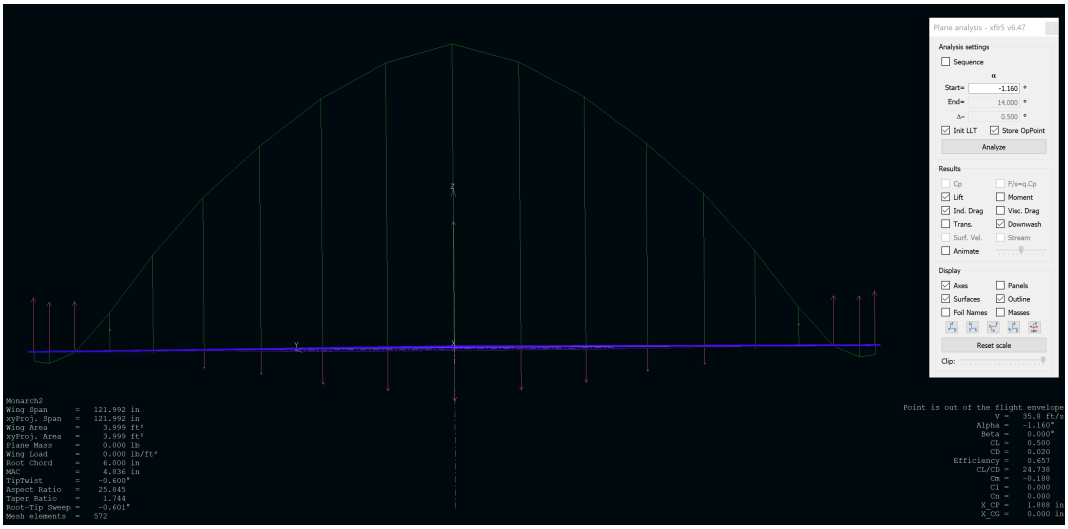

Figure 60: LLT Results in XFLR5 for STVA

5.2.4 Final Design and Substantiation: Straight Taper

The final design variant selected for high-fidelity analysis and manufacturing is the straight taper, constant airfoil wing, STCA. This decision was made due to the consistently high efficiency demonstrated in increased lift to induced drag ratios across the board, its less aggressive overall geometric twist and resulting larger stall angles, and its continuity with

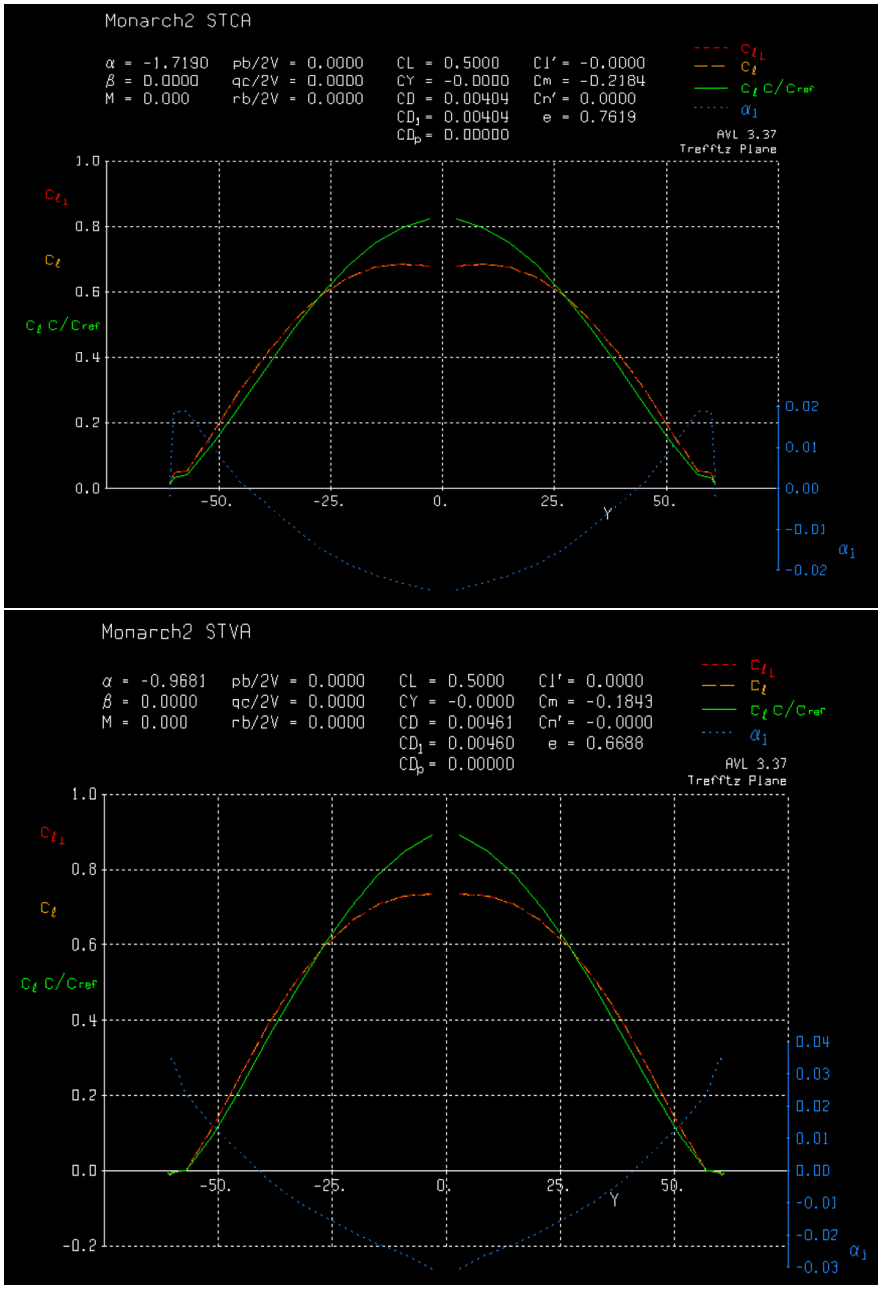

Figure 61: Vortex Lattice Results for STCA and STVA

the base MathCad code. The STCA wing variant demonstrated the highest aerodynamic efficiency, with a L/D of 123 and 125 from vortex lattice analysis. Although the L/D for LLT in XFLR5 didn't match this, the profile drag predicted in its viscous analysis is expected to be accurate, as it directly imports airfoil data from XFOIL analysis. This will be confirmed in the next section. The most comparable wing to this was the BCVA variant, which led to it initially being used to model and start 3D printing for stress testing (see *Chapter 8, Future Works*); The BCVA demonstrated a 12.5% smaller profile drag coefficient and a 2.5% smaller induced drag coefficient according to LLT in XFLR5, but a 22% higher induced drag coefficient in VLM2. These results are incredibly conflicting, but the latter

was chosen as validation for the new wing design; the STCA variant demonstrated a much higher L/D_i across the board, regardless of the smaller estimated profile drag coefficient. Ideally, because profile drag is a larger component of overall drag, the BCVA variant would be ideal for overall drag reduction, but because this body of work focuses on induced drag reduction, the STCA variant was chosen for high fidelity analysis. All performance figures can be seen in *Tables 12, 13, and 14.*

Attribute	MathCad	XFLR5 LLT	XFLR5 VLM2	AVL
α	—	1.55	2.00	1.766
C_L	—	0.5	0.5	0.5
C_{D_i}	—	0.00459	0.00450	0.0044
D_i	—	0.0273 lbf	0.0268 lbf	0.0262 lbf
C_{D_P}	—	0.01697	—	—
D_P	—	0.101 lbf	—	—
$C_{D,TOTAL}$	—	0.02156	—	—
D_{TOTAL}	—	0.128 lbf	—	—
L/D_i	—	108.94	111.11	113.64

Table 12: Low Fidelity Performance of Stock Wing, untwisted

Attribute	MathCad	XFLR5 LLT	XFLR5 VLM2	AVL
α	0	-0.89	-0.54	-0.80
C_L	0.5	0.5	0.5	0.5
C_{D_i}	0.004621	0.0047	0.00432	0.00423
D_i	0.0275 lbf	0.0280 lbf	0.0257 lbf	0.0252 lbf
C_{D_P}	—	0.01699	—	—
D_P	—	0.1012 lbf	—	—
$C_{D,TOTAL}$	—	0.02169	—	—
D_{TOTAL}	—	0.129 lbf	—	—
L/D_i	108.21	106.38	115.74	118.2

Table 13: Low Fidelity Performance of Ideal Stock Wing, twisted

Shown in *Fig. 62* is an overlay from the original MathCad results and the AVL results, showing continuity between the local C_l and cC_l/MAC distributions. This specific analysis was run on AVL at -1.36 degrees, which yielded a C_L of 0.5 in XFLR5's VLM2 analysis. Even though this AVL analysis resulted in a lift coefficient of 0.53 instead of 0.5, local lift coefficient distributions matched almost perfectly in the overlay. This demonstrates the model created in XFLR5, analyzed in XFLR5, and exported in AVL operates consistently with the base geometry specified in MathCad. This is crucial for demonstrating consistent performance across analyses.

The source of this inconsistency is believed to be the number of panels used in the analysis differing from VLM2 to AVL. An inconsistent geometry can poorly capture the very

Attribute	MathCad	XFLR5 LLT	XFLR5 VLM2	AVL
α	0	-1.37	-1.36	-1.719
C_L	0.5	0.5	0.5	0.5
C_{D_i}	0.004368	0.00492	0.0040	0.0040447
D_i	0.0260	0.0293 lbf	0.0238 lbf	0.0241 lbf
C_{D_P}	—	0.01711	—	—
D_P	—	0.102 lbf	—	—
$C_{D,TOTAL}$	—	0.02204	—	—
D_{TOTAL}	—	0.1312 lbf	—	—
L/D$_i$	114.469	101.626	125.258	123.618
% Reduction C_{D_i}, Twisted	5.63%	-4.57%	7.69%	4.47%
% Reduction C_{D_i}, Stock	—	-6.9%	11.7%	8.4%
% Reduction of $C_{D_i} = 0.004621$	5.63%	-6.27%	14.41%	13.3%

Table 14: Low Fidelity Performance of Monarch, STCA

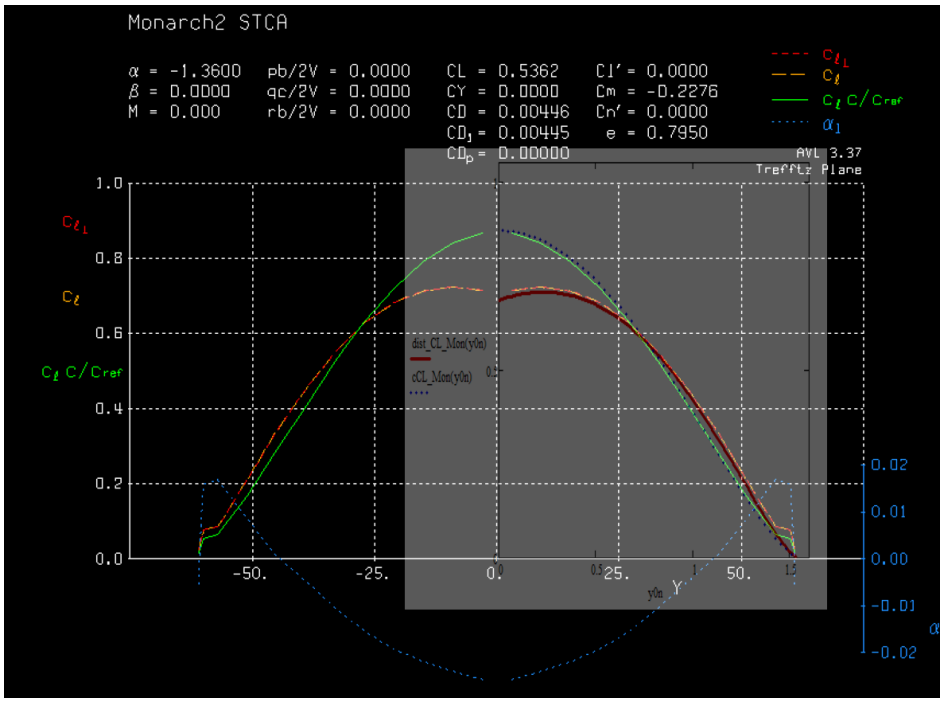

Figure 62: Overlay of Mathcad LLT results and AVL results, for C_l and $c(y)C_l/MAC$ distributions

small differences in each section's airfoil and geometric twist angle, which could result in smaller differences in the results of the analysis and slight changes in the representative lift distribution. Overall, regardless of these inconsistencies, the continuity from start to finish in low fidelity analysis, low profile drag, and consistently high L/D ratios made this geometry the most desirable iteration for Monarch's new wings.

5.2.5 Profile Drag Validation

Because LLT provides the best indicator of profile drag and overall drag to compared to future high-fidelity analysis, a custom Matlab script developed by Dr. Ryan Paul at Oklahoma State was utilized to import airfoil data from XFOIL into AVL, and perform analysis on the wing geometry for its profile drag and overall drag properties. As previously stated, it is expected that a major source of drag reduction will result from the change in the airfoil, so it is important to accurately predict the profile drag of Monarch's new wings, in order to gain a better understanding of the ratio of induced to profile drag for deconstruction of CFD results in STAR-CCM+.

The imported XFOIL analysis looked at the comparison between the stock wing's theoretical airfoil, the ClarkY, and the new custom airfoil for Monarch, named Monarch1, applied to the same STCA wing geometry (*See Fig. 63*). As shown, the airfoils produce near identical C_L v α and C_M v α sweeps, but performs better in drag over the expected flight regime, which based on current understanding, will span -4 degrees to 6 degrees, where the wing is expected to stall at the root.

Running the script, which imports this airfoil data into AVL and assigns it based on twist angle, the total drag properties of each wing are produced. As seen in the airfoil polars, a large overall drag reduction can be observed when using the new airfoil; the Monarch1 airfoil produces only 80% of the profile drag of the ClarkY while induced drag remains constant, resulting in a 17% reduction in drag overall. Profile drag from the Monarch wing also greatly resembled viscous drag calculations from XFLR5; LLT in XFLR5 predicted C_{D_P} at 0.01711, compared to AVL's prediction of 0.0169, resulting in a 1.17% difference. This difference is expected to come from the incidence angle of the wing, which changes from -1.37 to -1.72 degrees, but overall, this provides confidence in the resulting analyzed profile drag. From this analysis, it was derived that 23.66% of the overall drag for the final Monarch wing design in cruise flight is induced. Theoretically, if profile drag across elliptical and bell-curve loaded wings was the same and induced drag reduction was maximized, the overall drag reduction seen (ideally) would be 2.6%. The overall benefits of this figure and its application to other future aircraft will be discussed in later sections, but for this design, drag reduction is expected to be much larger from the decrease in profile drag from airfoil optimization.

Attribute	Monarch: Monarch1	Monarch: ClarkY
α	-1.719	-1.573
C_L	0.500	0.500
C_{D_i}	0.0040	0.0040
C_{D_P}	0.0169	0.0209
$C_{D,TOTAL}$	0.0210	0.0249
C_{D_i}/C_{D_P}	23.66%	19.5%
$\mathrm{L/D}_i$	125.0	125.0
$\mathrm{L/D}_{Total}$	23.81	20.08

Table 15: Matlab AVL analysis with Profile Drag Buildup

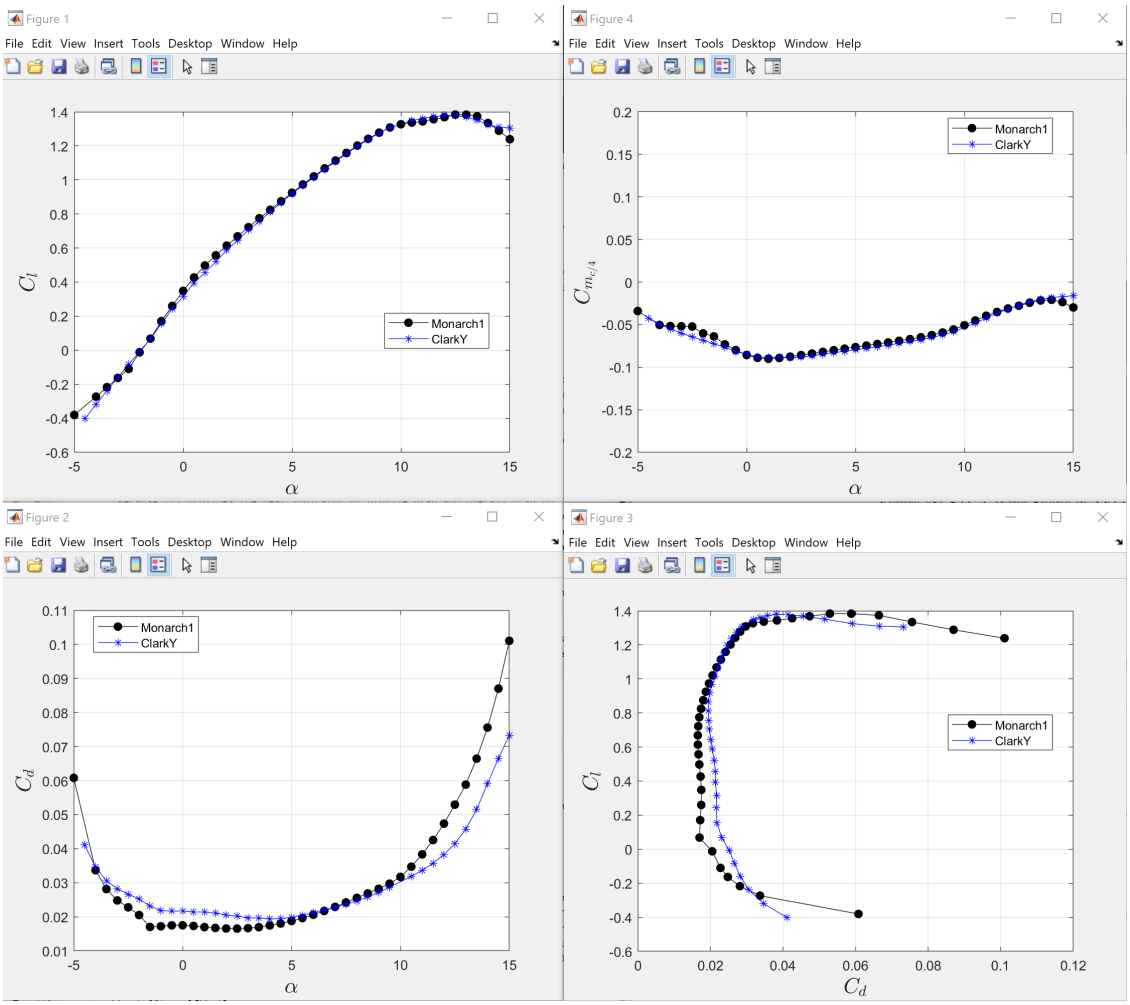

Figure 63: 2D Airfoil Performance Comparison between Monarch1 and the ClarkY

5.3 High-Fidelity Analysis: CFD

5.3.1 Construction and CFD Analysis

From the XFLR5 model, twist angles per 6 inch span section and airfoil cross sections converted to splines were imported into Solidworks for the construction of the wing, for 3D printing and and CFD analysis (shown in *Fig. 64*).

This body was mirrored across the longitudinal plane and imported into CFD as a parasolid. From there, mesh settings were copied in from the final mesh settings specified in section 4.4.2, as well as physics continuum specified in 4.4.1. The Star file was meshed and run on Oklahoma State's HPCC supercomputer, Pete, for 1200 iterations or until residuals reached a steady state (*See Acknowledgements and Fig. 65*). For low angles of attack where stall was not a problem, residuals measured in CFD leveled out after 450 iterations. The residuals plot can be seen in the figure below.

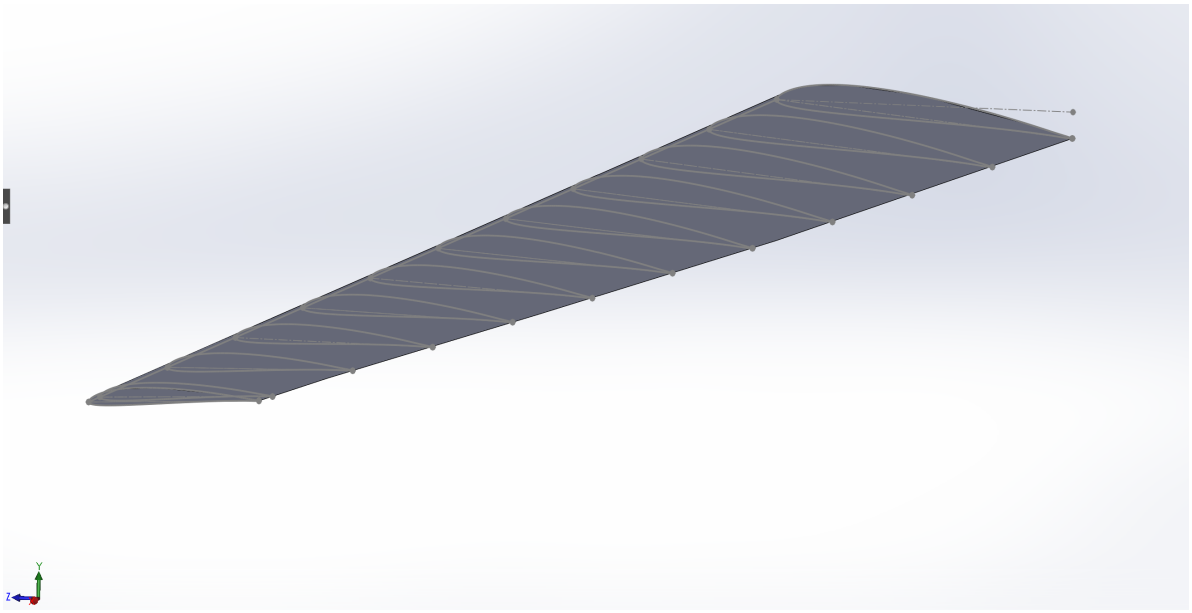

Figure 64: Solid Model of STCA in Solidworks, Iso View

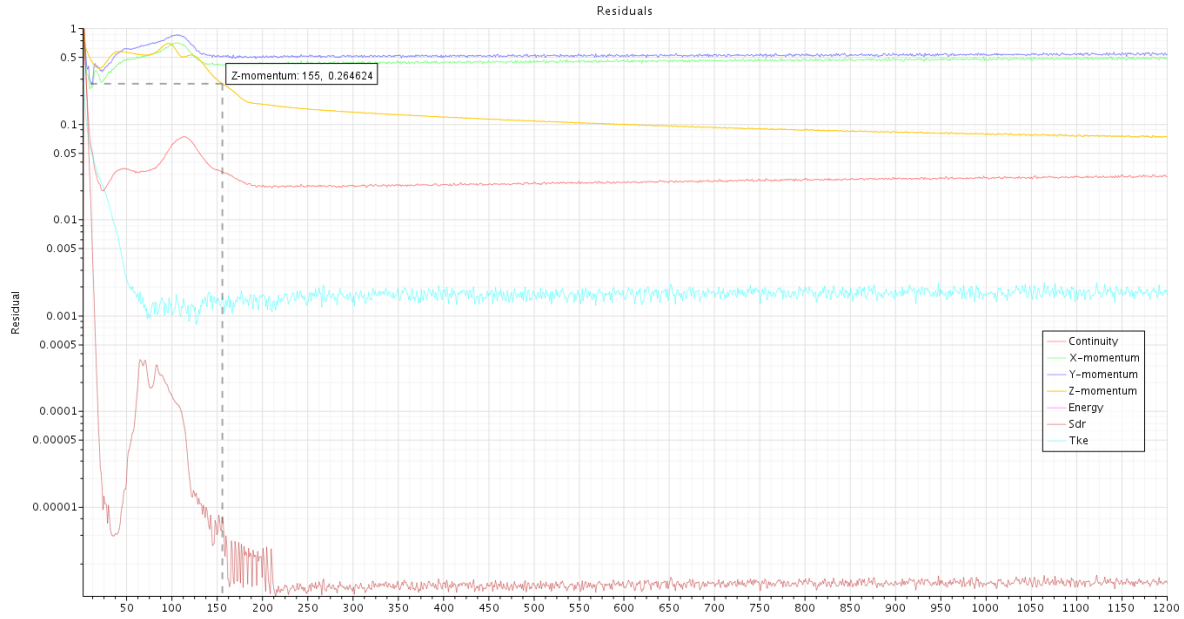

Figure 65: Residual plots for Monarch wings, -0.7 degree angle of attack

5.3.2 Constant CL Performance

Force and Coefficient Performance

After several variations in angle of attack (exposed parameter in STAR-CCM+), the incidence angle that produced a lift coefficient of 0.5 was -1.104 degrees (producing 3 lbs of lift), near the expected -1.36 found in XFLR5 and AVL analysis for the STCA wings. This analysis was run for 1200 iterations (as previously noted) to ensure residuals reach a

steady state. A histogram was defined along the wing's leading edge, trailing edge, and wing core to measure force distribution in the positive Y direction, or in this case, lift distribution along the span. The histogram was programmed to contain 90 bins along the span, roughly representing each inch and a half of the wing's length. The resulting lift distribution was exported into Excel to be compared to the defined lift distribution shape from MathCad.

The results are incredibly promising: as seen in *Fig. 66*, the lift distributions are a near perfect match from the original theory to the solid meshed model run at the same velocity. The lift distribution in Mathcad was per unit span, not per inch and a half, so a correction factor was added to compensate for this difference.

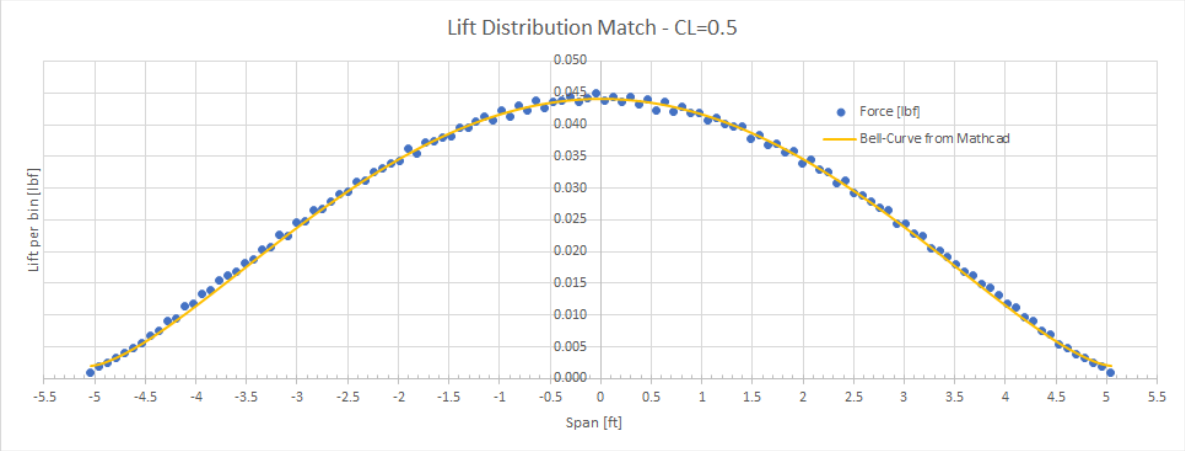

Figure 66: Lift Distribution Comparison: MathCad (orange) and CFD (blue)

This demonstrates continuity between the original base lifting line theory code in Mathcad to initially design the wings for the bell-curve lift distribution and the final model's high-fidelity performance - the goal of this entire effort.

Matching the lift distribution means the wing is generating near-perfectly predicted aerodynamic performance. Force and force coefficient plots defined before analysis runs show a total drag coefficient of 0.02274, equating to 0.135 lbf drag in cruise. Compared to the profile drag validation discussed in section 5.2.5, this is a 7.9% difference. If the ratio of induced to profile drag has remained the same, this equates to an induced drag coefficient of:

$$C_{D_{i,CFD}} = 0.00433 \tag{5.3.1}$$

This figure has a % Difference from the predicted Mathcad code of 0.87%. Considering the small differences in profile drag and theoretical induced drag, this is considered a successful simulation. The steady state results of the coefficient predictions are shown in the monitor *Fig. 67*.

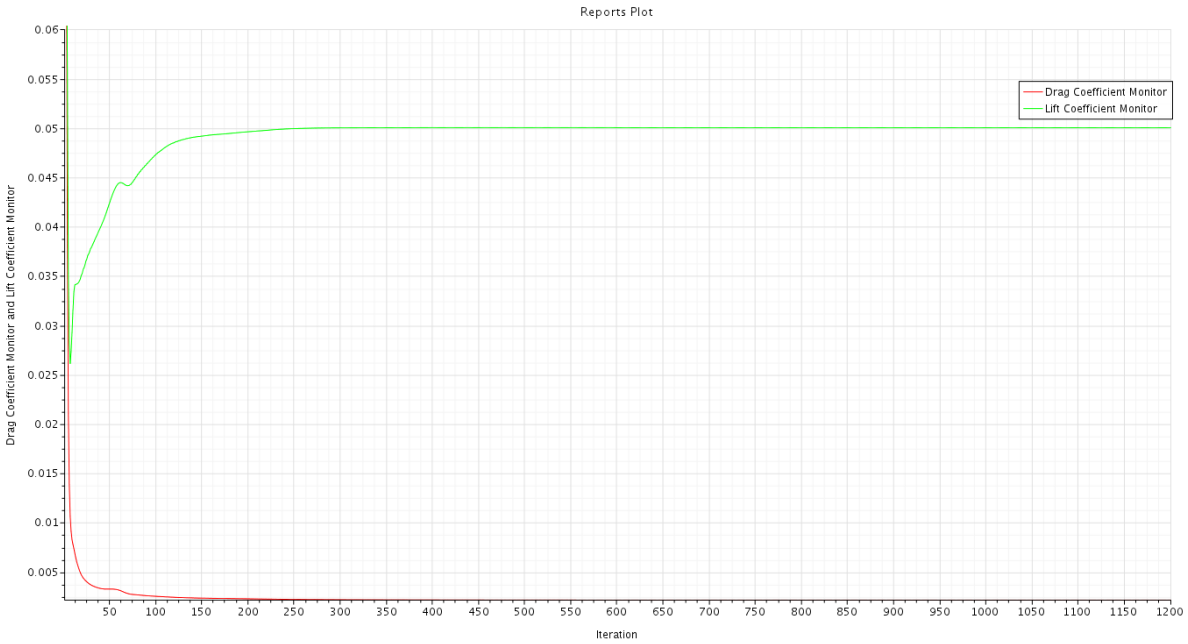

Figure 67: Lift and Drag Coefficients Plots in STAR-CCM+ at cruise conditions

Upwash Profiles and Vortex Shedding

Another important feature unique to the bell span loading that needed to be demonstrated in CFD is the upwash region of the wingtips, which is associated with the trailing vortex shedding of the wing. As stated previously, there exists a transition zone from downwash to upwash neat the 70% semi-span location where the main trailing vortex is shed, and outboard from this region is upwash, which allows for force redirection to induced thrust in a coordinated turn. Using a vertical velocity scalar scene in STAR-CCM+, this region can be visualized.

Seen in *Fig. 68* is a region near the wingtip that shows a positive velocity magnitude in the vertical direction, directly behind the wing. This scalar scene is visualized on a section plane placed directly below the bottom wing surface. As expected, the presence of this velocity region indicates upwash in this region, which equates to the outboard 1/4th of the semi-span.

Upwash indicates vortex shed right inboard of the velocity region. To visualize this, another sectional plane was placed 1m behind the aircraft's wing and a vortex vector scene was created to show the trailing vortex profile (*See Fig. 69*). This same strategy was used by the author and Scott Weekley in the analysis of Bellwether, and shows the peak of the vortex shed occurring at the predicted 70% transition zone on the wing [22].

Validating the location of the max vortex shed indicates the span load is operating with the proper lift distribution and downwash/upwash profile, a tripe check validation on the results. The magnitude and distribution shape of this vortex shed region needs to be ex-

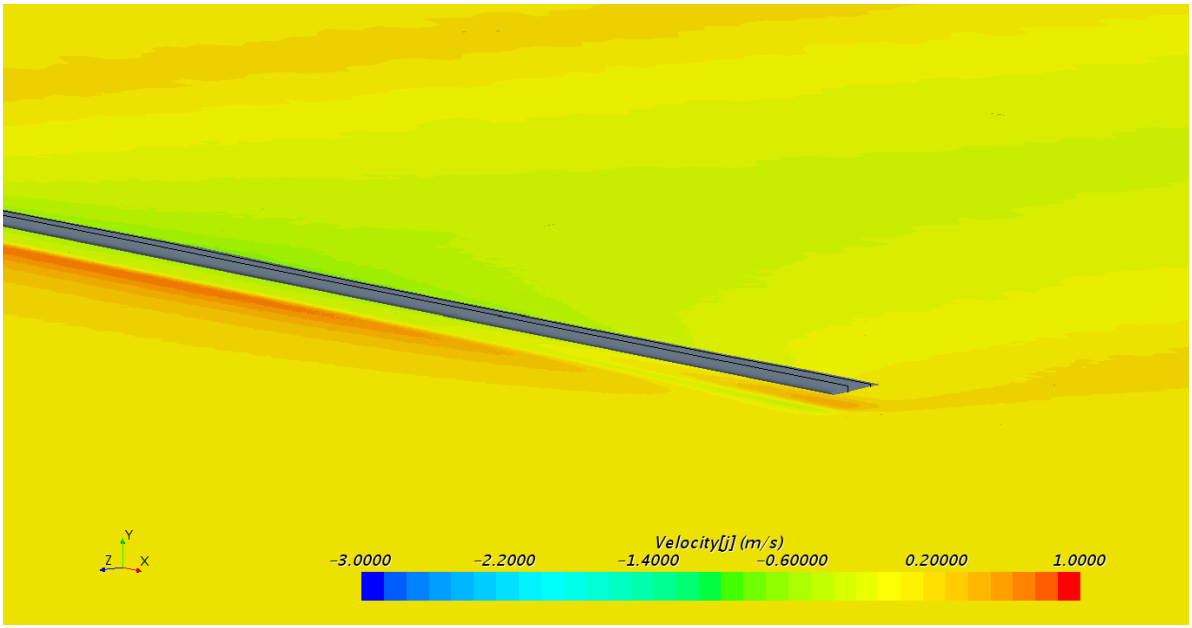

Figure 68: Vertical Velocity profile in wake of Monarch wing

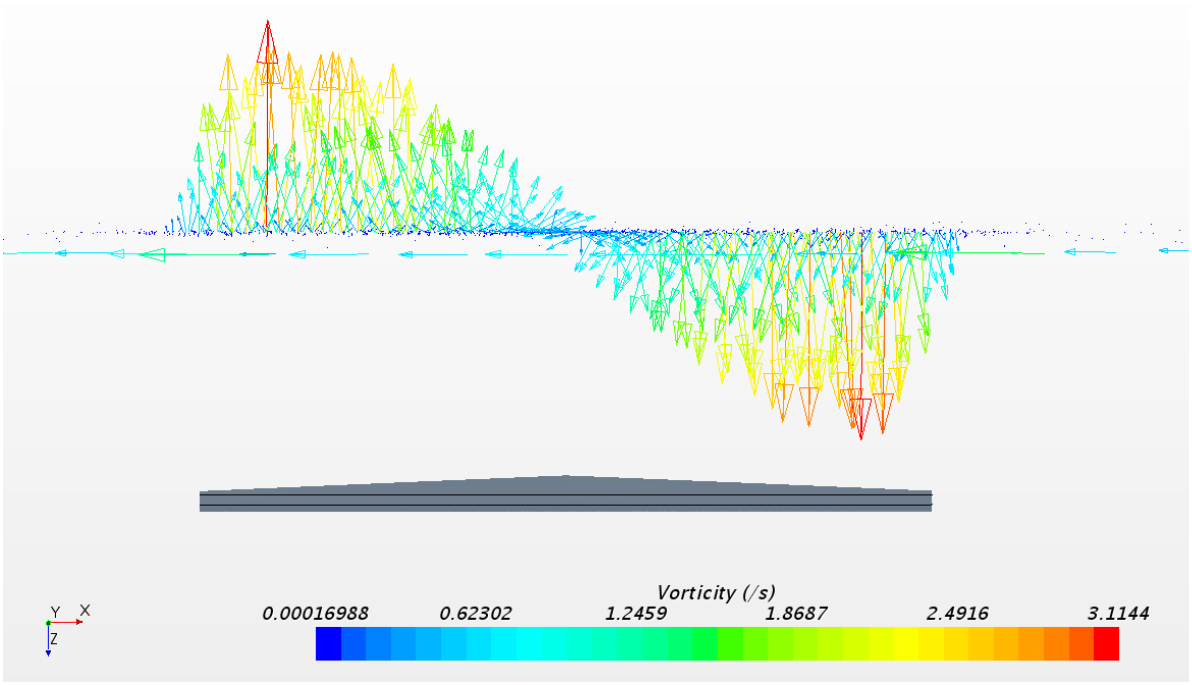

Figure 69: Top View Vorticity Scene of Monarch in Cruise

plored more in depth in future work, as the overall magnitude could indicate reductions in induced drag, due to less energy in the flow being transitioned into lateral kinetic energy. Finding easier and more reliable ways to represent the vortex shed distribution could lead to methods of further decreasing induced drag by manipulation of this vortex shed region.

Alpha Sweep and Stall

To further compare the wing's performance to low-fidelity analysis, and gain a better picture of stall characteristics of the wing, an alpha sweep was performed in STAR-CCM+ with the aide of Oklahoma State's HPCC supercomputer, Pete. The attitude of the wing was iterated from -4 to 16 degree in steps of 2 degrees, run, and the lift and drag results were tabulated (*See Fig. 70*).

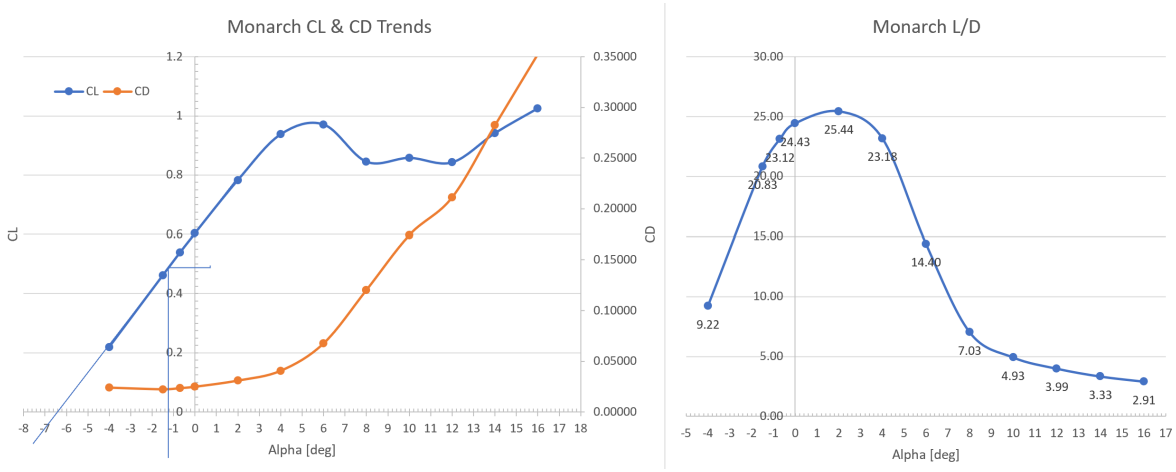

Figure 70: Alpha Sweep and L/D Performance of Monarch in STAR-CCM+

From this analysis, it shows the wing operating at a CL or 0.603 at 0 degrees, which compared to the CL value of 0.5 built into the MathCad, is a slight change. But, the wing has a CL value of 0.5 at -1.2 degrees, which still closely matches low fidelity analysis results, as stated above. This value will likely be the incidence angle that the wing is mounted to the fuselage at, which would give the aircraft its cruise condition lift generation at 35.75 ft/s as expected. From Figure 70, stall can be seen occurring at 6 degrees aoa. This, compared to other wings designed with an elliptical lift distribution, is relatively low, although the wing is producing far more lift at 0 degrees aoa. But unlike elliptically loaded wings, stall initially occurs at the root section of the wing, which although stall is undesirable, this keeps the aircraft from losing control once stall initially occurs The region from 6 to 12 degrees aoa seems to represent the period in which the entire wing stalls, leading to a massive increase in overall drag. Because the stall behavior of an aircraft implementing this span loading is relatively unknown, the results of performing a high aoa stall in flight testing will be interesting. This will be discussed in future work.

5.3.3 Fuselage Profile Drag

Using the same mesh settings as the Monarch wing (M4.3), while applying the surface constraints to smaller geometry, the bare fuselage was analyzed in STAR-CCM+ under the same flow domain and physics settings. Surface mesh controls were added to the nose cone, the vertical and horizontal stabilizer leading edges, and the interface between the tail and the

fuselage to further refine those more aggressive geometry changes. Similar to the wing CFD analysis, boundary layer capture and mesh refinement was checked before proceeding with analysis runs (*See Fig. 71*). Drag reports were created to analyze the overall drag the body was creating at cruise conditions, and the simulation was run for 2000 iterations. According to the residual plots, analysis reached steady state around 500 iterations.

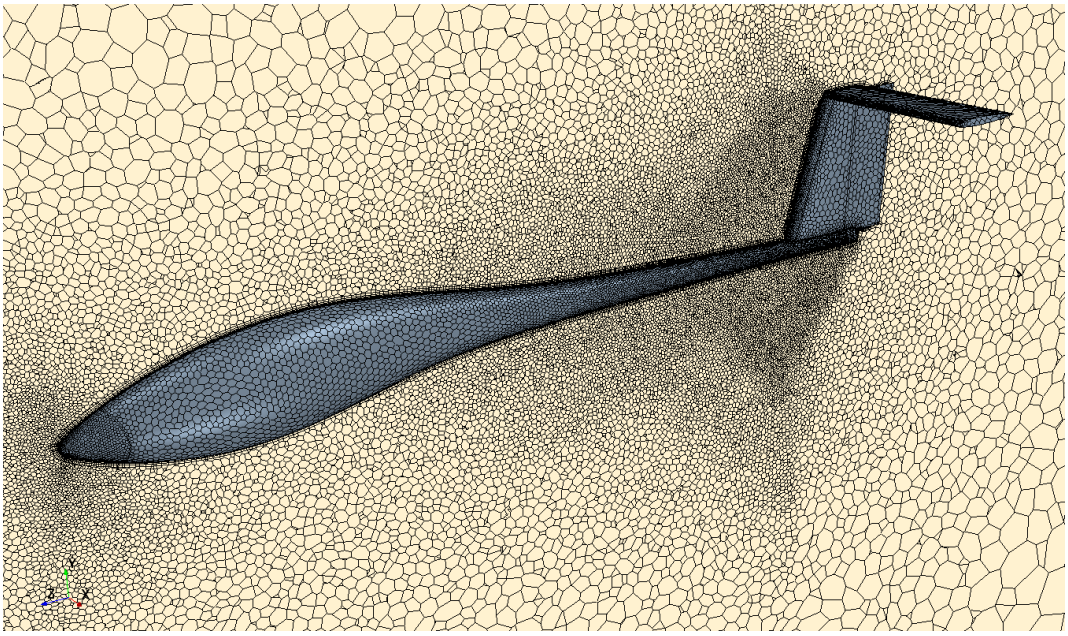

Figure 71: Fuselage Mesh in STAR-CCM+ using Mesh 4.3

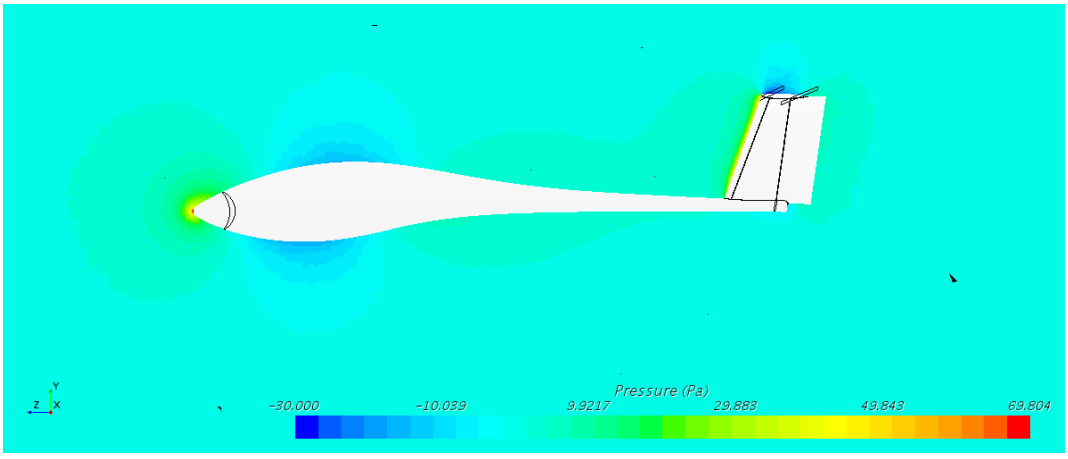

Figure 72: Fuselage Pressure Gradients in STAR-CCM+ at cruise

Drag results found the fuselage creating $D_{Fuselage} = 0.0411$ lbf of drag at cruise. From This is lower than initially expected, but because the wetted area for the fuselage is considerably lower than the wings, and the body is incredibly streamlined, this resulting figure is more realistic. The highest changes in pressure that could contribute to the drag are at

the stabilizer leading edges and the flattened nose cone, which was expected (*See Fig. 72*). Comparing the estimated drag to the total drag being produced by the STCA monarch wing (0.135 lbf according to previous CFD results), this composes 23.3% of the overall aircraft drag. Interference drag was not considered, since the expected amount is negligible compared to the propeller interference drag, which was also not included in the CFD analysis. This brings the overall estimated drag of the aircraft (from CFD analysis) to 0.176 lbf.

CHAPTER VI

CONCLUSION

6.1 Summary of Work

This body of work set out to design, analyze, and provide validation for the application of a bell-curve lift distribution to an existing high performance, straight wing aircraft with a stock elliptically loaded wing. Aided by low and high fidelity analysis techniques utilizing lifting line theory, vortex lattice analysis, and high-fidelity computational fluid dynamics in STAR-CCM+, meticulous analysis was run on 6 different geometrically constrained wing variants to explore the performance benefits of each, and select the most aerodynamic efficient design from an induced drag perspective to be manufactured and integrated into an existing Volantex ASW28 sailplane air frame.

A system for using Lifting Line theory inversely to back out the geometric twist distribution for any given wing geometry was developed and utilized to accurately apply a given bell-curve lift distribution to 6 wing variants: a bell-curve shaped wing, a Heresy bar wing, and a tapered wing, each designed with both a constant airfoil cross section and a linearly varying airfoil cross section, from a high performance low drag custom sailplane airfoil to a symmetric RAE101. By constraining a constant lift coefficient of $C_L = 0.5$, a wing area of 4 sq. ft, and a root bending moment of 2.633 lbf-ft, and increasing wingspan for the bell-curve loaded wing by 22% according to Prandtl's 1933 published works, an induced drag reduction of 5.47% was demonstrated under his strict design constraints; unfortunately, this is only half of his estimated performance increase.

Because the induced drag results of Lifting Line theory are dependent only on circulation and induced angle of attack, which is consistent along the span for each wing iteration, several different wing geometries with two variants of airfoil configurations were each analyzed using low fidelity analysis in XFLR5 and AVL, which utilizes vortex lattice methods and lifting line solvers to predict the aerodynamic performance of a given geometry. Each of the 6 wing geometries and their inherited bell-curve span loading twist distributions were imported into XFLR5 and AVL and analyzed at cruise conditions, with corrected angle of attack values to achieve a lift coefficient of 0.5. Tabulating the results from each analysis run for each wing variant, the tapered wing with a constant airfoil cross section (STCA) was selected over its opponents, as it demonstrated the highest consistent L/D_i ratio for vortex lattice analysis, at 125.26 and 123.62. Across the board, LLT analysis in XFLR5 seemed to over predict induced drag, resulting in a L/D_i of 101.63, but produced an accurate estimation of profile drag due to its integrated XFOIL analysis on each of the custom airfoil

geometries at the given flight condition. To confirm continuity between MathCad theory and AVL, C_L and cC_L/MAC distributions were overlaid, and they matched to a high degree of accuracy. Profile drag properties and improvements were confirmed by using a custom drag buildup method in AVL, which showed a 17% drag reduction overall from the Monarch wing with the stock ClarkY airfoil. From the same drag results, induced drag for the final Monarch wing composed 23% of the overall wing's drag.

Confirmation of the results found in low fidelity analysis was achieved in high-fidelity computational fluid dynamics in STAR-CCM+. This was preceded by an in-depth mesh resolution study and careful physics considerations. The given lift distribution exported from STAR-CCM+ analysis matches almost perfectly with the theoretical lift distribution from Mathcad and the lift distribution solved for in XFLR5 using vortex lattice inviscid analysis. This demonstrates continuity across all analysis platforms and more specifically the VLM solvers, and inherently the accuracy in the results of the analysis. Running an entire alpha sweep on the wing, as well as more in-depth analysis runs near the cruise condition was conducted, and lift and drag properties were derived from the results. At a cruise condition of near 0.5 CL, the wing produced an overall drag coefficient of $C_D = 0.02274$, which differed from the expected overall drag coefficient found in AVL by 7.9%. If the ratio of induced and profile drag remains constant, then this equates to an induced drag coefficient of $C_{D_i} = 0.00433$, which only differs from the design C_{D_i} in Mathcad by 0.87%. Last, CFD was able to show two different representations of the upwash profile outboard of the 70 percent semi-span location of the wing, which matches several previous researched works and confirms Prandtl's original 1933 theory.

6.2 Analysis Conclusions and Future Application Considerations

Using low and high fidelity analysis to analyze the performance of a wing with an experimental and efficient bell-curve span loading was a success; analysis results across the solvers used, including LLT, VLM, and RANS, showed consistent results from an optimized planform for this span loading, which demonstrated lower induced drag than its equivalent elliptical counterpart. From this analysis, the Straight Taper Constant Airfoil (STCA) was selected because it demonstrated the lowest D_i and highest performance over all the wing variants over the stock wing performance, as shown in *Fig. 73*. But the degree of this success near negligible, as discussed above; For an ideal case of 11% induced drag reduction, where a similar wing is modified to have a bell-curve span loading while maintaining the same profile and fuselage drag, the best performance increase achievable from the bell-curve span loading is a 2.53% reduction in overall drag for the STCA wing. The Monarch wing demonstrates a 13% to 14% reduction in induced drag over the elliptical induced drag coefficient according to results from AVL, which would equate to a best-case 3.22% reduction in overall wing drag. With the addition of the added drag from the fuselage, which was calculated to be 0.041 lbf and composed 23.3% of the overall aircraft's drag, this is a 2.47% in *overall aircraft* drag.

Putting aside best case scenario and considering the implementation of a bell-curve span loading onto the Volantex ASW28, and looking at the overall drag breakdown of the new

aircraft against the untwisted stock aircraft (not ideal, twisted elliptical version) shown in *Fig. 73* and *Table 16*, the resulting overall drag reduction of the wing was 0.86% and the overall drag reduction of the entire aircraft was only 0.66%. This is due to the increase in profile drag, which makes up a larger portion of the aircraft's overall drag, and the minute reduction in induced drag.

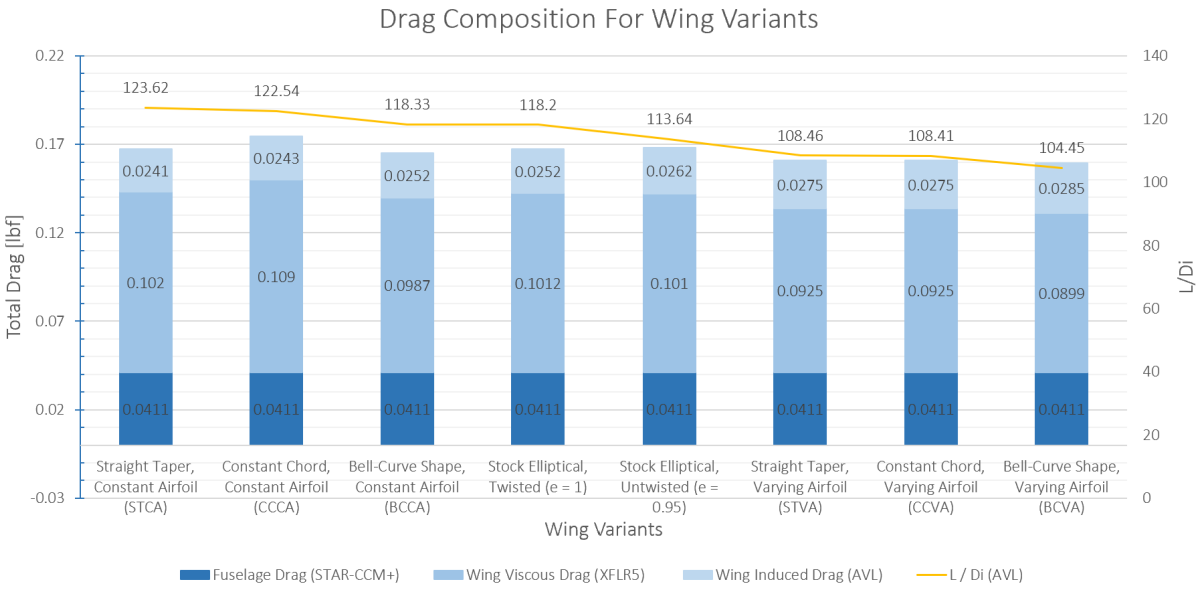

Figure 73: Drag Buildup and L/D_i for all wing variants

Attribute	Monarch: STCA	Stock Volantex: Untwisted	% Reduction (Stock to Monarch)
α_{AVL}	-1.719	1.766	—
C_L	0.500	0.500	—
$D_{i,AVL}$	0.0241 lbf	0.0262 lbf	8.02%
$D_{P,wing}$	0.102 lbf	0.101 lbf	-0.99%
$D_{P,fuselage}$	0.0411 lbf	0.0411 lbf	—
D_{TOTAL}	0.1672 lbf	0.1683	0.65%
C_{D_i}/C_{D_P}	23.66%	25.95%	—
L/D_i	123.62	113.64	-8.78%
L/D_{Total}	17.94	17.82	0.66%

Table 16: Drag Composition of Stock Volantex ASw28 aircraft (elliptical, untwisted) v Monarch (STCA) and % Reduction of Core Performance Values

Needless to say, this amount of *ideal* drag reduction is incredibly small when comparing the elliptical and bell curve span-loadings together, assuming the fuselage drag and wing profile drag remain constant. Previous sources, such as the work of Dr. Bowers, seem to over exaggerate the benefits of this span loading's applications without substantial data comparing it to an equivalent elliptically loaded aircraft [4]. The Prandtl-D and Scott Weekley's

Bellwether operate in a similar Reynolds's regime as Monarch (near 10^6), and even though flying wings lack a fuselage (which added 23.3% more profile drag for Monarch), the drag reduction is near negligible comparative to an elliptical span loading, as shown in this body of work. At the cost of extra design consideration, increased modeling complex, and costly manufacturing efforts, the only real benefit from this loading is proverse yaw, which is incredibly useful without yaw control from a vertical stabilizer. This has been demonstrated fully in previous applications of this theory to previous aircraft. That being said, the only realistic application for this span loading is on flying wings, and it isn't for the efficiency benefits, but for enhancing flight control. There is more work to be done in this realm of research when comparing both span loadings on the same flying wing geometry, to compare the actual benefits of it's application to overall drag performance when strictly following the base theory.

For a tube and wing aircraft, the bell-curve span loading isn't the new golden standard. There exists only two incredibly specific examples of it's potential benefit when applied to this classification of aircraft. For a cyclical aircraft that relies on incredibly long range flights or can demonstrate a reduction in operation cost from a 0.66% - 2.5% drag reduction over long periods of time, the implementation of a bell-curve lift distribution into the existing geometry can be recommended. But this type of aircraft may operate under an entirely different flight regime and may have a different composition of profile, induced, and overall aircraft drag, so more research will have to be done to see if the observed overall drag reduction is similar. But for aircraft that do not aim at long-term fuel reduction or are not hyper-optimized for long endurance missions, for which a larger percent of the overall aircraft's drag is contributed by the fuselage and tail, a 0.86% - 3% reduction in wing drag is not recommended over the complexity a bell-curve span loading will add to the wing geometry, so long as it isn't accompanied by a higher performing, more optimized airfoil. Deviating from this thesis's focus on the lowest induced drag value and instead considering profile and overall drag from planform twist and the airfoil, the BCVA wing variant actually outperformed the STCA wing by 4.71% in overall aircraft drag, even when induced drag is 16.7% higher. This points strongly to favoring planform and airfoil optimization over induced drag reduction for future aircraft that might benefit from the proverse yaw or *small* induced drag reductions, as profile drag composes a significantly larger portion of the total drag profile. Overall, for this classification of aircraft, an elliptical wing will perform just as well without needing to consider complex manufacturing, which will be discussed in future work (*See Appendix A*).

Moving forward in future work, the new wing design will be manufactured, integrated into the stock aircraft's fuselage, and flown to see if the estimated drag reduction from induced drag reduction in cruise and airfoil optimization holds true, or the difference is negligible. As previously noted, interference drag between the wings and fuselage and prop were neglected in analysis, which might further effect how the wings perform in cruise flight, whether by further reducing the drag benefits of the bell-curve span loading or reducing performance by alteration of the lift distribution in the prop's slipstream. These differences will need to be quantified and compared to the potential benefits found in previous analysis. Building on the calculated aerodynamic performance benefits, further considerations need to also be made for the complexity of manufacturing and future flight testing moving forward. Only then

will the validity of the bell curve span loading and its integration into existing air frames be confirmed and potentially recommended for future high performance, straight winged aircraft.

REFERENCES

[1] Ira H. Abbott and Albert E. Von Doenhoff, *Theory of wing sections*, Dover Publications, New York, 1949.

[2] John D. Anderson, *Fundamentals of aerodynamics*, 3 ed., ch. 1, 14, McGraw Hill, New York, 2001.

[3] Christopher P. Banfield, *Design and development of a 3d printed uav*, (2013).

[4] Albion H Bowers and Oscar J Murillo, *On wings of the minimum induced drag: Spanload implications for aircraft and birds*, NASA (2017).

[5] Bragado Estela Carrizalez, Martin and Mudassir Lone, *Non-elliptical lift distribution wings to decrease vertical tailplane size in commercial aircraft*, (2019).

[6] Joshua Patrick Deslich, *Effects of a bell-shaped lift distribution on an oblique flying wing and its impact on aerodynamic performance*, (2020).

[7] Mark Drela, *Xfoil: An analysis and design system for low reynolds number airfoils*, MIT Dept. of Aeronautics and Astronautics (1986).

[8] Aldo Frediani, Matteo Gasperini, Guido Saporito, and Andrea Rimondi, *Development of a prandtl plane aircraft configuration*, Department of Aerospace Engineering.

[9] Kevin Hainline, *Vehicle design study of a straight flying wing with bell-shaped spanload*, Engineering and Applied Sciences Theses Disertations **512** (2020).

[10] D. F. Hunsaker and W. F. Phillips, *Ludwig prandtl's 1933 paper conerning wings for minimum induced drag, translation and commentary*, AIAA (2020).

[11] D. F. Hunsaker, W. F. Phillips, and J. J. Joo, *Designing wings with fixed twist for minimum induced drag*, American Institute of Astronautics and Aeronautics (January 2017).

[12] Robert T. Jones, *The spanwise distribution of lift for minimum induced drag of wings having a given lift and a given bending moment*, (1950).

[13] Prandtl Ludwig, *Über tragflügel kleinsten induzierten widerstandes*, Zeitschrift für Flugtecknik und Motorluftschiffahrt **1** (1933), no. VI.

[14] Kyle Lukacovic, *A parametric study of formation flight of a wing based on prandtl's bell-shaped lift distribution*, (2020).

[15] Troy McMillan, *How to build rc 3d printed ask14 glider - planeprint*, Feb 2021.

[16] Massachusetts Institute of Technology, *Trefftz plane analysis of induced drag*, Aerospace Lecture Notes (2005).

[17] Gunther PFeifhofer and Helmut Tributsch, *The flight of albatross - how to transform it into aerodynamic engineering*, Scientific Research Publishing (2014).

[18] W.F. Phillips and D.O. Snyder, *Modern adaptation of prandtl's classic lifting line theory*, American Institute of Aeronautics and Astronautics (2019).

[19] Ludwig Prandtl, *Applications of modern hydrodynamics to aeronautics*, NACA **116** (1921).

[20] Jonathan et. all Richter, *Examination of proverse yaw in bell-shaped spanload aircraft*, (2019).

[21] R. Srinath and D. S. Sahana, *Aerodynamic analysis of forward swept wing using prandtl-d wing concept*, Mangalore Institute of Technology and Engineering.

[22] Scott Weekley, *Design and analysis of bellwether: A flying wing featuring the bell-shaped spanload*, (2021).

[23] Gregory A et. all Williamson, *Summary of low speed airfoil data*, 5 ed., University of Illinois, 2012.

[24] Justin et. all Winslow, *Basic understanding of airfoil characteristics at low reynolds numbers*, AIAA **55** (2018), no. 3.

[25] Seung Y. Yoo and Albion H. Bowers, *Computational fluid dynamics analysis of the stall characteristics of a wing designed based on prandtl's minimum induced drag*, AIAA (2018).

APPENDICES

Future Work: Manufacturing

To accomplish flight testing and gather flight data to validate overall drag properties of the aircraft, the wings needed to be designed to interface directly with the aircraft, without exceeding the stock aircraft's weight. Oklahoma State has extensive experience in composite manufacturing for complex wing shapes, so this was the first manufacturing strategy considered for the new wings.
Composite manufacturing, more specifically using fiberglass molds and light fiberglass weave for the aircraft's skin, was being explored by Scott Weekley for the manufacturing of Bellwether, the 26ft flying wing being developed at Oklahoma State's Unmanned Systems Research Institute. The most significant problem when developing the build strategy for that aircraft were the non-linear molds needed to create the fiberglass skin. Normally, wings for smaller unmanned aircraft have no geometric twist along the span, and because of this, the top and bottom halves of the wing's mold and molding plug have linear parting lines. The CNC machine used to mill the parting boards for the molds and the foam plugs cannot create negative geometry, so linear parting lines are needed for all pieces being manufactured in the lab. Due to the dramatic geometric twist needed for wings with a bell-curve span load, linear parting lines and flat parting boards are not an option.

For Bellwether, the solution was creating a linearly extrapolated parting line along the leading and trailing edges of the wings and fuselage, which creates a jagged and uneven top and bottom mold, and each half of the molds would be CNC'd from molding foam of different thicknesses.The non-linear parting lines can be seen in *Fig. 74*. This process is incredibly expensive and risky; CNC'ing the material results in a lot of wasted molding foam, and the two halves need to be machined and finished for a perfect fit, which hasn't been completely done by Oklahoma in the past.

For an aircraft with a 26 ft wingspan, the composite manufacturing strategy is still ideal for strength to weight of the wing structure, but for Monarch's wings, weight is the major concern; the new wings should ideally weigh the same as the original wings (235g), while maintaining enough structural rigidity to minimize flutter and wing bending in flight and without costing too much. Unlike the new constructed wings for Bellwether (*See Fig. 75*), the original wings are EPO foam-molded, which is unrealistic for a small-batch production, but good for overall strength to weight when mass producing wings. And to mold Monarch's wings using composites, two pieces of 4 inch molding foam would need to be CNC'd, meticulously primed and sanded for surface finish, then laid up with fiberglass and epoxy. This process is time consuming, experimental, and incredibly expensive; two 4 in foam pieces

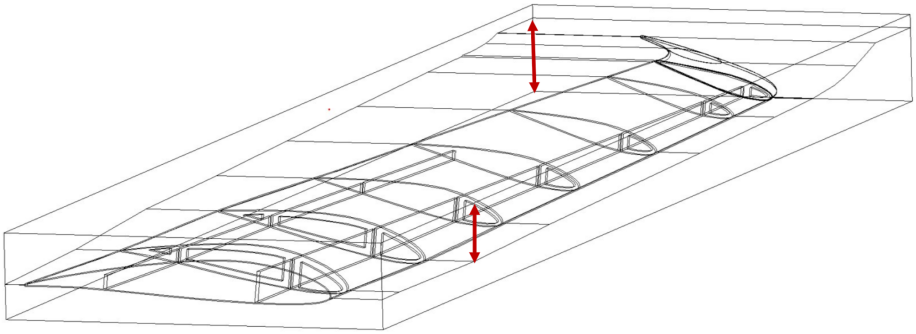

Figure 74: Isometric View of Bellwether's Non-linear Outboard Wing Mold

would total 984 dollars, not including cost of fiberglass, machining, and epoxy. The cost of the machinable foam alone costs 10x that of the original aircraft and x2 that of the autopilot and telemetry equipment on board. To summarize, composite manufacturing is risky and expensive, and a new manufacturing strategy needs to be explored.

Figure 75: Internal Layout for Bellwether: Fiberglass skin and internals

Composites are still incredibly important; carbon fiber pieces and rods have a very large strength to weight ratio and are relatively cheap, and are used exclusively in other projects at Oklahoma State. Ideally, carbon fiber tubes would act as the main structural spars, underneath an internal structure to form the wing shape. To create the complex, twisted wing shape, a cheaper alternative is needed to composites. Creating a wood (balsa) frame with a Monokote skin is a possibility, but making sure the outside wing surface is perfect is a challenging task, especially with Monokote or other heat treated frame wraps; the frame, referred to in this body as internals, needs to be perfect, and "dense" to make sure there are no sunken Monokote spots between the spars and ribs. This much wood internals needed, along with the Monokote skin, would likely exceed the weight needed for each wing.

3D printing the internals and monokoting the structure is not a new concept; a proof of concept was developed by Christopher Banfield at Oklahoma State University in 2013. His aircraft had a wingspan of 1 meter, a wing area of 1.636 sq. ft, and featured a composite

spar with 3D printed ribs and an Ultrakote surface finish. Total, with electronics, the model came out to 780 grams, an featured a less than ideal finish to the wing surface and inherently the wing shape, as seen in *Fig. 76* [3].

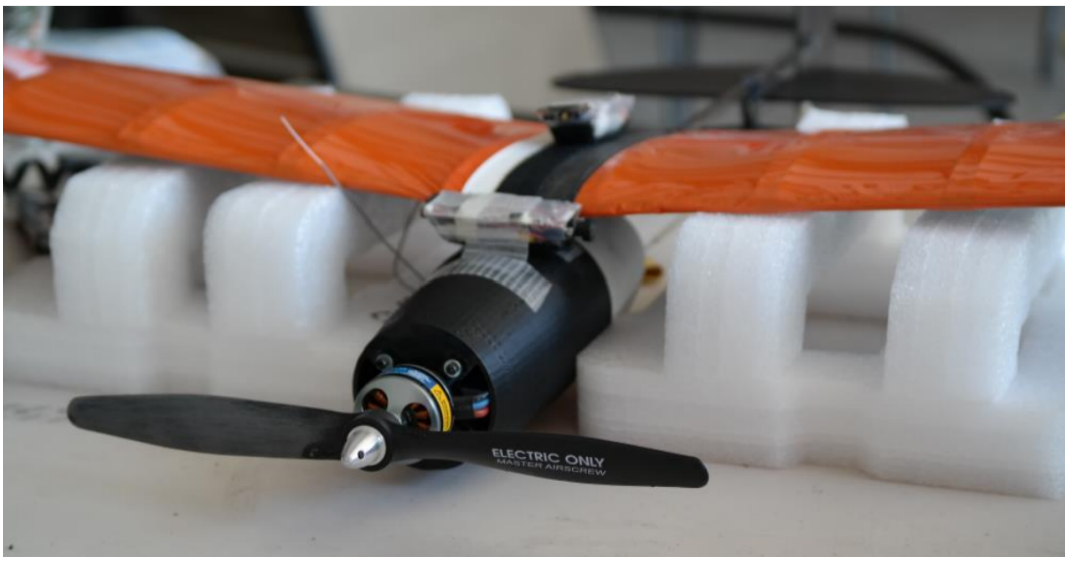

Figure 76: Christopher Banfield's 3D printed aircraft, with 3D printed ribs and a monokote-style covering

The selected final building strategy is 3D printing the wing structure with inserted carbon fiber internals. Several new sources have experimented with a new material called Lightweight PLA, or LW-PLA, and used the material to print entire aircraft on cheap 3D printers [15]. This material is a foaming 3D filament, that when printed correctly, can yield parts that are 50 % the weight of normal PLA parts (*See Fig. 77*).

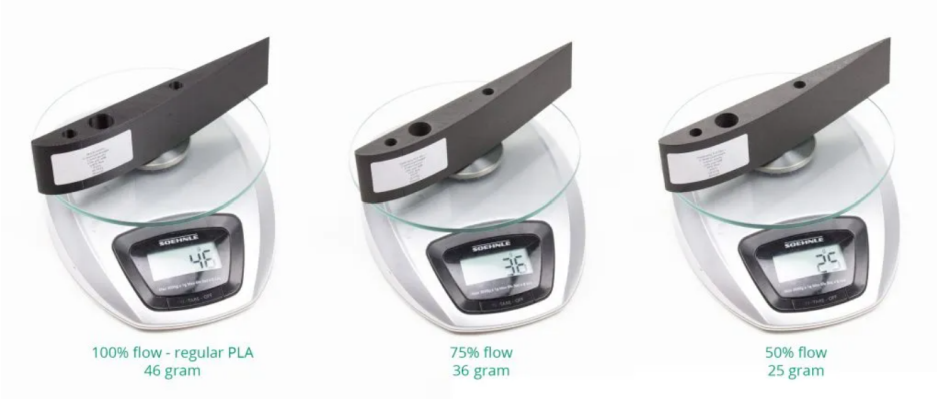

Figure 77: Weight comparison for PLA and LW-PLA at different flow settings (Colorfabb.com)

Unlike normal PLA, LW-PLA is printed at 230 Celsius, normally with a 30 to 50 % decrease in flow rate. To remain thorough, a 6 in root section for the Monarch Wing BCVA

variant, shelled to 0.4mm thick, printed with normal PLA on a Craftbot 3D printer weighed 62 grams, which confirms the need for LW-PLA. Although spools of LW-PLA are twice the price of normal PLA spools, the cost is still very cheap compared to composite molding. Most importantly, 3D printing is a cheap and incredibly precise way of manufacturing; if modeled and sliced in 3D printing software correctly, the geometry of the wing can be perfectly made. This is ideal, considering the performance is incredibly dependent on the airfoils and the geometric twist.

3D Printer Setup

The selected 3D printer used to complete printing of Monarch's wings is the Prusa Mini+, shown in *Fig. 78*. A cheaper member of the Prusa 3D printing family, the Mini has a 7" x 7" x 7" heated printing deck, with a 0.4mm extruding nozzle and an automatic bed leveler. The printer itself is incredibly compact and easy to transport, which made it ideal for use on this project, as manufacturing was completed in two different states. Created to be a single unit for a large printing farm, the Prusa Mini is known for it's reliability, easy to use features, and industry leading slicer software, Prusa Slicer. The Mini uses 3 stepper motors and a new 32 bit controller, that makes bed and extruder travel incredibly smooth and quiet. As far as size is concerned, because the 3D models of the Monarch wings are made in 6 inch sections, the smaller bed and lower cost printer was perfect for printing the wing in sections ready for assembly. For future manufacturing efforts, a larger printer capable of producing 12 inch wing sections would also be incredibly useful, considering there are 20 6 inch sections needed for the wing construction. But overall, test prints with LW-PLA on the Prusa Mini were incredibly successful, and will be discussed in later sections.

Figure 78: The Prusa Mini 3D printer used for Manufacturing

Modeling and Internal Design

Two different strategies were taken for modeling the wing to be 3D printed: creating a shelled, hollow structure with ribs, and utilizing a feature in the selected 3D slicing software called "Vase Mode", which included a solid part and small extruded cuts where internals needed to be. Using a shelled model was attempted first, and resulted in a clean geometry consisting of two major spar tubes aligned with the original spar tubes on the fuselage, and several layers of diamond shaped internal ribs, visualized in *Fig. 79 and 80.*

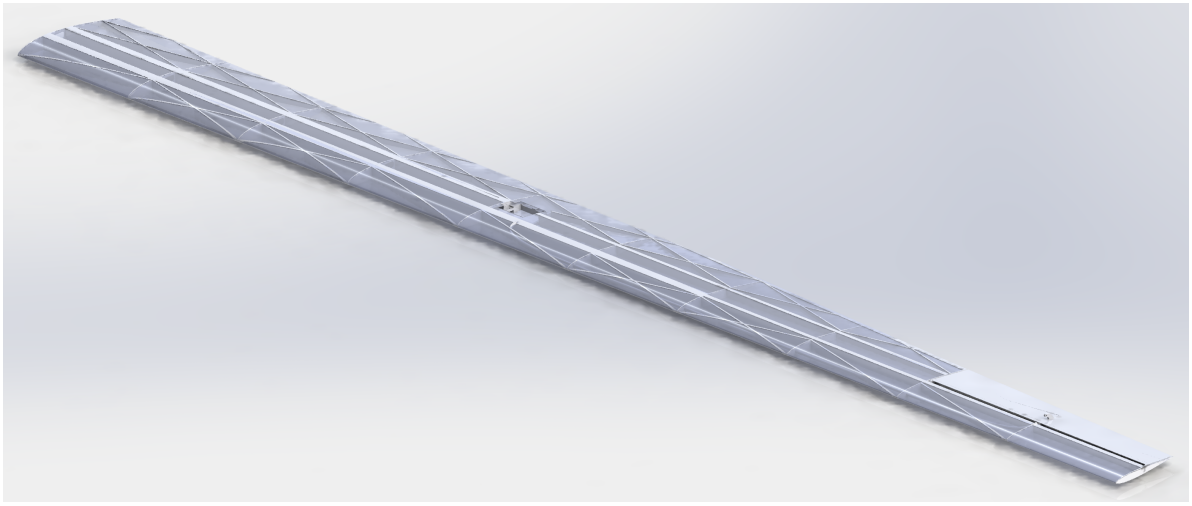

Figure 79: Shelled Model render in Solidworks

This model uses a 0.4mm thickness on all ribs and shelled solids, consistent with the size of the extruder on the Prusa Mini. This design decision followed a series of iterations looking at different shell thicknesses and resulting weights of the print, starting from 0.86mm and working down. LW-PLA is a foaming filament, meaning when the extruder heats up past 215 °C, the filament foams, increasing its volume by 300 % and exiting the extruder near 0.4 mm thick. Because the extruder keeps the temperature consistently above 215 degrees Celsius, and the final wing prints were made at 245 degrees Celsius, the filament cannot retract. This means, the extruder on the printer cannot pick up from the part it's printing and move to a new area - each layer on the part needs to be one continuously printed bead of LW-PLA. The shelled models posed a challenge in this area, and even with meticulous iterations made to 3D print settings, retraction could not be avoided. This meant the wing sections included extra filament that was not structurally necessary, made the inside of the wing sections incredibly messy, and the outside finish rough.

The first wing, which was printed in order to complete stress testing, was printed using the shelled 0.4mm model shown in Fig. 62. The BCVA variant was used as the main wing geometry, as it was believed to be the most promising wing variant at the time, and the internals were constructed with a main spar sleeve for a 8.3mm carbon fiber tube, an auxiliary spar sleeve for a 3.5mm carbon fiber rod, and 3 rows of diamond shaped internals to keep the thin skin from warping during printing. All structures were 0.4mm thick. This

wing was printed in roughly 100 hours, averaging 9 to 10 hours per section. The surface finish, because stringing was non-avoidable in the slicer software, was incredibly rough and therefore unacceptable for any type of flight testing or potential wind tunnel testing. The printed wing with an 8.5mm carbon fiber spar and a pre-selected Corona Thin Metal Wing Servo weighed 305 grams, 70 grams more than the original wing weight for the same wing area, thinner airfoil cross sections, and one servo compared to two for the original (flaps and aileron). For future reference, the root sing section (6in in length) weight 34 grams.

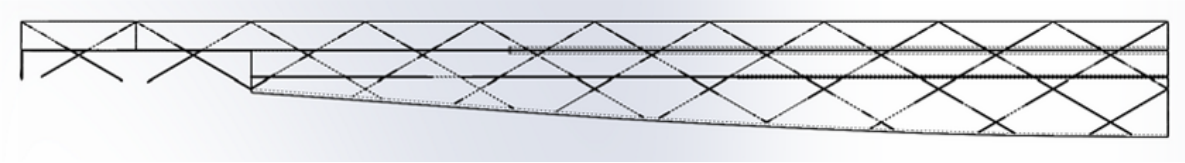

Figure 80: Shelled BCVA Top View in Solidworks, showing internal structure

This model, although only being used for stress testing and printer calibration, was a good indicator of what changes needed to be made. Entirely overweight, this was contributed to the flow rate of the filament, set to 100 %, the amount of stringing present on the inside of the wings, and the redundancies in the internals.

The second and final iteration of the wings were made using the Prusa Slicer's Vase Mode. Unlike the previous iteration's printer settings, this took a solid model and created an outside shell inside the slicer rather than Solidworks, that was only one later thick along solid boundaries. After careful iterations with test sections, it was found that 0.125mm thick extruded cuts through one surface of the wing up to 0.5mm from the other surface could create internals two layers thick, or 0.8mm, that connected each of the wing surfaces in the prints. Vase mode is also incredibly useful because there is no retraction, and pieces can be printed entirely without picking up the printer nozzle from the piece, which takes away stringing entirely, as shown in *Fig. 81.*

Once this consideration was made, test root sections were printed at a range of temperatures and flow settings; from 230 to 250 degrees Celsius, and 100 to 30 % flow. From those test sections, 245 degrees resulted in the cleanest prints without creating thick wing sections, and 70 % flow resulted in the strongest sections that didn't show signs of warping. These two print settings, along with Vase Mode, were used for the remainder of the printed pieces. This geometry was created once low fidelity analysis was completed, so the STCA wing variant was selected and modified for manufacturing.

The resulting wings now included two 8.3mm carbon fiber spar sleeves to interface with the Volantex fuselage, which utilized the stock steel spar tubes and a 48 in carbon fiber tube to span the length of the wing up to the aileron. Among this, the wing also included only two rows of diamond shaped internals to minimize warping and increase strength, a sleeve to hold the 3mm carbon fiber control rod for the aileron, a slot for the servo 12 inches from the root, and a wing tip to hold the other end of the aileron control rod (*Fig. 82*). Also characteristic of Vase Mode is a two layer solid base for each part, which resulted in automatic ribs

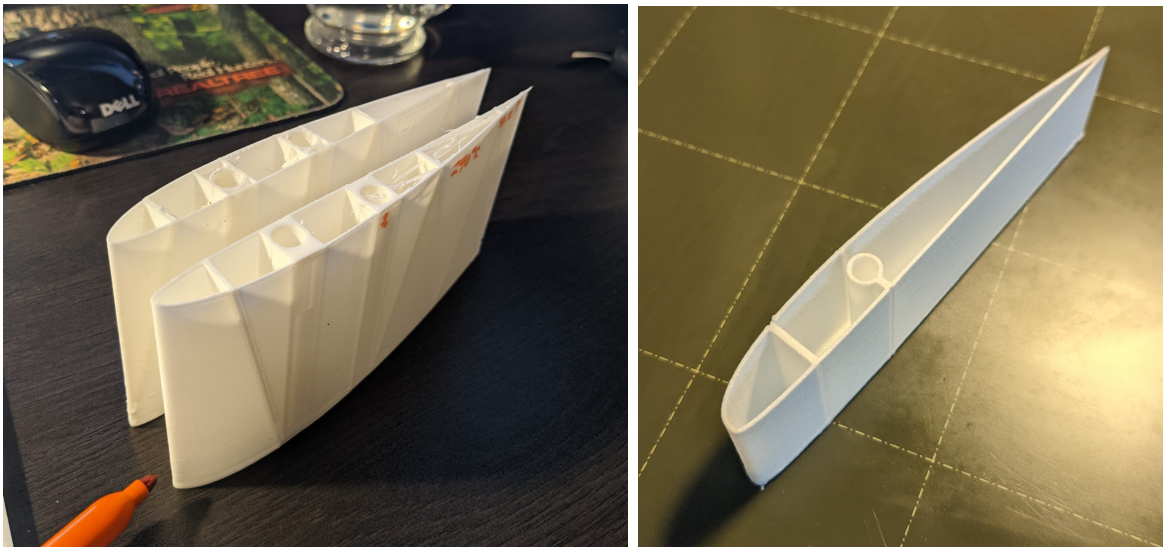

Figure 81: Monarch Test Sections: Shelled (left) and Solid w/ Internal Cuts (right), showing disparity in stringing and overall finish

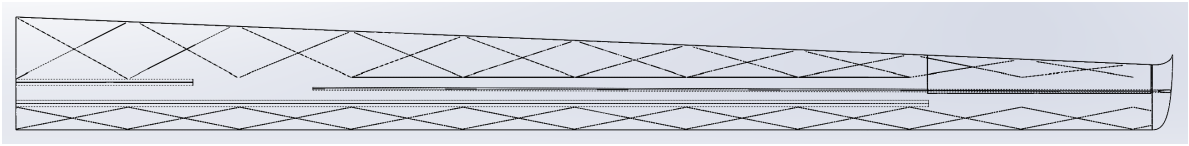

Figure 82: Final Monarch Wings: Solid STCA with Internal cuts, showing internal structure

for wing sections ever 6 inches, which helped with assembly and overall structural rigidity. The total wing spanned 5 feet 2 inches, with a wing area of 2 sq. ft each (4 sq. ft. total), and a total weight of 260 grams including the wing servo, servo extensions to reach the fuselage, a 48 inch 8.3mm carbon fiber tube, a 40 inch 3.5mm carbon fiber control rod, wing tip, and aileron. This puts the wing 25 grams above the original wing weight, a % difference of 10.1 in overall weight. Compared to the previous root section being 32 grams with LW-PLA and 62 grams with normal PLA, the new root sections printed with Vase Mode are 22 grams. Most importantly, the new wing sections were printed in less than 2 hours 20 minutes, compared to the shelled wing model sections, of which prints took between 9 and 11 hours to complete. Overall, a complete wing was printed in a single day, compared to a week needed for the first iteration. The slicer UI and the resulting print for the root section of the wing can be seen in *Fig. 83*.

Stress Testing and Results

The first 3D printed wing variant, a 0.4mm shelled model of the BCVA wing, was printed and assembled with a single 48 inch, 8.3mm carbon fiber tube as a main spar, spanning 36 inches from the root with 12 inches of spar extruded from the root wing section. The wing was composed of 10 6 inch sections, bonded together using fast-bonding InstaCure CA glue and accelerator, which added negligible weight. An inch of the root of the wing and

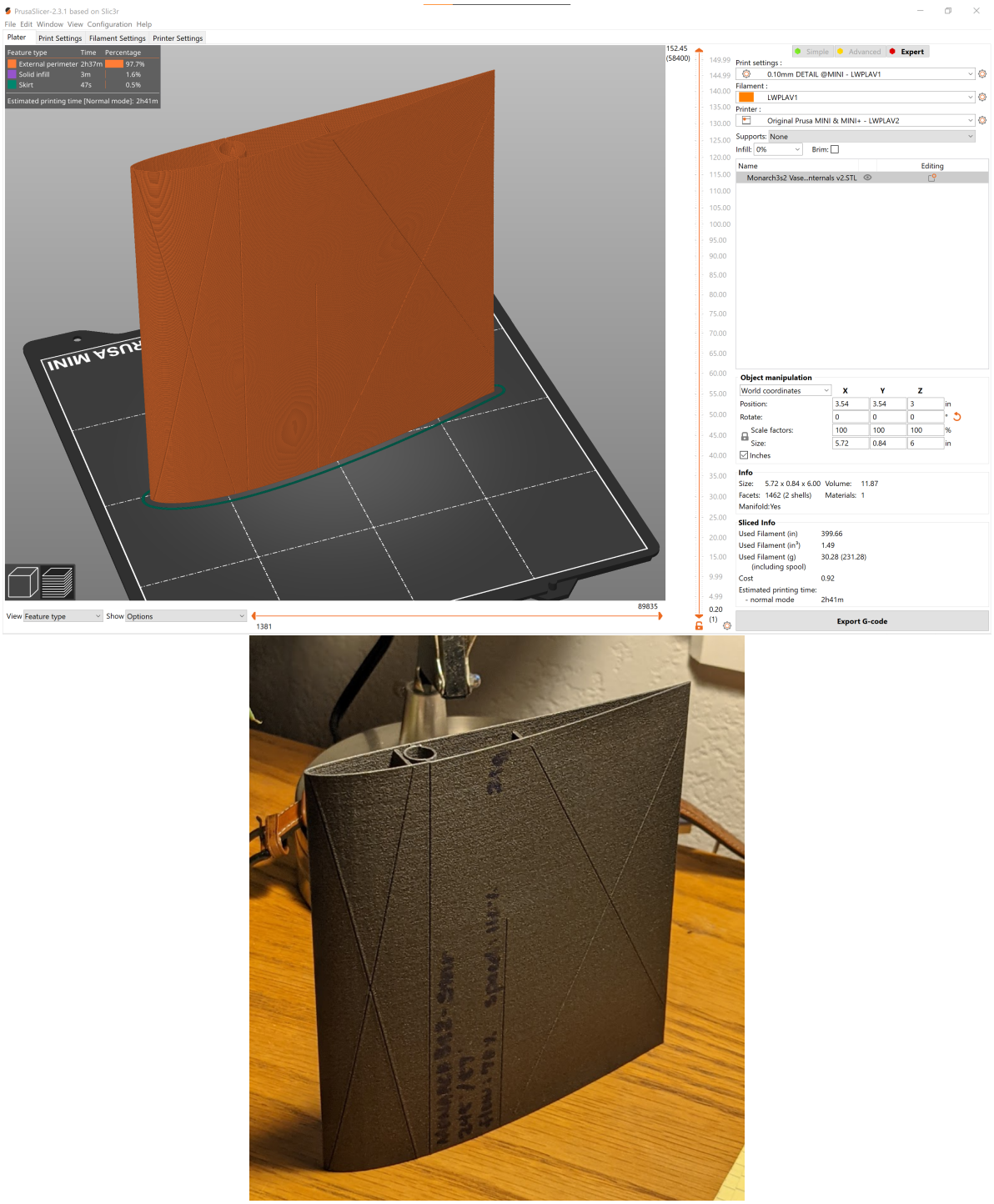

Figure 83: Prusa Slicer UI (top) and Resulting Final Printed Section (bottom)

the extruded foot of spar were secured to a table with the wing oriented upside down, and machined plates were added along the span to see deflection and material deflection.
Using a weight buildup method to see material failure point, the wing was able to hold 5.7 pounds of force 40 inches from the root before the LW-PLA wing sections after the end of the

spar and at the root started to yield and buckle (*Fig. 84*). The weight was placed initially at the end of the spar, but to truly see the material's ability to hold weight without the carbon fiber reinforcement, the weight was moved 4 inches past the end of the spar. Together, the spar and LW-PLA wing sections were able to hold a root bending moment of 19 lbf-ft, which is equivalent to a loading factor of $n = 7.21$. Under this loading, the wing deflected near 20 inches from horizontal to the point of the weight loading, which indicates that if the wings experienced such loading in flight, the amount of flutter will be drastic. Taking this into consideration, the final wing design added two spars at the root and a 3.5mm carbon fiber aileron control rod that also acted like a secondary spar.

This simple test was able to demonstrate the materials ability to hold the loading without the need for complex FEA analysis, considering the material used is new and experimental.

Figure 84: Max Loading on 3D printed Wing before Yielding: 5.7 lbs 40 inches from root

Attribute	MathCad	XFLR5 LLT	XFLR5 VLM2	AVL
α	0	-1.3	-1.38	-1.75
C_L	0.5	0.5	0.5	0.5
C_{D_i}	0.004368	0.00490	0.0040	0.00408
C_{D_P}	0.0	0.01833	0.0	0.0
$C_{D,TOTAL}$	0.0	0.0023	0.0	0.0
L/D_i	114.469	102.04	124.776	122.54

Table 17: Low Fidelity Performance of Monarch, CCCA

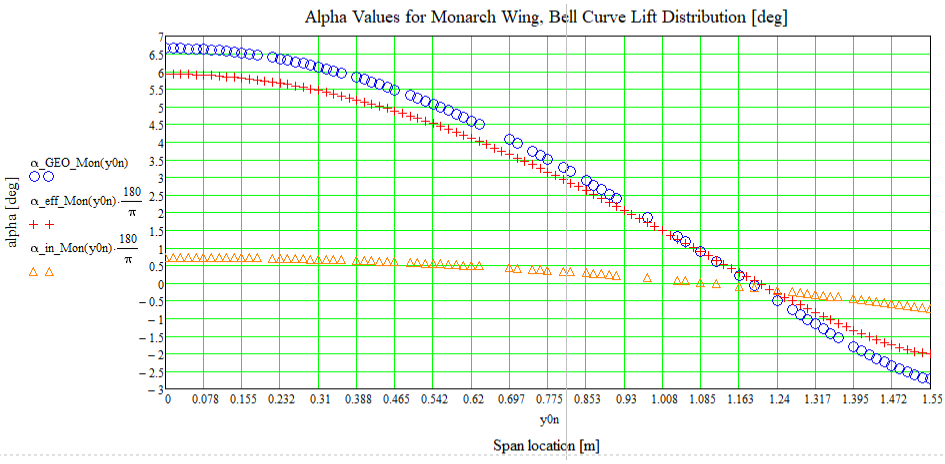

Figure 85: MathCad Geometric Twist, CCCA

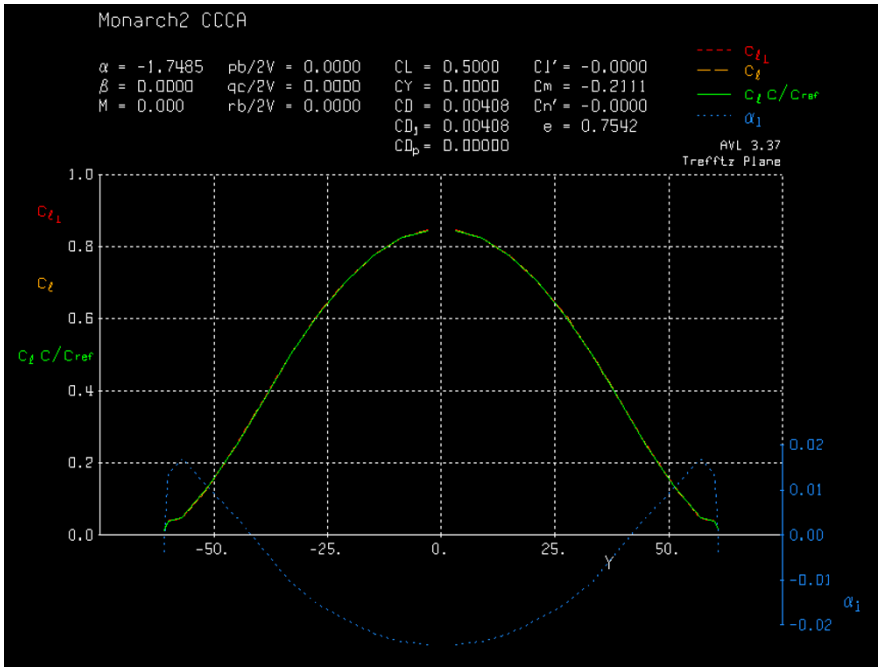

Figure 86: Vortex Lattice Results for CCCA

Attribute	MathCad	XFLR5 LLT	XFLR5 VLM2	AVL
α	0	-1.160	-0.76	-0.97
C_L	0.5	0.5	0.5	0.5
C_{D_i}	0.004368	0.0047	0.00444	0.004612
C_{D_P}	0.0	0.01553	0.0	0.0
$C_{D,TOTAL}$	—	0.02023	—	—
L/D$_i$	114.468	106.38	113.08	108.412

Table 18: Low Fidelity Performance of Monarch, CCVA

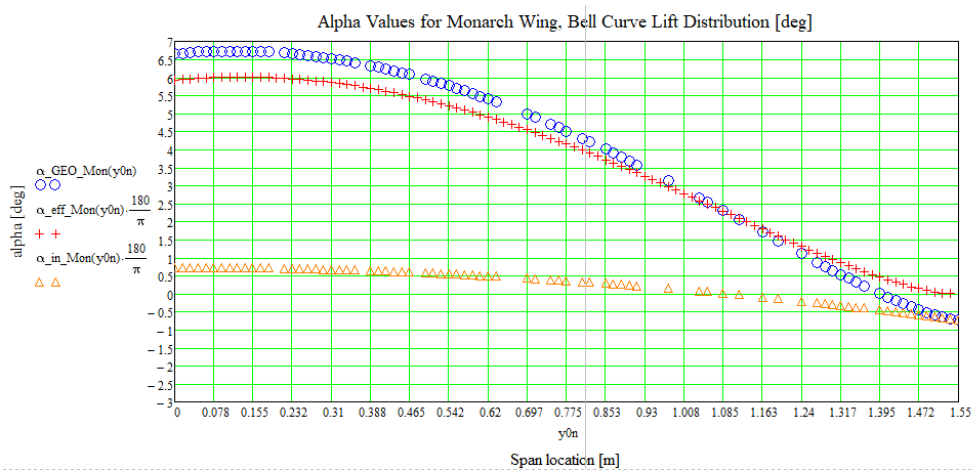

Figure 87: MathCad Geometric Twist, CCVA

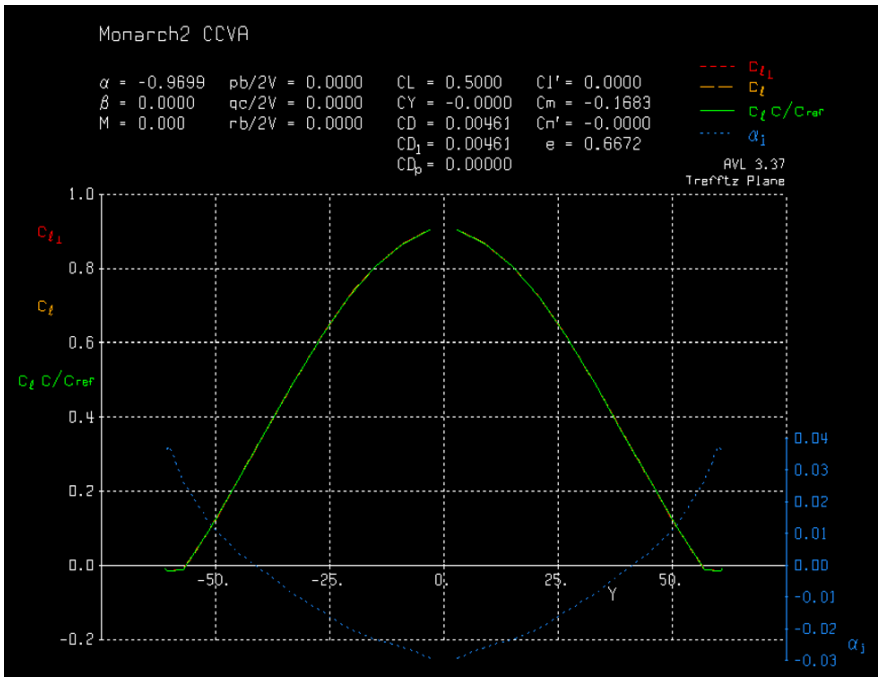

Figure 88: Vortex Lattice Results for CCVA

Attribute	MathCad	XFLR5 LLT	XFLR5 VLM2	AVL
α	0	-1.28	-1.23	-1.583
C_L	0.5	0.5	0.5	0.5
C_{D_i}	0.004368	0.00509	0.0040	0.004226
C_{D_P}	—	0.01657	—	—
$C_{D,TOTAL}$	—	0.02166	—	—
L/D$_i$	114.469	98.23	119.922	118.3263

Table 19: Low Fidelity Performance of Monarch, BCCA

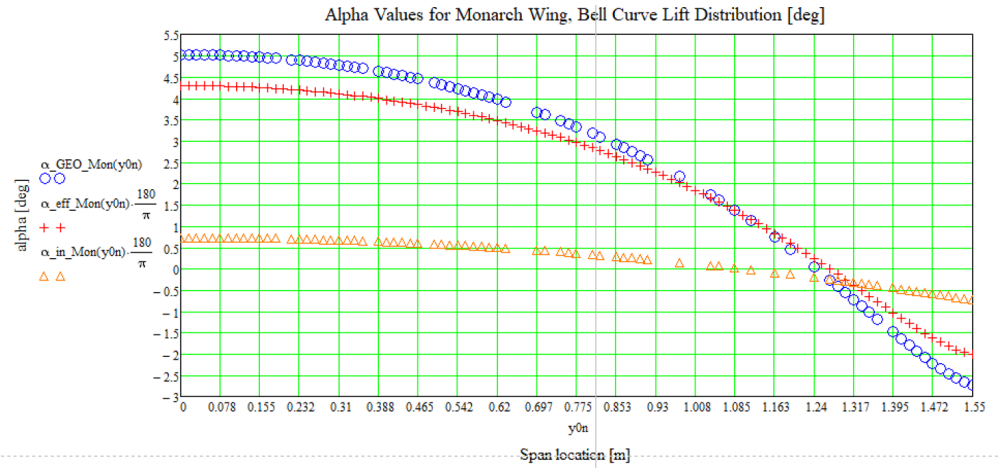

Figure 89: MathCad Geometric Twist, BCCA

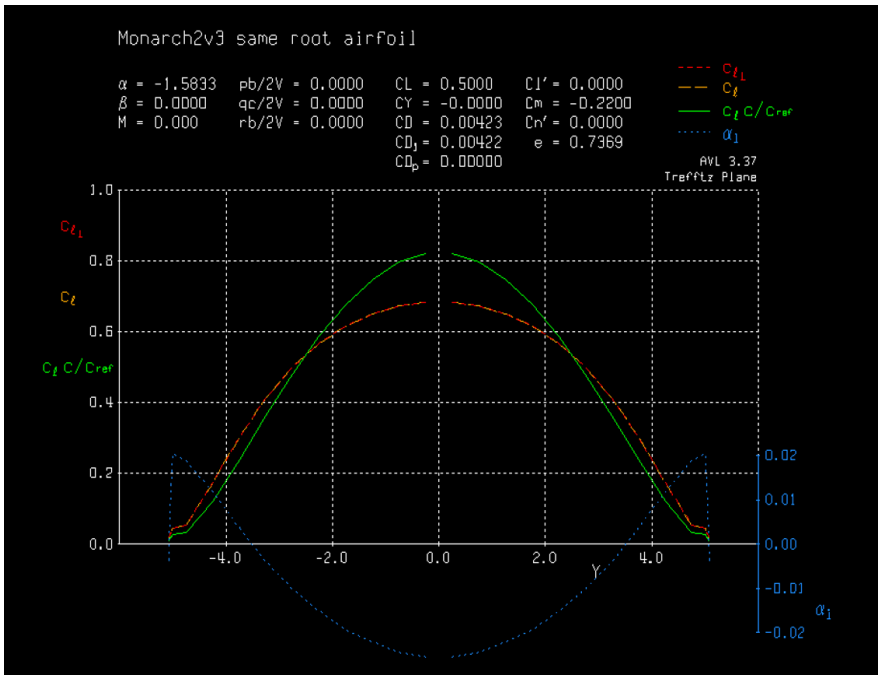

Figure 90: Vortex Lattice Results for BCCA

Attribute	MathCad	XFLR5 LLT	XFLR5 VLM2	AVL
α	0	-1.12	-0.68	-0.88
C_L	0.5	0.5	0.5	0.5
C_{D_i}	0.004368	0.00480	0.005	0.004787
C_{D_P}	—	0.0151	—	—
$C_{D,TOTAL}$	—	0.01991	—	—
L/D$_i$	114.468	104.166	108.343	104.449

Table 20: Low Fidelity Performance of Monarch, BCVA

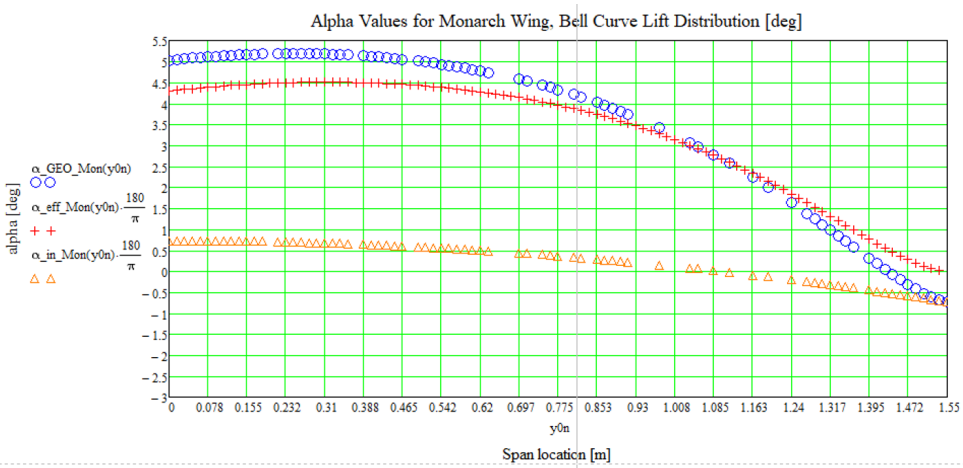

Figure 91: MathCad Geometric Twist, BCVA

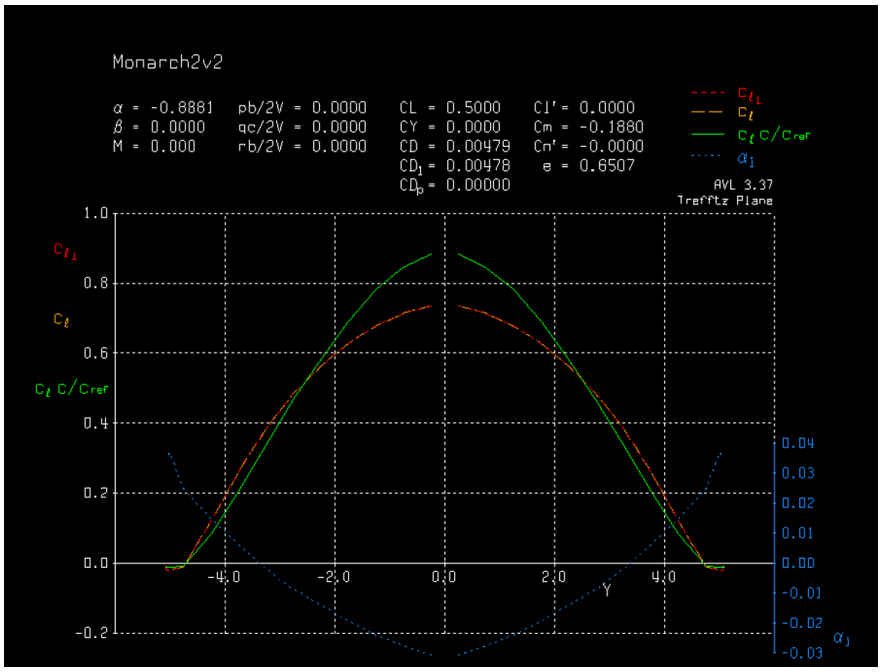

Figure 92: Vortex Lattice Results for BCVA

Attribute	MathCad	XFLR5 LLT	XFLR5 VLM2	AVL
α	0	-1.37	-1.36	-1.719
C_L	0.5	0.5	0.5	0.5
C_{D_i}	0.004368	0.00492	0.0040	0.0040447
C_{D_P}	—	0.01711	—	—
$C_{D,TOTAL}$	—	0.02204	—	—
L/D_i	114.469	101.626	125.258	123.618

Table 21: Low Fidelity Performance of Monarch, STCA

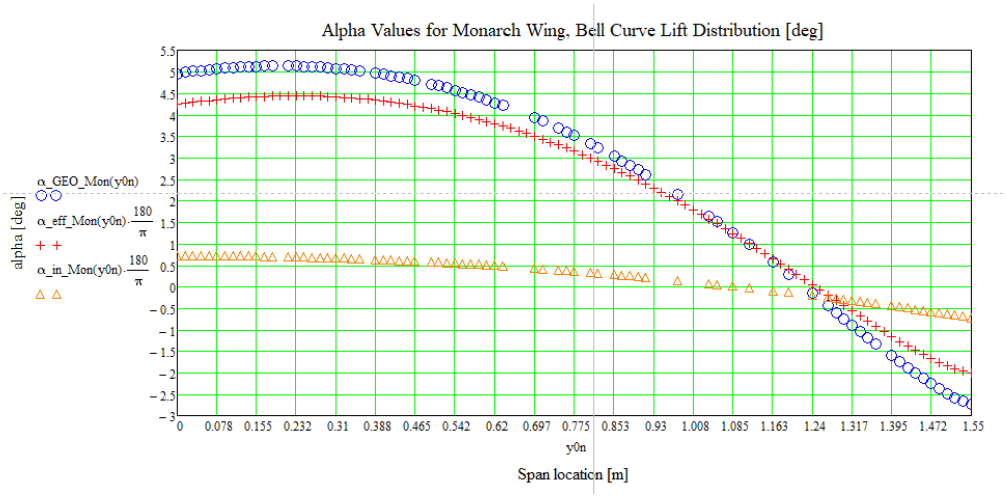

Figure 93: MathCad Geometric Twist, STCA

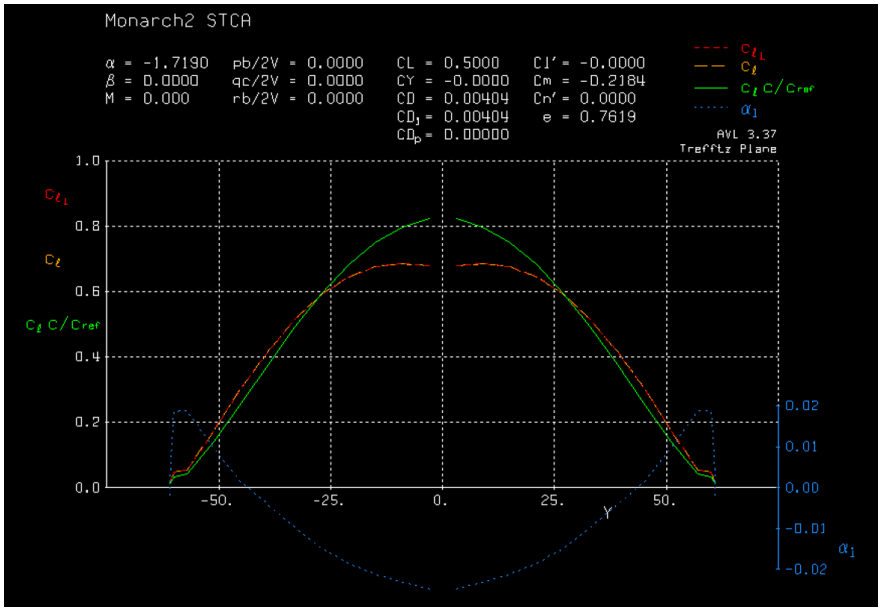

Figure 94: Vortex Lattice Results for STCA

Attribute	MathCad	XFLR5 LLT	XFLR5 VLM2	AVL
α	0	-1.16	-0.76	-0.968
C_L	0.5	0.5	0.5	0.5
C_{D_i}	0.004368	0.0047	0.004	0.0046102
C_{D_P}	—	0.01553	—	—
$C_{D,TOTAL}$	—	0.02023	—	—
L/D$_i$	114.468	106.383	112.606	108.455

Table 22: Low Fidelity Performance of Monarch, STVA

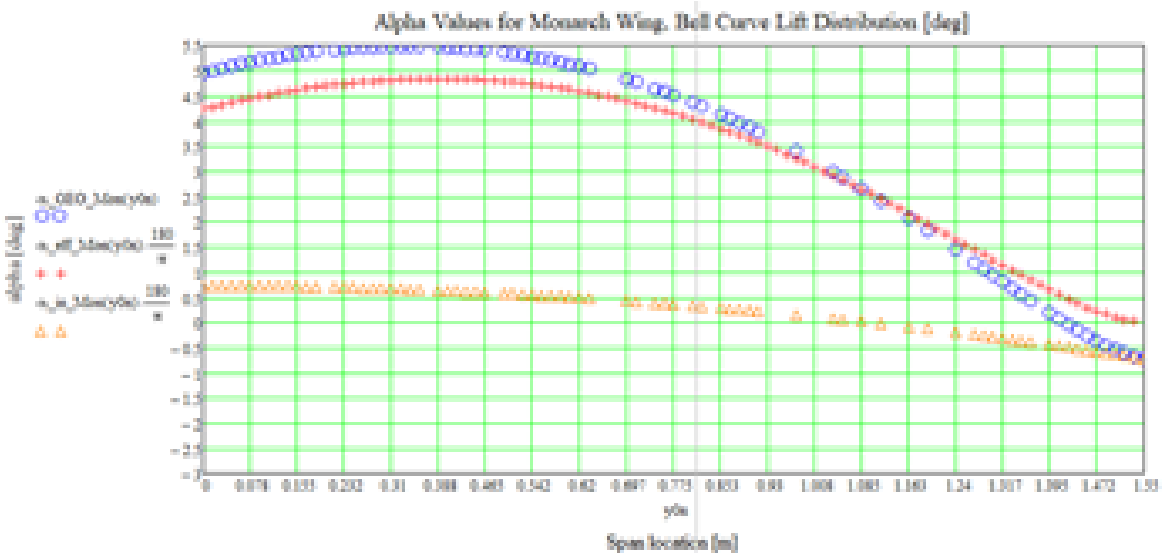

Figure 95: MathCad Geometric Twist, STVA

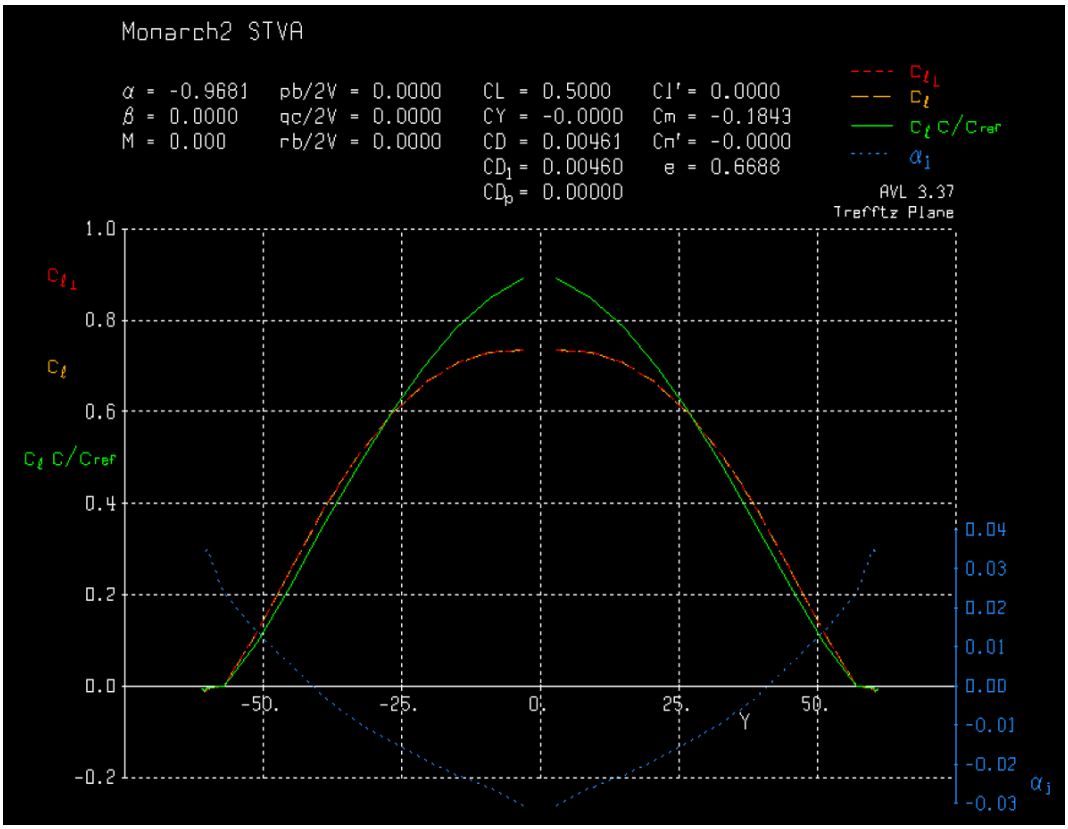

Figure 96: Vortex Lattice Results for STVA

MONARCH: Lift DIstribution Analysis

Volantex ASW-28 Specifications: mass := 1.35kg

$W := mass \cdot 9.81 \frac{m}{s^2} = 2.977 \cdot lbf$ Lift := W

b_stock := 2540mm = 8.333·ft y0 := −4.16ft, −4.15ft .. 4.15ft

y0_in := −4.16ft, −4.15ft .. 4.15ft

$bhalf := \frac{(b\_stock)}{2} = 4.167 \cdot ft$

Wing Geometries

Geometry Definitions: Stock

Tip Airfoil: CLARKY

c_tip := 3in

αL0_tip := −0.04363rad = −2.5·deg

Root Airfoil: CLARKY

c_root := 6.5in

αL0_root := −0.04363rad

$c\_stock(y0) := \sqrt{1 - \frac{(y0^2)}{(bhalf)^2}} \cdot 3.5in + 3in$

$taper := \frac{c\_tip}{c\_root} = 0.462$

$S\_stock := \int_{-bhalf}^{bhalf} c\_stock(y0)\, dy0 = 3.992 \cdot ft^2$

$dist\_\alpha L0\_stock(y0) := \alpha L0\_root + \left| \frac{\alpha L0\_root - \alpha L0\_tip}{bhalf} \cdot y0 \right|$

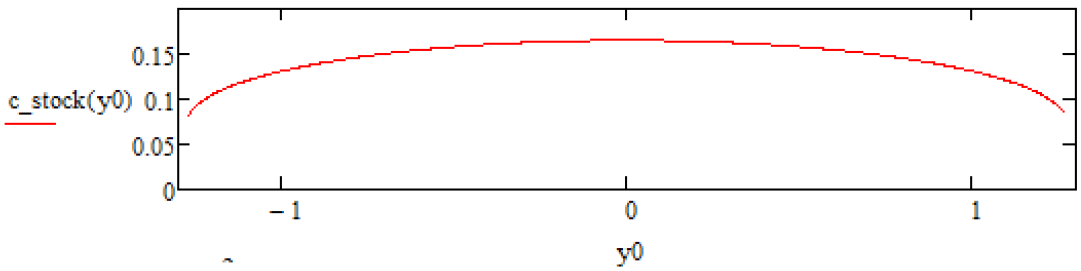

$MAC\_stock := \frac{S\_stock}{b\_stock} = 5.749 \cdot in$

$AR\_stock := \frac{b\_stock^2}{S\_stock} = 17.395$

Geometry Definitions: Monarch1

Tio Airfoil: Monarch1

$c\_tip := 3.44in$

$\alpha L0\_tip := -2deg$

Root Airfoil: sd7032/WASP combo, MONARCH

$c\_root := 6in$

$\alpha L0\_root := -2deg = -0.035$

$taper := \frac{c\_tip}{c\_root} = 0.573$

$b\_Mon := 1.22 \cdot b\_stock = 10.167 \cdot ft$

$bhalf\_new := \frac{b\_Mon}{2}$

$\frac{b\_Mon - b\_stock}{b\_stock} = 0.22$

According to Ludwig (1933), a 22% increase in span with constant root bending moment creates less induced drag

$y0n := -(bhalf\_new), -(bhalf\_new \cdot 0.99) .. bhalf\_new$

$y0n\_in := -(bhalf\_new), -(bhalf\_new \cdot 0.99) .. bhalf\_new$

$$c\_Mon1(y0n) := (c\_root - c\_tip)\left[1 - \left(\frac{y0n}{bhalf\_new}\right)^2\right]^{\frac{3}{2}} + c\_tip$$

$$c\_Mon(y0n) := -\left|\frac{c\_root - c\_tip}{bhalf\_new} \cdot y0n\right| + c\_root$$

Root Airfoil Options:
- s3002-il
- s7012-il
- s9000-il
- sd5060-il
- sd7032-il ***

$$dist\_\alpha L0\_Mon(y0n) := \alpha L0\_root + \left|\frac{\alpha L0\_root - \alpha L0\_tip}{bhalf\_new} \cdot y0n\right|$$

$c\_Mon(0) = 6 \cdot in$

$c\_Mon(5ft) = 3.482 \cdot in$

$$S\_Mon := \int_{-bhalf\_new}^{bhalf\_new} c\_Mon(y0n)\, dy0n = 3.999 \cdot ft^2$$

$S\_stock = 3.992 \cdot ft^2$

$$AR\_Mon := \frac{(2 \cdot bhalf\_new)^2}{S\_Mon} = 25.847$$

$$MAC\_Mon := \frac{S\_Mon}{b\_Mon} = 0.393 \cdot ft$$

$$c\_Mon\_BCCA(y0n) := (6in - 3in)\left[1 - \left(\frac{y0n}{bhalf\_new}\right)^2\right]^{\frac{3}{2}} + 3in$$

$$c\_Mon\_STCA(y0n) := -\left|\frac{6in - 3.44in}{bhalf\_new} \cdot y0n\right| + 6in$$

$$c\_Mon\_MACCA(y0n) := 4.764in$$

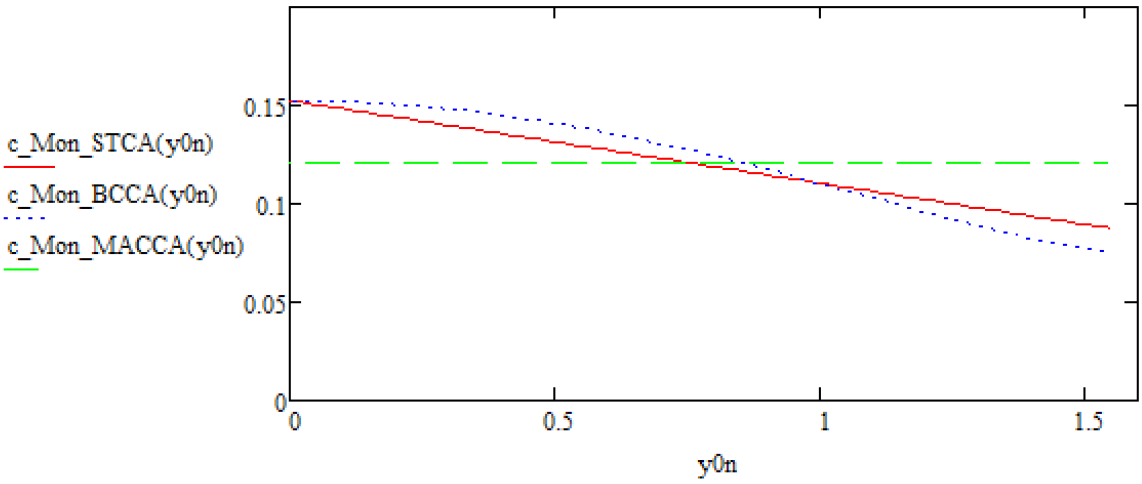

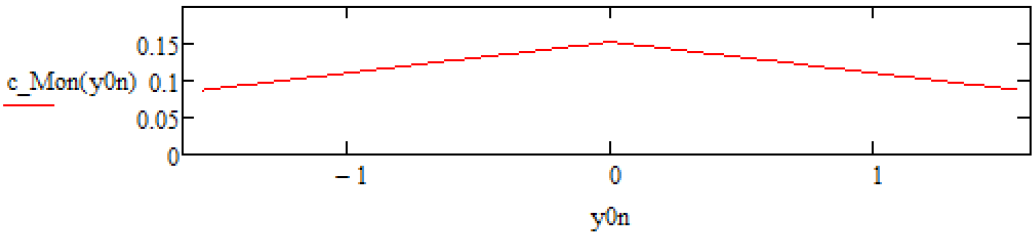

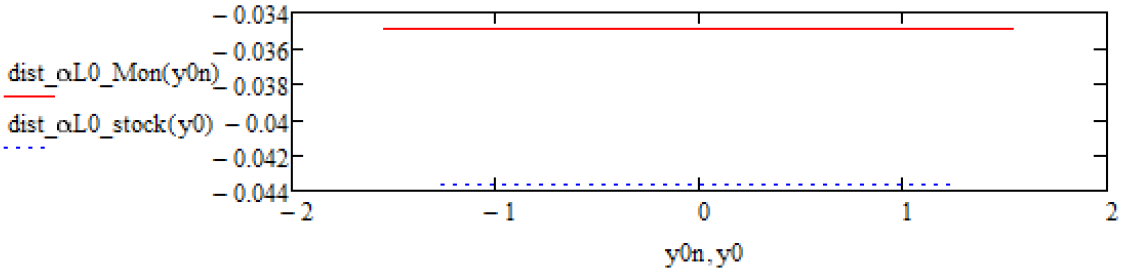

Flight Conditions Definitions:

Flight Conditions: Stock Aircraft w/ Elliptical Lift Distribution, L'

Using a benchmarked design CL to achieve, back out cruise velocity

$CL\_stock := 0.5$ $\rho\_stilly := 0.002308 \frac{slug}{ft^3} = 1.189 \frac{kg}{m^3}$

$V\_stock := \sqrt{\frac{2Lift}{\rho\_stilly \cdot CL\_stock \cdot S\_stock}} = 35.951 \cdot \frac{ft}{s}$

$S\_stock = 3.992 \cdot ft^2$

$dist\_L\_stock(y0) := \frac{0.455lbf}{ft} \sqrt{1 - \frac{(y0^2)}{(bhalf)^2}}$, also known as L'

$Lift\_stock := \int_{-bhalf}^{bhalf} dist\_L\_stock(y0)\, dy0 = 2.978 \cdot lbf$

$\mu\_stilly := 3.717 \times 10^{-7} \frac{slug}{ft \cdot s}$

$dist\_M\_stock(y0) := dist\_L\_stock(y0) \cdot y0$

$W = 2.977 \cdot lbf$

$rootM\_stock := \int_{0}^{bhalf} dist\_M\_stock(y0)\, dy0 = 2.633 \cdot lbf \cdot ft$

We will design the new wing to have this same root bending moment as the stock wing

$Re\_stock := \frac{\rho\_stilly \cdot V\_stock \cdot c\_stock(0)}{\mu\_stilly} = 1.209 \times 10^5$

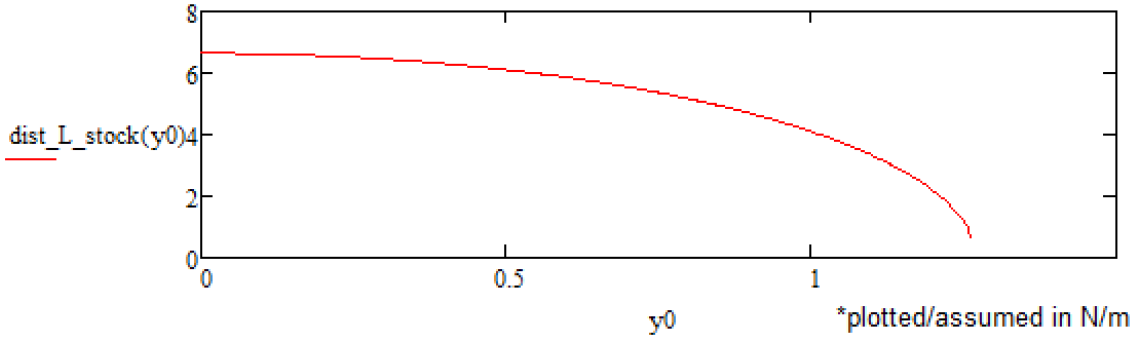

*plotted/assumed in N/m

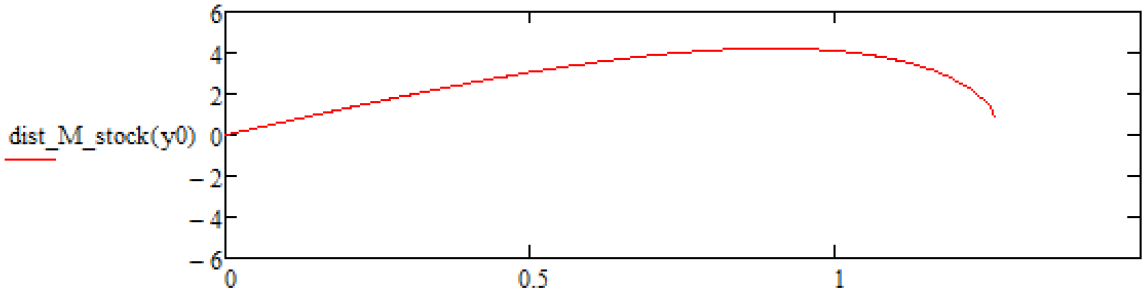

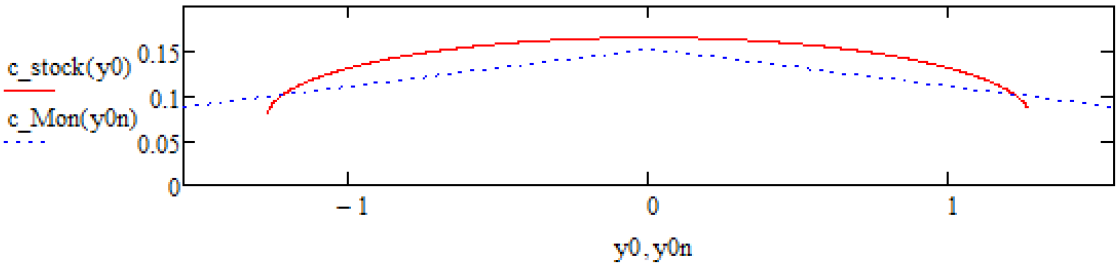

$$dist\_CL\_stock(y0) := \frac{dist\_L\_stock(y0)}{0.5 \cdot \left(\rho\_stilly \cdot V\_stock^{2}\right) \cdot c\_stock(y0)}$$

$$cCL\_stock(y0) := \frac{dist\_CL\_stock(y0) \cdot c\_stock(y0)}{MAC\_stock}$$

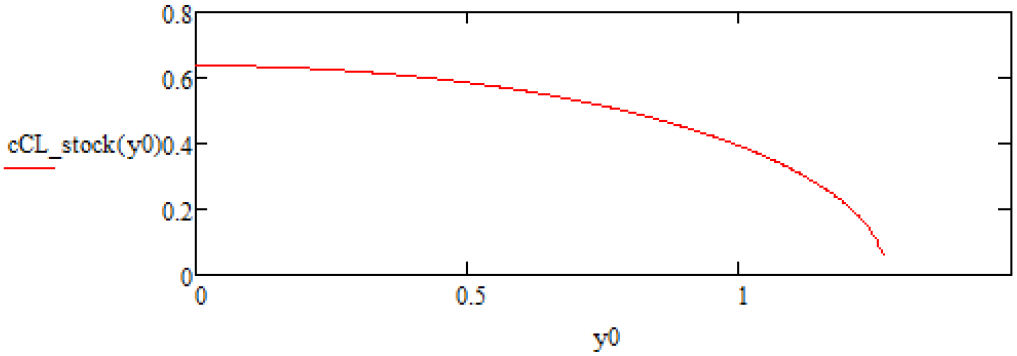

Flight Conditions: MONARCH

Using a benchmarked design CL to achieve, back out cruise velocity fro new wing

$CL\_Mon := CL\_stock = 0.5$ Same designed CL value as the volantex aircraft

$$V\_Mon := \sqrt{\frac{2Lift}{\rho\_stilly \cdot CL\_Mon \cdot S\_Mon}} = 10.949 \cdot \frac{m}{s}$$

$$V\_Mon = 10.949 \frac{m}{s}$$

two variables can change when looking to keep root bending moment constant: Ldist_y0 (lift distribution value at root) and span

$$dist\_L\_Mon(y0n) := 0.509 \frac{lbf}{ft} \cdot \left[1 - \left(\frac{y0n}{bhalf\_new}\right)^{2}\right]^{\frac{3}{2}}$$

$$dist\_CL\_Mon(y0n) := \frac{dist\_L\_Mon(y0n)}{0.5 \cdot \left(\rho\_stilly \cdot V\_Mon^2\right) \cdot c\_Mon(y0n)}$$

$$Lift\_Mon := \int_{-bhalf\_new}^{bhalf\_new} dist\_L\_Mon(y0n)\, dy0n = 3.048 \cdot lbf$$

$Lift\_stock = 2.978 \cdot lbf$ comparitively to stock wing, generated lift is **constant**

$$dist\_M\_Mon(y0n) := dist\_L\_Mon(y0n) \cdot y0n$$

$$rootM\_Mon := \int_{0}^{bhalf\_new} dist\_M\_Mon(y0n)\, dy0n = 2.631 \cdot ft \cdot lbf$$

Root bending moment created by one wing

$rootM\_stock = 2.633 \cdot ft \cdot lbf$ comparitively to stock wing

$$Re\_Mon := \frac{\rho\_stilly \cdot V\_Mon \cdot MAC\_Mon}{3.735 \cdot 10^{-7}\ \frac{slug}{ft \cdot s}} = 8.731 \times 10^4$$

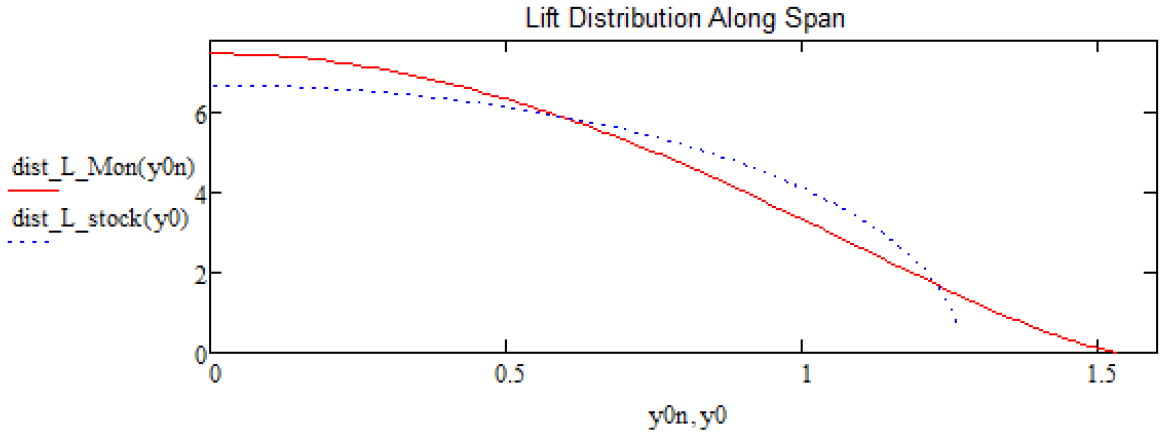

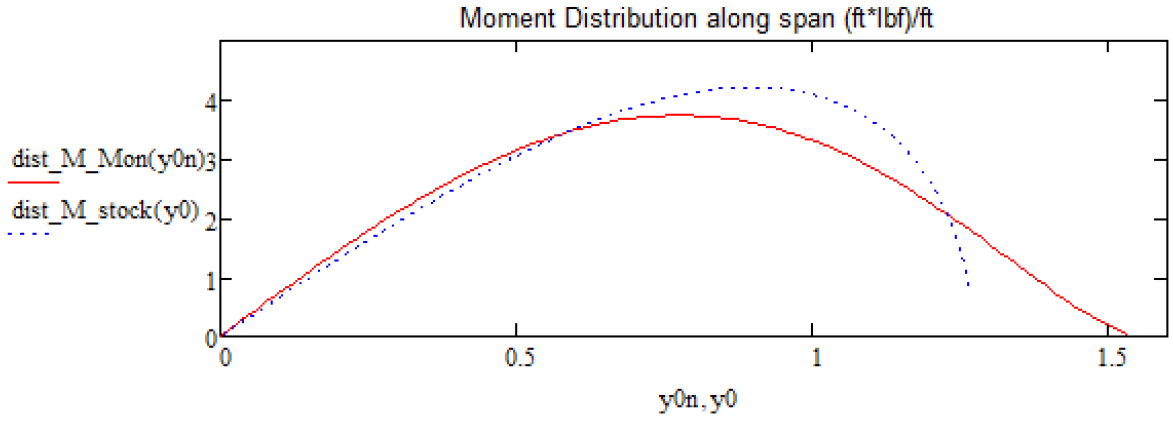

$$cCL\_Mon(y0n) := \frac{dist\_CL\_Mon(y0n) \cdot c\_Mon(y0n)}{MAC\_Mon}$$

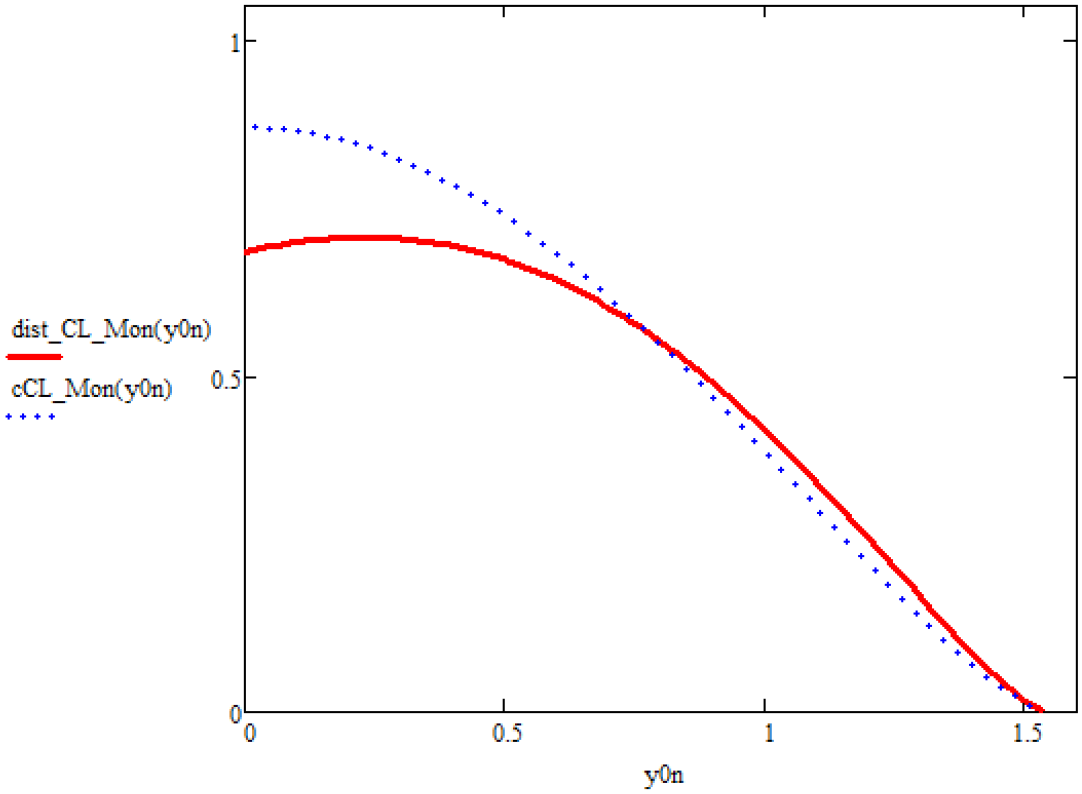

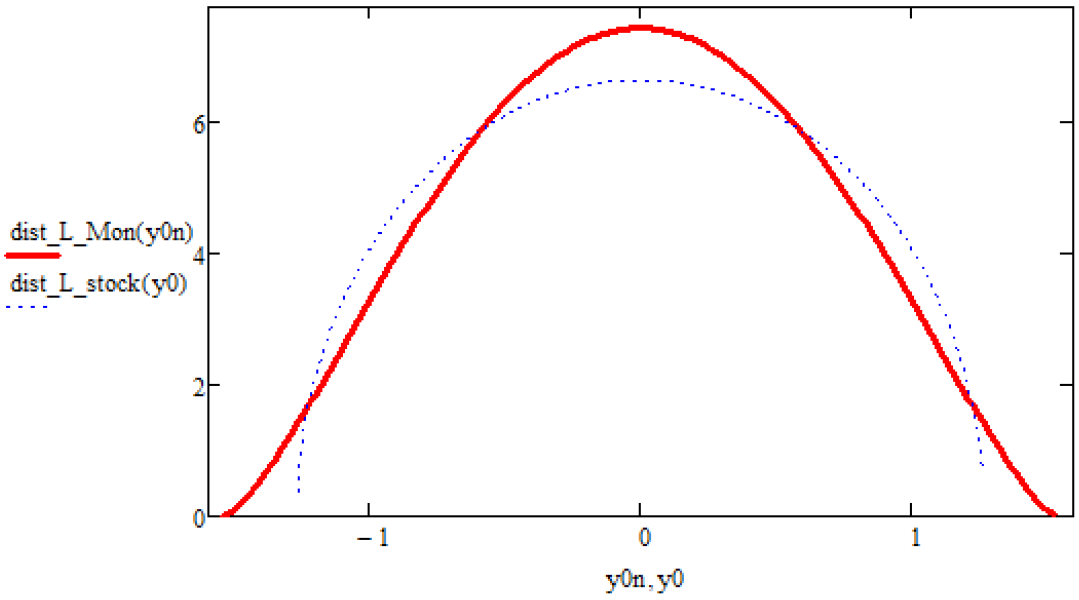

Lift, Circulation, and α Calculations:

Lift and Circulation Calculations: Stock

$$dist\_cL\_stock(y0) := \frac{dist\_L\_stock(y0)}{\frac{1}{2}\cdot \rho\_stilly \cdot V\_stock^{2} \cdot c\_stock(y0)}$$

$dist\_cL\_stock(0) = 0.563$

local cL value of stock wing created at wing root

$$dist\_\Gamma\_stock(y0) := \frac{dist\_L\_stock(y0)}{\rho\_stilly \cdot V\_stock}$$

$$dist\_d\Gamma\_stock(y0) := \frac{d}{dy0}(dist\_\Gamma\_stock(y0))$$

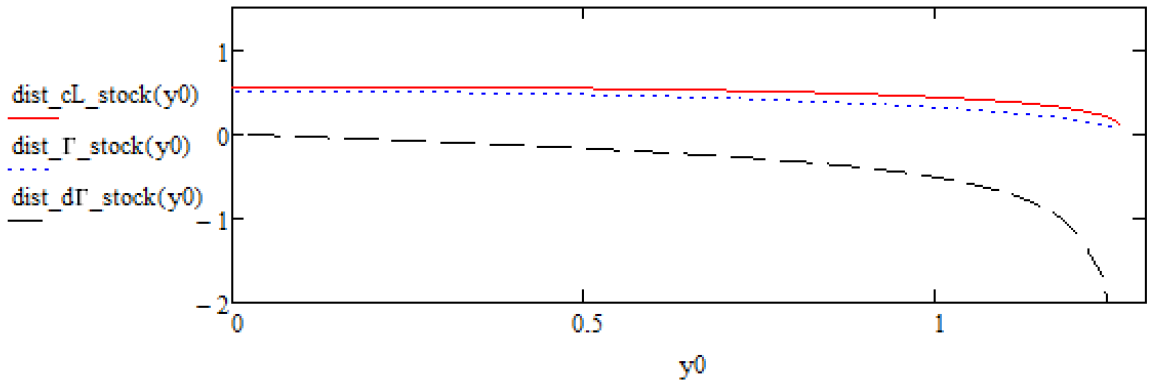

$$\alpha\_eff\_stock(y0) := \left(\frac{dist\_\Gamma\_stock(y0)}{\pi \cdot V\_stock \cdot c\_stock(y0)} + dist\_\alpha L0\_stock(y0)\right)$$

$$\alpha\_in\_stock(y0) := \left(\frac{1}{4\cdot\pi\cdot V\_stock}\cdot\int_{-bhalf}^{bhalf}\frac{dist\_d\Gamma\_stock(y0\_in)}{y0 - y0\_in}\,dy0\_in\right)$$

$$\alpha\_GEO\_stock(y0) := (\alpha\_eff\_stock(y0) + \alpha\_in\_stock(y0))\cdot\frac{180}{\pi}$$

sum of two alpha values, converted to degrees

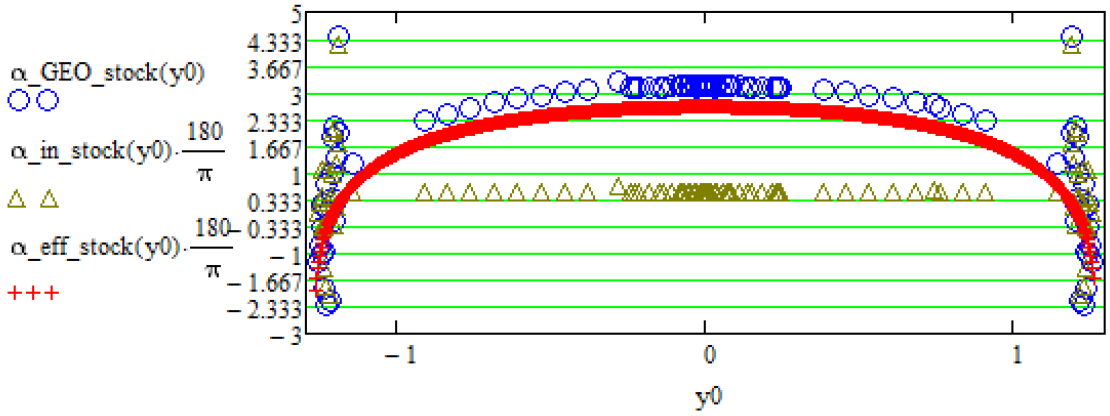

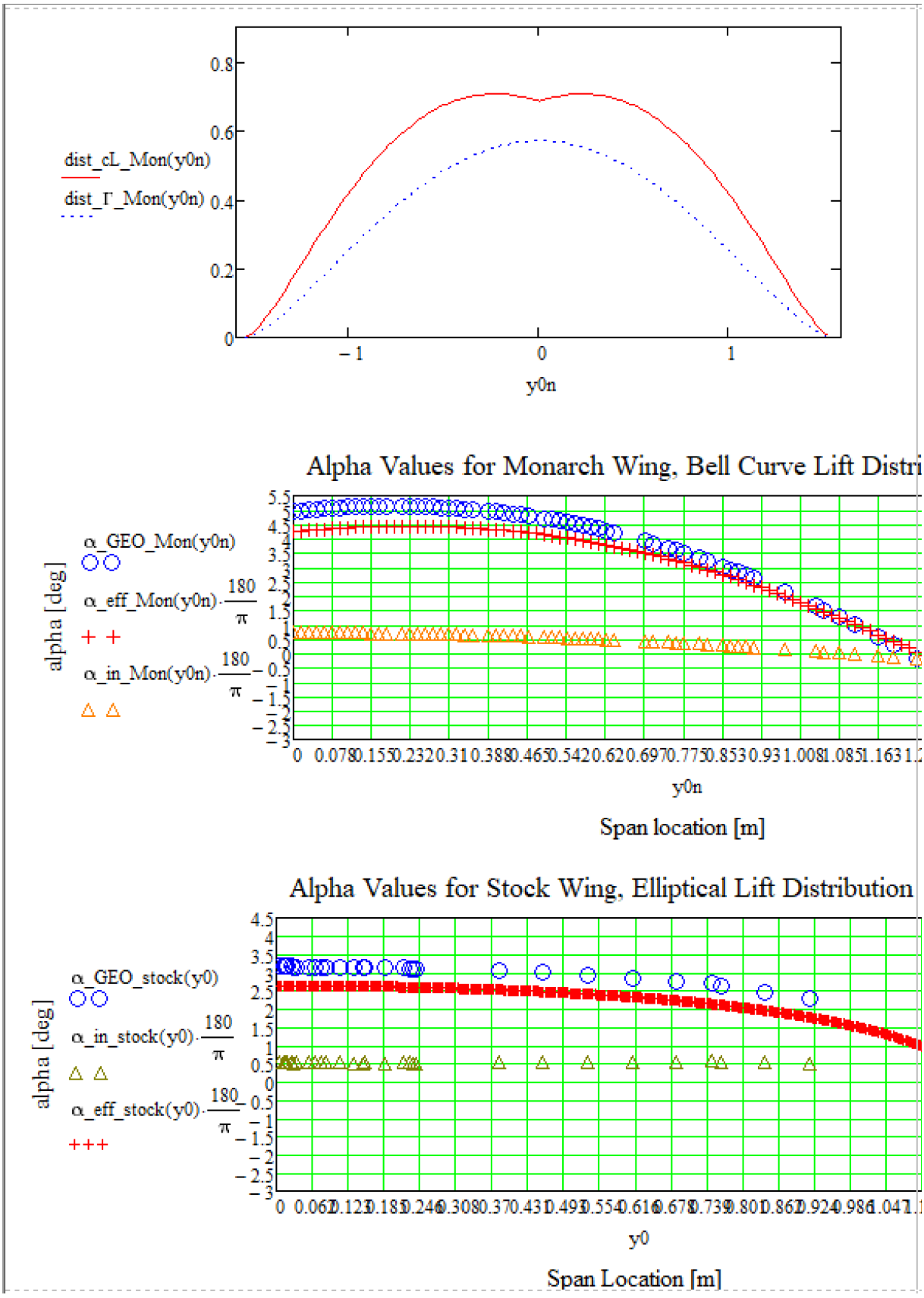
dist_cL_Mon(y0n)
dist_Γ_Mon(y0n)
y0n
Alpha Values for Monarch Wing, Bell Curve Lift Distri
α_GEO_Mon(y0n)
α_eff_Mon(y0n)·180/π
α_in_Mon(y0n)·180/π
alpha [deg]
y0n
Span location [m]
Alpha Values for Stock Wing, Elliptical Lift Distribution
α_GEO_stock(y0)
α_in_stock(y0)·180/π
α_eff_stock(y0)·180/π
alpha [deg]
y0
Span Location [m]

Induced Alpha Curve Fitting & Induced Drag Calculations

$$\text{fitted\_}\alpha\text{i\_stock}(y0) := \frac{\text{dist\_}\Gamma\text{\_stock}(0)}{2 \cdot \text{b\_stock} \cdot \text{V\_stock}}$$

$$\text{fitted\_}\alpha\text{i\_Mon}(y0n) := \frac{-0.0009752}{\text{ft}^2} \cdot y0n^2 + 0.01275$$

$$\text{CDi\_Mon} := \frac{2}{\text{V\_Mon} \cdot \text{S\_Mon}} \cdot \int_{-0.99\text{bhalf\_new}}^{0.99\text{bhalf\_new}} \text{dist\_}\Gamma\text{\_Mon}(y0n) \cdot \text{fitted\_}\alpha\text{i\_Mon}(y0n)\, dy0n = 4.377 \times 10^{-3}$$

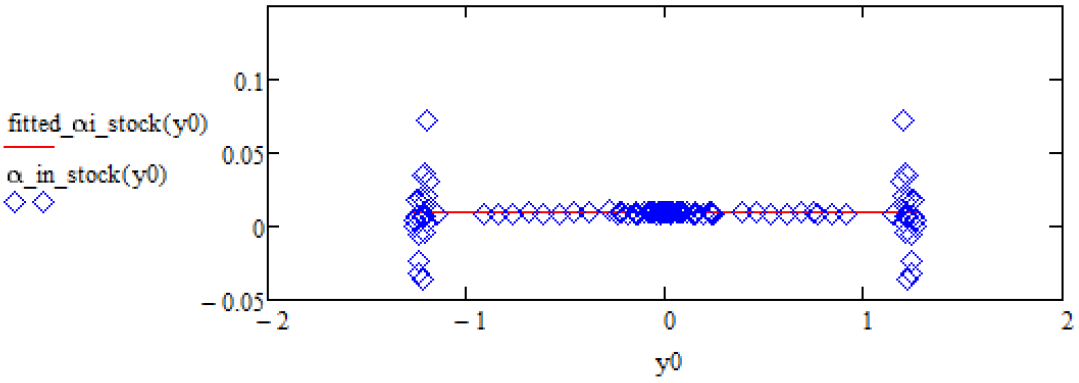

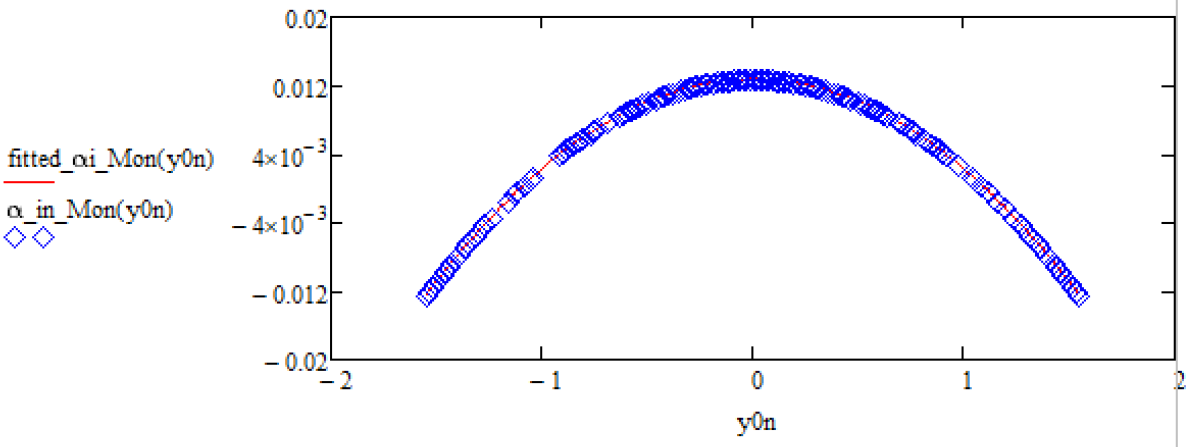

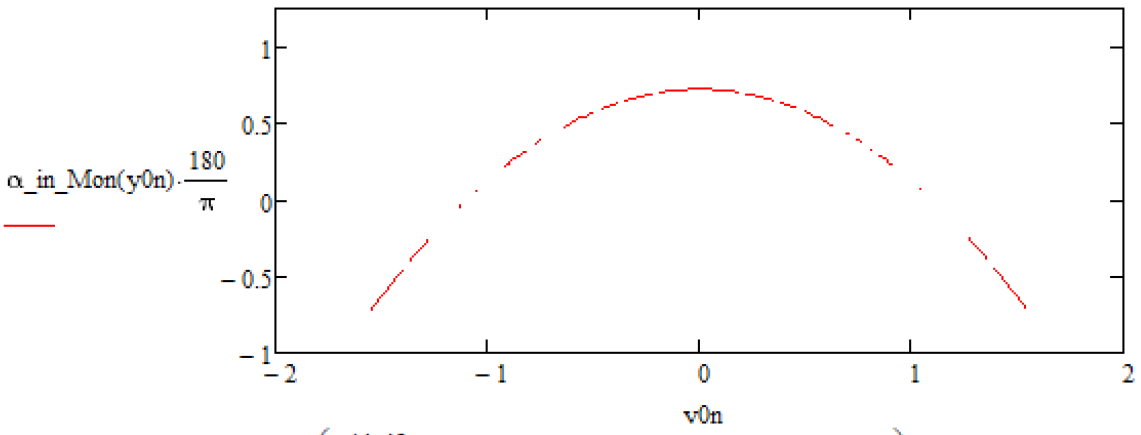

$$D\_in\_stock := \left(\int_{-bhalf}^{bhalf} dist\_L\_stock(y0) \cdot fitted\_\alpha i\_stock(y0)\, dy0 \right) = 0.027 \cdot lbf$$

$$D\_in\_Mon := \left(\int_{-bhalf\_new}^{bhalf\_new} dist\_L\_Mon(y0n) \cdot fitted\_\alpha i\_Mon(y0n)\, dy0n \right) = 0.026 \cdot lbf$$

$$CD\_in\_stock := \frac{D\_in\_stock}{\left(\frac{1}{2} \cdot \rho\_stilly \cdot V\_stock^{2} \cdot S\_stock \right)} = 4.577 \times 10^{-3}$$

$$CD\_in\_Mon := \frac{D\_in\_Mon}{\left(\frac{1}{2} \cdot \rho\_stilly \cdot V\_Mon^{2} \cdot S\_Mon \right)} = 4.377 \times 10^{-3}$$

$$e\_Mon := \frac{CL\_Mon^{2}}{\pi \, CD\_in\_Mon \cdot AR\_Mon} = 0.703$$

Results:

dont forget to re-fit the induced alpha graphs

$V\_Mon = 35.921 \cdot \frac{ft}{s}$

$S\_Mon = 3.999 \cdot ft^2$

$b\_Mon = 10.167 \cdot ft$ These include fuselage!

$CL\_Mon = 0.5$

$Lift\_Mon = 3.048 \cdot lbf$

$dist\_L\_Mon(0) = 0.509 \cdot \frac{lbf}{ft}$

$rootM\_Mon = 2.631 \cdot lbf \cdot ft$

$D\_in\_Mon = 0.026 \cdot lbf$

$CD\_in\_Mon = 4.377 \times 10^{-3}$

$V\_stock = 35.951 \cdot \frac{ft}{s}$

$S\_stock = 3.992 \cdot ft^2$

$b\_stock = 8.333 \cdot ft$

$CL\_stock = 0.5$

$Lift\_stock = 2.978 \cdot lbf$

$dist\_L\_stock(0) = 0.455 \cdot \frac{lbf}{ft}$

$rootM\_stock = 2.633 \cdot lbf \cdot ft$

$Di\_stock = 0.028 \cdot lbf$

$CDi\_stock = 4.621 \times 10^{-3}$

$$\frac{D\_in\_Mon - D\_in\_stock}{\frac{(D\_in\_stock + D\_in\_Mon)}{2}} = -4.469 \cdot \%$$

This is the reduction in induced drag for the new wing

$$\frac{CD\_in\_Mon - CD\_in\_stock}{\frac{(CD\_in\_stock + CD\_in\_Mon)}{2}} = -4.469 \cdot \%$$

This is the reduction in induced drag coefficient for the new wing

$$\frac{S\_Mon - S\_stock}{S\_stock} = 0.165 \cdot \%$$

This is the % increase in planform area --> stays relatively the same

$$\frac{b\_Mon - b\_stock}{b\_stock} = 22 \cdot \%$$

This is the % increase in span length (22% is theory based)

$AR\_Mon = 25.847$

$$e\_Mon := \frac{CL\_Mon^2}{\pi \, AR\_Mon \cdot CD\_in\_Mon} = 0.703$$

VITA

Cole Kelly

Candidate for the Degree of

Master of Science

Thesis: PROJECT MONARCH: THE APPLICATION OF LUDWIG PRANDTL'S BELL-CURVE SPAN LOADING TO A STRAIGHT, HIGH PERFORMANCE SAILPLANE WING

Major Field: Mechanical and Aerospace Engineering

Biographical:

Education:

Completed the requirements for the Master of Science in Mechanical and Aerospace Engineering at Oklahoma State University, Stillwater, Oklahoma in July, 2021.

Completed the requirements for the Bachelor of Science in Aerospace Engineering at Oklahoma State University, Stillwater, Oklahoma in 2019.

Completed the requirements for the Bachelor of Science in Mechanical Engineering at Oklahoma State University, Stillwater, Oklahoma in 2019.

Professional Memberships:

American Institute for Aeronautics and Astronautics

American Physics Society